DISS. ETH No 18340

ANALYSIS AND DESIGN OF COMPACT PASSIVE DISTRIBUTION NETWORKS FOR MICROWAVE APPLICATIONS

A dissertation submitted to the
SWISS FEDERAL INSTITUTE OF TECHNOLOGY ZURICH

for the degree of
Doctor of Sciences

presented by
George Tudosie
Dipl. Ing. Technische Universität Darmstadt, Germany
born September 9, 1978
citizen of Romania

accepted on the recommendation of
Prof. Dr. C. Hafner, examiner
Prof. Dr. R. Vahldieck, co-examiner
Prof Dr. W. Bächtold, co-examiner
Prof Dr. A. Jacob, co-examiner

2009

Pentru parintii mei

Acknowledgments

This research was carried out at the Laboratory for the Electromagnetic Fields and Microwave Electronics (IFH), ETH Zurich, Zurich, Switzerland. I would like to express my gratitude to several people who made this work possible. I would like to thank Prof. Dr. Rüdiger Vahldieck for his support throughout all the research time. Special thanks go to Prof. Dr. Christian Hafner for accepting to be examiner of this thesis and supporting me in this time.

I would like to thank very much Prof. Dr. Arne Jacob from the Faculty of Electrical Engineering of the University of Hamburg-Harburg, and Prof. Dr. Werner Bächtold from ETH Zurich for accepting to be my co-examiner and for reading and commenting on this thesis.
Many thanks go to all, which were my colleagues at IFH, for making my stay and work at the institute unforgettable. Special thanks go to the support of my students Andreas Büchel, Mariko Bürgin, Valeria Hunkeler, Cornelia Setz, Thomas Schiesser, Conradin Merk, Stephanie Jarno.

I am in debt to Martin Lanz and Hansrüdi Benedikter for having in them the best technicians one can have. Only this made it possible to go for the most challenging fabrications and measurements of microwave devices. The same gratitude I would like to express to Ray Ballisti, Aldo Rossi and Federico Bonzanigo for their help and support with any computer matters. Last but not least, I would like to thank the warm soul of the institute Barbara Schuhbeck-Wagner. Without the help of all, my work would not be possible.
Finally, the financial assistance from the Swiss National Science Foundation (SNF), the Confederation's innovation promotion (CTI) and Armasuisse is greatly appreciated.

Outside the ETH, I would like to thank the people, who supported me in the best way one can expect, with patience and love.

Abstract

Various modern radars, radiometers and communication systems move towards the implementation of highly directive and active space filtering radio frequency (RF) front ends. Networks with the capability to form multiple radiation beams are therefore becoming essential.
Addressing the different space sectors at the same time leads to a higher system capacity by re-using the time, code and frequency. Over the years two passive beamforming networks prevailed: the Rotman lens and the Butler matrix. Unfortunately, at lower microwave frequencies as well as for complex systems, the two beam forming networks become quite large and difficult to integrate in compact transceivers.
To overcome this major problem and make the Rotman lens amenable to higher integration, this work introduces on one side a novel lens design using multi-dielectric substrates and folding procedures of the Rotman lenses. Analytical formulations for the design of the multi-dielectric Rotman lenses have been derived. The effort is motivated by the expected size reduction and increased efficiency of the lens. Introducing dielectric slabs of different permittivity within the lens creates an refraction, and therefore, additional focus inside the lens. Parametric and error analyses of the conventional and the new lens structures were carried out and the comparison showed the benefits of the new design in terms of size reduction while maintaining the overall performance properties. The non-uniform substrate is a key change from the conventional Rotman lenses design.
The complexity and size scaling of the Butler matrix on the other side is addressed using the low temperature cofired ceramics (LTCC) technology. A novel Butler matrix design based on folding and stacking of the matrix elements is developed. The geometrical rebuild of the Butler matrix leads to a significant size reduction, modularization thus providing a true 3D integration of the matrix. This again reduces the overall lateral dimension drastically and due to its modular structure offers for the first time extendibility to higher order Butler matrices
The thesis contains a set of multi-dielectric lenses as well as LTCC Butler matrixes. This beamforming networks were realized and measured to validate the stratagem behind the integrative solution.

Zusammenfassung

Moderne Radar-, Radiometern- und Kommunikationssysteme erfordern hochdirektive und raumselektive Antennengruppen. Eine gleichzeitige Auswertung unterschiedlicher Raumrichtungen ermöglicht die Wiederverwendung derselben Zeitfenstern, Kodierungen und Frequenzkanälen. Schlüsselkomponenten dieser Systeme sind Netzwerke, welche gleichzeitig mehrfache Abstrahlcharakteristiken mithilfe einer einzigen Antennengruppe bilden können.
Im Verlauf der Zeit waren es überwiegend zwei passive Netzwerke, die den Weg in praktische Anwendungen gefunden haben: die Rotman-Linse und die Butler Matrix. In kompakten Sendeempfängern und im Bereich niederfrequenter Applikationen sind diese zwei wichtigen Netzwerke wegen ihrer Komplexität und Größe unmöglich oder sehr schwierig einzubauen.
Ziel dieser Arbeit war es, diese bedeutende Hürde zu überwinden und sowohl die Rotman-Linsen als auch die Butler Matrix für eine kompaktere Integration zu erweitern.
Erstens wurden für die Rotman-Linsen neue Linsenausführungen verwendet, die mittels mehrfacher dielektrischer Substrate und einer geometrischen Faltung eine Größenreduktion erzielen. Gleichzeitig wurde dafür eine neue analytische Ableitung entwickelt. Dadurch konnte erstmals eine Verkleinerung, aber auch eine Effizienzverbesserung der Linse erreicht werden. Die Verwendung von dielektrischen Streifen unterschiedlicher Permittivität innerhalb der Linse ergibt eine zusätzliche Brechung und, daraus folgend, einen Fokus innerhalb der Linse. Die Parameter- und Fehleruntersuchungen der bisher bekannten und der neuen Linsenstrukturen konnten die geometrische Reduktion bei gleichzeitigem Beibehalten der generellen Leistungseigenschaften festigen.
Zweitens konnten die Komplexität und die Größenreduktion der Butler Matrix mithilfe von Niedertemperatur-Einbrand-Keramiken (LTCC) erreicht werden. Ein neues Verfahren, basierend auf die Faltung und das Aufstapeln der Elemente einer Matrix, wurde entwickelt. Die geometrische Rekonstruktion der Matrix anhand eines modularen Aufbaus zeigte eine deutliche Verkleinerung der Flächengröße, wobei die elektrische Leistung exzellent blieb. Diese 3D-Integration der Butler Matrix reduziert wiederum die seitliche Ausdehnung deutlich und ermöglicht – erstmalig – die Verwirklichung von Matrizen höherer Ordnung.

In dieser Arbeit werden sowohl eine Reihe von Rotman-Linsen mit Mehrfachsubstraten beschrieben und analysiert, als auch eine Serie von LTCC Butler Matrizen. Anhand deren Aufbaus und der anschließenden Messungen konnte die integrative Strategie untermauert werden.

Contents

List of Figures

Chapter 1

Introduction

1.1 Motivation

Various modern radars, radiometers, and communication systems move towards the implementation of highly directive and active space filtering radio frequency (RF) front ends. Networks with the capability to form multiple radiation beams are becoming more and more attractive for commercial applications such as the area of space division multiplex access (SDMA), automotive radars, and in remote sensing systems. The history of the beamforming networks, best described in [1], reaches back to the phased arrays in radars implemented in a variety of practical realizations [2].

Beamforming networks are essential components for any multi beam systems. As such, they are subject of intense research both in terms of performance as well as of miniaturization and costs.
From the circuit point of view, two major types of beamforming networks, the active and the passive ones, can be distinguished.
The active beamformers have several drawbacks when used in conjunction with a large number of radiating elements. The most prominent drawback is the fact that the beamformers complexity, required space, and costs grow linear with the number of elements. For a large number of antenna beams the networks become complex, costly and not amenable to realization. The salient advantage of such systems is flexibility in generating any specific radiation pattern.

The alternative solution to active beamforming is passive beamforming. A comprehensive overview of the existing passive beamforming networks can be found in [3]. Low cost, compact size, and simultaneous processing of the separate space sectors are the main advantages over the active beamforming

networks. A passive beamforming network differs from an electronic scanning array in that it has one port for each discreet beam. If a separate transmit or receive system is connected to each port, simultaneous independent operations in different space directions can be obtained. Addressing the different space sectors at the same time leads to a higher system channel capacity (especially communication systems based on SDMA) by re-using the time, code and frequency.
Over the years two passive beamforming networks prevailed: the Rotman lens [4] and the Butler matrix [5].

The Rotman lens uses different propagation paths within one structure to provide for different feeding points a unique linear phase shift at the output ports. Using the lens very compact and cheap multi-beam system can be realized at higher frequencies. Unfortunately, at lower microwave frequencies the Rotman lens becomes quite large and difficult to integrate in compact transceiver designs.
To overcome this problem and make the Rotman lens amenable to higher integration, this work introduces a novel lens design using multi-dielectric lenses and folded Rotman lenses. This way the application can be extended in to lower frequencies.

An alternative to the Rotman lens is the Butler matrix. This beamformer is composed of discret components like transmission lines, power splitters, and combiners assembled into a matrix structure to provide linear phase shifts at the output ports. Since highly integrated RF/millimeter wave front ends with a large number of radiation beams require many elements, the realization of a Butler matrix as planar beamformer is virtually impossible. This work addresses the complexity and size problems using the low temperature cofired ceramics (LTCC) technology. Already a matrix using one stripline will provide a solution for geometrical limitations of the standard microstrip implementations. However, using only a few layers of LTCC tape the full potential for 3D integration cannot be exploited. Therefore, a novel design based on folding and stacking the Butler matrix elements will be presented. The geometry of this matrix leads to a significant size reduction by maintaining excellent electrical performance, thus providing a true 3D integration of the Butler matrix concept.

1.2 Background

1.2.1 Rotman lens

The beamformer networks based on Ruze, Rotman, and parallel-plate (R-KR) lens-type structures are the most commonly used lens-based beamformers in multi beam systems [3]. Of the existing lenses, the dielectric lenses such as a the Luneburg lens are the most expensive and complex to manufacture at millimeter-wave frequencies [6],[7]. Therefore, the first choice in large antenna arrays is a Rotman/Ruze lens based beamformer.
Ruze [8] introduced the design of a lens using two focal points. The Rotman lens was developed by Rotman and Turner [4, 9] in 1963. Later, Shelton [10] simplified the design equations using symmetrical lens arcs. Nevertheless, the design options remained constrained and Katagi extended the Rotman lens to allow different values of focal angle and scan angle [11]. Additional improvements of dielectric guiding were presented in [11, 12]. Hansen [13] used a set of compact formulas for designing the Rotman lens and discussed the influence of the design parameters on the lens shape. Simon [14] extended this set of design formulas with a useful approximation for the mutual coupling between arbitrary beam and array ports, from which the lens amplitude, phase errors, and the far-field array factor can be calculated.

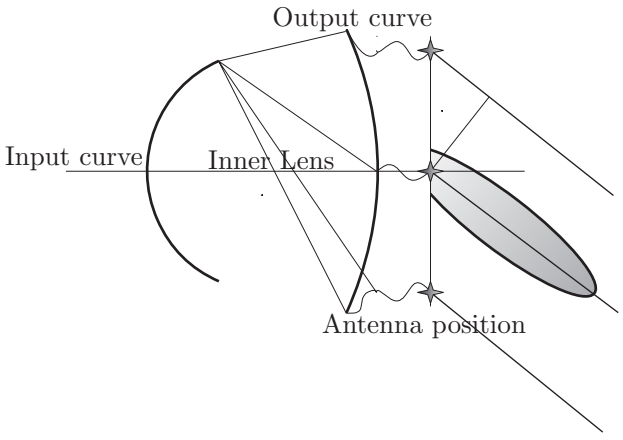

Figure 1-1 Functional schematic of a Rotman lens

The Rotman lens is a constrained multiple-beamforming feed network, most commonly employed in arrays of radiating antenna elements. As such, the lens in Figure 1-1 generates at its output curve an amplitude and phase distribution, which produces multiple simultaneous beams covering different space sectors. For the same beam-pointing direction, each beam produced by the lens ideally has the gain of a single-beam array of the same size and illumination. For each beam, a separate input port (beam port) is provided at the input curves of the lens. The lens was originally constructed of parallel plates that transmit the wave between the beam ports and the array ports. Archer [15] developed a microstrip version of this lens. In all implementations, the arcs and their surfaces are shaped to provide the required phase shifts in the array ports for all the beam ports. In addition to simultaneous availability of many beams, the advantages of Rotman lenses include monolithic construction, ease of manufacture, low cost, and lightweight. The lens can be designed as a true time-delay device, resulting in frequency-independent beam steering and – consequently – very good wideband properties.

The majority of Rotman lenses in use nowadays is designed and built in microstrip technology as opposed to the former waveguide structures. Planar microstrip lenses on a dielectric substrate reduce circuit size and manufacturing complexity due to the simple etching process. The technology provides the advantage of low cost, compact and low profile design, and ease of integration with other circuit components. In the following section, we will focus on microstrip technology; however, the lens-design guidelines developed apply generally, and are not limited to any particular technology.

The port design is an exception because the ports act as the interfaces to the connecting signal-distribution lines and therefore have to be designed and built in the technology of the lines.

For good performance of any lens it is required to take into account also the geometry and placement of all the ports. Investigations of the port orientations and the transitions from a $50\,\Omega$ microstrip line to the parallel-plate aperture of the lens have been done by Musa and Smith [16]. They proved that a linear transition with a flare angle of 12.5° has no significant difference in performance compared to a flare angle of 7.5°. Both designs exhibit an average reflection coefficient of about -15 to -18dB. Whereas a

port with higher flare angle shows a strong increase in the average reflection coefficient. Therefore, a flare angle not larger than 15° should be chosen for the ports. On the other side, the ports should be layed out close together, in order to avoid reflections from any open boundaries along the lens contours.
At this point, additional ports –called dummy ports – are usually placed between the array-port and the beam-port contours to reduce possible reflections and the afferent standing-wave patterns along the lens. The standing waves would generate additional, hardly quantifiable phase and amplitude errors and therefore deteriorate the lens performance.

The desirable performance characteristics and the availability of mature analysis techniques for the realization in various technologies make the Rotman lens today an attractive candidate for use in any discrete multi-beam systems. As a result, the device is widely used in various radar and communication systems [17-19]. The size reduction, packaging, and integration using new technologies are the remaining frontiers of the Rotman lens applications and will be addressed in this work.

1.2.2 Blass and Butler matrix

Beamformers composed of discrete components like transmission lines, power dividers and combiner, which, assembled into a matrix structure, form multiple beams, are the alternative to the lens type of beamforming. Either transmission lines of different length or other dedicated phase shifters provide the phase shifts required for these matrices to produce beam scanning. The power combiners and dividers can be chosen from the pool of passive devices available depending on the technology employed.
Two main types of network based beamformers, used in practical realizations are the Blass [20] and Butler matrix [5]. The Blass matrix is more flexible than the Butler matrix with respect to the phase distribution, but has a considerable disadvantage - the increased loss due to the presence of terminated lines.
Comparing the Blass and the Butler matrix will help to distinguish the advantages and explain the increased usage of the Butler matrix. The Blass Matrix consists of a number of rows and columns, as depicted in Figure 1-2. The number of rows corresponds to the number of wanted beams. The columns are used to interconnect all the input ports to the radiating elements.

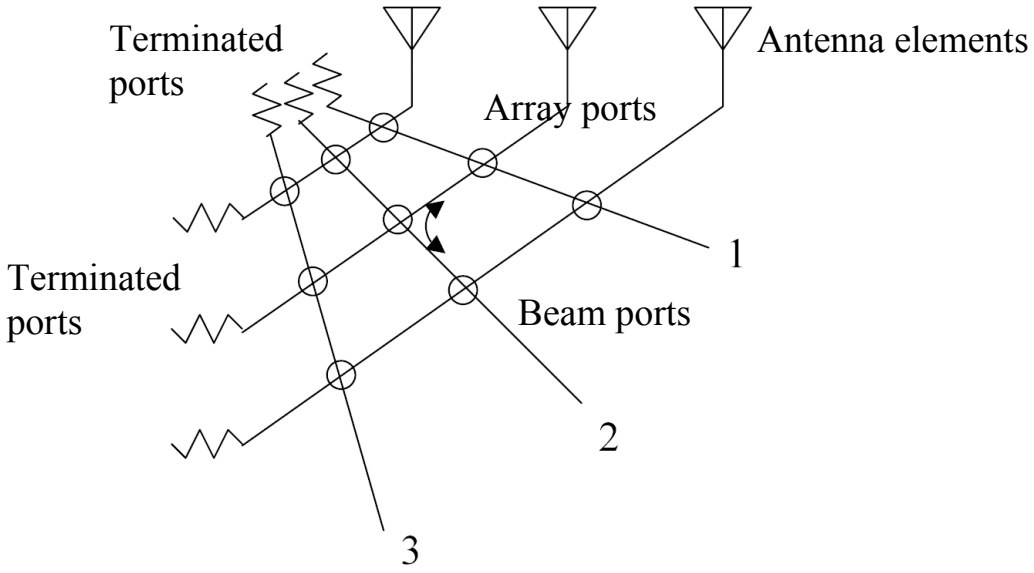

Figure 1-2 Schematic of a Blass matrix

All the rows and columns of the matrix are connected with a crossover realized by a directional cross coupler. Signals applied at each input port propagate along the corresponding feed lines, terminated by a matched load to avoid signal reflections. At each crossover, a small portion of the signal is coupled into each column exciting the corresponding radiating element. A directional coupler is designed to have a stronger transmission through the straightforward line than to the branch arm. The path lengths between the input and the radiating element determine the beam direction, whereas the power distribution throughout the array is controlled by the coupling coefficients.

The main quality of the Blass matrix is the capability to generate multiple beams placed in arbitrary directions and covering a wide scanning range. However, the Blass matrix also has two important drawbacks, setting the limit on the performance and making it difficult to be implemented. The first drawback is the presence of matched loads at the end of each line. This leads to more loss compared to the Butler Matrix. The best reported Blass matrices have a theoretical efficiency of 80% [21] and [22]. This efficiency can be achieved only by controlling the coupling at the crossings. The coupling coefficient varies in this design [21] from -7dB to -28.77dB and is a considerable constraint of the design problem.

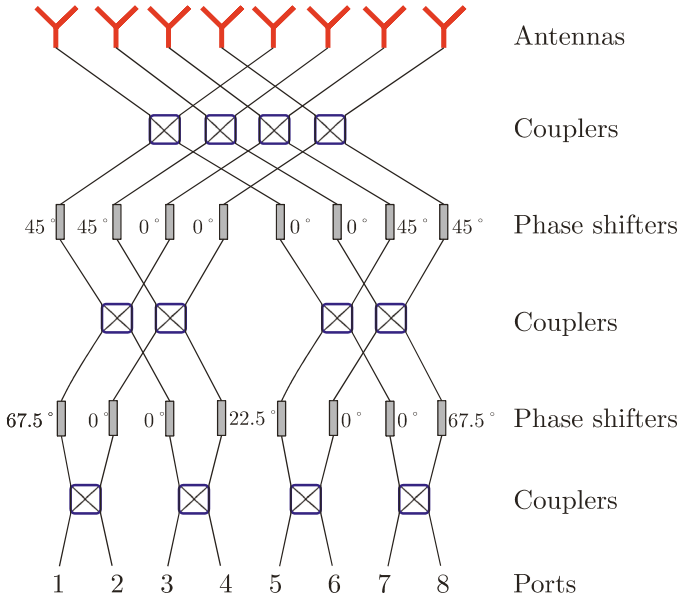

Figure 1-3 Schematic of an 8x8 Butler Matrix

The second and more important drawback is the interaction between the feeding lines. The first beam port is an exception having a high isolation due to the high directivity of the couplers. The excitation of the other ports produces second order beams due to the presence of multiple paths inside the matrix.

Compared to the Blass matrix the Butler matrix has a full power transmission to the antenna array. The Butler matrix is build by interconnecting fixed phase shift sections and 3 dB couplers as shown in Figure 1-3 with an 8x8 matrix. This matrix requires a lower number of couplers and crossings compared to the Blass matrix. Especially when looking at the directional couplers, it is clear that designing one single 3dB coupler can not compare with designing (*N*x*N*) directional couplers (*N* being the number of input and output ports).

So, despite the apparent strengths, the Blass matrix proves to have major drawbacks in terms of number of components, design effort, and especially losses, which will even increase with the size of the matrix. The small number of practical designs reported until today sustains this statement.

Butler matrix as minimal beamforming network

The Butler matrix has been introduced for the first time by Butler and Lowe [5] in 1961. It was conceived as a beam-forming network composed of a set of directional couplers and phase shifters for feeding an antenna array. In 1968 Shelton [23] talked about the parallelism between the Butler matrix and the fast Fourier transform (FFT) in computer science. For the first time the analogy between the Butler matrix and the FFT algorithm is made. Chronologically the Butler matrix precedes the mathematical FFT algorithm by some years. This interesting fact has lead Shelton to the conclusion that interdisciplinary thinking is of major importance.
The analogy of the Butler matrix and the FFT is of key importance for the realization of compact and optimal beamforming networks. The implication can be made clear also by drawing the similarities between the Blass matrix and the discrete Fourier transform (DFT). Shelton is using the term "slow" Fourier transform [23] for what later on will be called the DFT. In order to see again the difference in terms of complexity between the Blass and the Butler matrix one only has to compare the DFT with the FFT from the mathematical perspective.

DFT and FFT algorithms applied to beamforming

The DFT can take considerable time to compute, the time taken being proportional to the square of the number of ports (or of points in the series). Cooley and Tukey [24] have developed a much faster algorithm, called the fast Fourier transform in 1965. The only requirement of the most popular implementation of this algorithm (Radix-2 Cooley-Tukey) is that the number of ports (or points in the series) be a power of two. The computing time for the radix-2 FFT is proportional to the numbers of operations needed:

$$O = N \log_2 N \tag{1.1}$$

N is the number of points in the mathematical series or ports in a beam-forming network. For example, a Butler matrix would relate N input with N output ports (NxN order of the matrix). The number of the input and output ports is limited to an integer power of two as given by (1.2).

$$N = 2^a; \forall a > 1 \tag{1.2}$$

Compared to the radix-2 FFT the DFT needs $O = N^2$ operations. For example, a transform on 1024 points using the DFT takes about 100 times

longer than using the FFT, a significant speed difference. The computation speed relates directly to the network complexity.

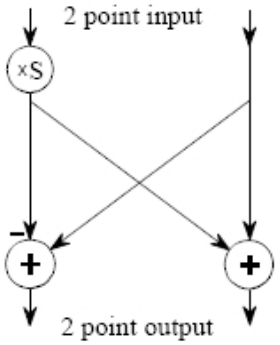

Figure 1-4 Schematic of an 4-point FFT

Now, considering that an RF circuit, as an analog computer, performs the above computation. Multiplication with an exponent in the mathematical space corresponds to a phase shift, which can be realized with a discrete phase shifters. A junction point of the FFT scheme corresponds to either a power divider or a power combiner. Thus, an RF circuit has the same number of phase shifters as the FFT has multiplications. This implies that a beam-forming network with reduced number of phase shifters and combiners can be realized following the FFT algorithm. The full DFT approach corresponds to the Blass matrix with N^2 couplers and phase shifter. It can be therefore labeled as "slow" Fourier transform.

In [25], the derivation of the Butler matrix from the general FFT algorithm is done systematically and can be followed easily. This derivation includes the matrix based on hybrids instead of simple power splitters and combiners. Using 4-port hybrid directional couplers is preferable because hybrids have better port-to-port isolation than Wilkinson power dividers. Consequently, the loss and circuit size can be reduced. A hybrid is a 4-port network and can replace two power dividers and two power combiners at the same time. This reduces the component of the analogue FFT to $O = 0.5N \log_2 N$ phase shifters and couplers. Therefore, the hybrid matrix is the most popular beam-forming matrix.

This work will combine the theoretical background of the FFT with the practical realization. In addition, a new integration technology using LTCC is presented as a toolbox for more compact and complex beam-forming networks.

1.2.3 Objective of this dissertation

In the first part of the dissertation, the analytical formulation for a simple model of the Rotman lens on non-uniform substrates is introduced. The effort is motivated by the expected size reduction and increased efficiency of the lens. Introducing dielectric regions of different permittivity within the lens creates an additional refraction inside the lens and, therefore, an additional focus onto the array ports.
The high space requirements of the Rotman lens can be reduced using non-uniform substrates. The size depends also on the tapered input and output ports as well as the absorbing sidewalls. When used in a compact system this can be a major drawback. In order to make the design more compact, a new folded design of the Rotman lens is introduced. The size reduction of the non-uniform substrate and the multiple geometrical folding of the lens extend the application frontier of this lens structure to new multiple beam systems.

In the second part, the focus of the thesis is a realization of a Butler matrix based on hybrid directional couplers, using new geometrical configurations and maintaining a high bandwidth. These practical designs try to overcome one major issue left in the FFT algorithm, the geometrically dense crossings of the signal lines. The previously described mathematical scheme accounts only for the operation, which determines the speed of the algorithm in a digital version. An analog implementation depends on the physical realization of the dividers and combiners as well as the placement of the numerous signal crossings. The dividers and combiners have to be interconnected in an efficient way using the available space. The novelty of the next three presented designs is in the routing of the signals by using the multilayer feature of LTCC. This routing allows, for the first time, the realization of a more compact and higher order Butler matrix in an elegant way. The novel realization of a Butler matrix using LTCC will be discussed in the second part of the thesis.
The popularity of the Butler matrix and the non-uniformly folded Rotman lens will benefit from the novel multilayer 3D integration.

1.3 Overview

The next seven chapters of this dissertation are outlined below:

Chapter 2 presents the design equation for the conventional Rotman lens and the detailed equations of the split-dielectric lenses. Parametric and error analysis of the conventional and the new lens structures are investigated.
Chapter 3 reports the results of the full-wave simulation of split-dielectric lenses and compares them to the conventional lens. Two lenses are realized on split-dielectric to validate the design methodology. Measurements and simulation are reported.
Chapter 4 describes the design of a folded Rotman lens based on a wideband stripline transition between the various LTCC layers. Current distribution and array factor of the folded Rotman lens are simulated and compared with the unfolded design. A double folded Rotman lens is realized in LTCC and measurements are compared to simulation results.
Chapter 5 describes a novel stripline configuration of an 8x8-port Butler matrix centered at 5 GHz. LTCC is used for the first time to implement the Butler matrix components: couplers, phase shifters, and, especially the crossings.
Chapter 6 introduces a Butler matrix, which takes full advantage of the 3D packaging capability of LTCC. The novelty described lies in the folding and stacking of phase shifters and couplers on 40 layers of LTCC tape to reduce the lateral dimensions of the previously described 5GHz Butler matrix.
Chapter 7 reports a Butler matrix at 60GHz using a standard LTCC tape process. The dimensions of the new Butler matrix scale down with the frequencies maintaining the beamforming capabilities over a bandwidth of 10GHz.
Chapter 8 summarizes the findings of this thesis and gives directions for possible future work.

Chapter 2

Lens with non-uniform substrates

Abstract - In this chapter, the analytical formulation for the Rotman lens on non-uniform substrates is introduced. The effort is motivated by the expected size reduction and increased efficiency of the lens.

2.1 Introduction

Implementing dielectric regions of different permittivity within the conventional Rotman lens creates an additional refraction inside the lens. With this design, less power is lost on the terminated dummy ports and – more importantly – the lens size is reduced while the performance characteristics are maintained.
Investigations of the power distribution within the lens and the scanning properties of the lens are carried out. The new design methodology has more degrees of freedom than the conventional Rotman-lens design procedure. This allows reducing the size of the lens compared with the conventional Rotman-lens design for a fixed mean phase error

2.2 Conventional Rotman lens

This section summarizes the design procedure of the conventional Rotman lens. In the first part of the section, the lens contours and port positions are calculated from the path-length equality equations. In the second part, the effects of the lens design parameters on the lens shape and port positions are analyzed.

2.2.1 Design equations for conventional Rotman lens

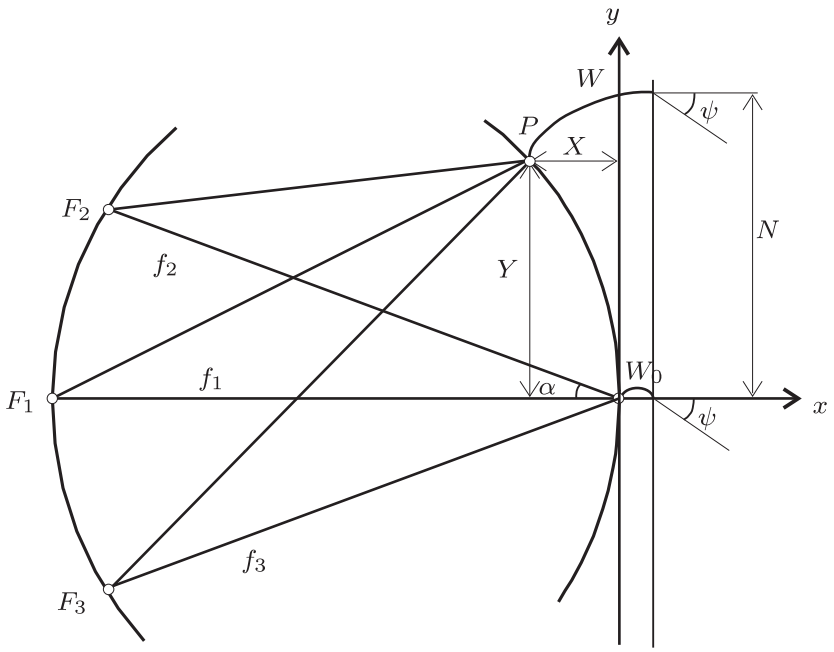

Figure 2-1 General Rotman lens parameters

Designing the conventional Rotman lens requires to solve three path-length equality equations and three additional equations related to the geometry. The path-length equality equations are solved for three points defining the beam-port positions for beam-scan angles 0 and $\pm\psi$. Since these are the only points that exactly fulfill the path-length equations, they are also referred to as perfect focal points. Using the nomenclature of Figure 2-1, the three equations corresponding to the path-length equality are

$$\begin{aligned} \overrightarrow{F_1P} + W &= f_1 + W_0 \\ \overrightarrow{F_2P} + W + N\sin\psi &= f_2 + W_0 \\ \overrightarrow{F_3P} + W - N\sin\psi &= f_3 + W_0 . \end{aligned} \tag{2.1}$$

Due to the symmetry of the off-axis focal points F_2 and F_3 with respect to the x-axis, it follows that $f_2 = f_3$.

The path lengths from the perfect focal points to the point $P = (-X, Y)$ can be derived directly from the geometry:

$$\begin{cases} \overrightarrow{F_1P}^2 &= (f_1 - X)^2 + Y^2 \\ \overrightarrow{F_2P}^2 &= (f_2\cos\alpha - X)^2 + (Y - f_2\sin\alpha)^2 . \\ \overrightarrow{F_3P}^2 &= (f_2\cos\alpha - X)^2 + (Y + f_2\sin\alpha)^2 \end{cases} \quad (2.2)$$

Array-port contour calculation

The lens contour on the array side is determined by calculating the position of the array port $P = (-X, Y)$ corresponding to one element of the antenna array. The positions of the array ports is derived from the three perfect focal points F_1, F_2 and F_3.

Combining (2.1) and (2.2) and defining $\widetilde{W} = W - W_0$ to be the absolute phase to inserted between the output ports of the lens and the input of the antennas yields

$$f_1^2 - 2f_1\widetilde{W} + \widetilde{W}^2 = X^2 + Y^2 + f_1^2 - 2f_1X \quad (2.3)$$

$$f_2^2 + \widetilde{W}^2 + N^2\sin^2\psi - 2f_2\widetilde{W} - 2f_2N\sin\psi + 2\widetilde{W}N\sin\psi = X^2 + Y^2 + f_2{}^2 - 2Xf_2\cos\alpha - 2Yf_2\sin\alpha \quad (2.4)$$

$$f_2^2 + \widetilde{W}^2 + N^2\sin^2\psi - 2f_2\widetilde{W} + 2f_2N\sin\psi - 2\widetilde{W}N\sin\psi = X^2 + Y^2 + f_2{}^2 - 2Xf_2\cos\alpha + 2Yf_2\sin\alpha \quad (2.5)$$

Subtracting (2.4) from equation (2.5) yields

$$f_2N\gamma\sin\alpha - \widetilde{W}N\gamma\sin\alpha = Yf_2\sin\alpha \quad (2.6)$$

The ratio of the scan angle ψ to the ray angle α is given by $\gamma = \dfrac{\sin\psi}{\sin\alpha}$

The ordinate Y of point P can be written as

$$Y = N\gamma\left(1 - \frac{\widetilde{W}}{f_2}\right) \quad (2.7)$$

Adding (2.4) and(2.5) results in

$$\widetilde{W}^2 + N^2\gamma^2\sin^2\alpha - 2f_2\widetilde{W} = X^2 + Y^2 - 2Xf_2\cos\alpha \qquad (2.8)$$

Subtracting (2.3) from (2.8) yields

$$2f_1\widetilde{W} + N^2\gamma^2\sin^2\alpha - 2f_2\widetilde{W} = 2Xf_1 - 2Xf_2\cos\alpha \qquad (2.9)$$

or

$$X = \frac{(f_1 - f_2)\widetilde{W} + \frac{1}{2}N^2\gamma^2\sin^2\alpha}{f_1 - f_2\cos\alpha} \qquad (2.10)$$

Replacing X and Y in (2.3) results in a quadratic equation for $\widetilde{W}$:

$$A\widetilde{W}^2 + B\widetilde{W} + C = 0 \qquad (2.11)$$

Where

$$\begin{aligned} A &= f_1 - \frac{(f_1 - f_2)^2}{(f_1 - f_2\cos\alpha)^2} - \frac{N^2\gamma^2}{f_2{}^2} \\ B &= -2f_1 + \frac{2N^2\gamma^2}{f_2} + \frac{(f_1 - f_2)N^2\gamma^2\sin^2\alpha}{(f_1 - f_2\cos\alpha)^2} + \frac{2(f_1 - f_2)}{f_1 - f_2\cos\alpha} \\ C &= -N^2\gamma^2 + \frac{N^2\gamma^2\sin^2\alpha}{f_1 - f_2\cos\alpha} - \frac{N^4\gamma^4\sin^4\alpha}{4(f_1 - f_2\cos\alpha)^2} \end{aligned} \qquad (2.12)$$

At this point, a set of parameters that are normalized relative by the focal length f_1 is defined:

$$x = \frac{X}{f_1}, \qquad y = \frac{Y}{f_1}, \qquad w = \frac{\widetilde{W}}{f_1}, \qquad \beta = \frac{f_2}{f_1}, \qquad \zeta = \frac{N\gamma}{f_1}$$

Using these parameters, the quadratic equation for the normalized length w can be written as

$$aw^2 + bw + c = 0 \qquad (2.13)$$

where

$$\begin{aligned} a &= 1-\frac{(1-\beta)^2}{(1-\beta\cos\alpha)^2}-\frac{\zeta^2}{\beta^2} \\ b &= -2+\frac{2\zeta^2}{\beta}+\frac{(1-\beta)\zeta^2\sin^2\alpha}{(1-\beta\cos\alpha)^2}+\frac{2(1-\beta)}{1-\beta\cos\alpha} \\ c &= -\zeta^2+\frac{\zeta^2\sin^2\alpha}{1-\beta\cos\alpha}-\frac{\zeta^4\sin^4\alpha}{4(1-\beta\cos\alpha)^2} \end{aligned} \tag{2.14}$$

Similarly, (2.7) and (2.10) can be written in a normalized form:

$$y=\zeta\left(1-\frac{w}{\beta}\right) \tag{2.15}$$

$$x=\frac{(1-\beta)w+\frac{1}{2}\zeta^2\sin^2\alpha}{1-\beta\cos\alpha} \tag{2.16}$$

For given values of parameters α, β and γ, the normalized electrical length w can be computed as a function of ζ for each antenna element. Substituting these values of w and ζ into (2.15) and (2.16), the position of each connection point P on the array-port contour can be calculated. The locus of the points obtained this way forms the complete array-port contour of the lens.

Beam-port contour calculation

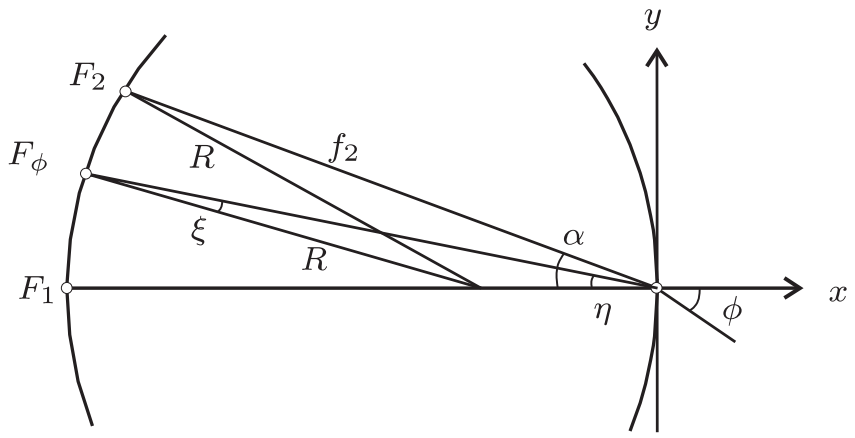

Figure 2-2 Geometrical parameters for beam-port contour calculation

The beam-port contour is selected as part of a circle of radius R, which passes through the three perfect focal points. Referring to Figure 2-2, the radius R can be calculated using the law of cosines:

$$R^2 = (f_1 - R)^2 + f_2^2 - 2(f_1 - R) f_2 \cos\alpha \tag{2.17}$$

Normalizing R relative by f_1 yields

$$r^2 = (1-r)^2 + \beta^2 - 2(1-r)\beta\cos\alpha. \tag{2.18}$$

The normalized radius can also be written as

$$r = \frac{1+\beta^2 - 2\beta\cos\alpha}{2(1-\beta\cos\alpha)}. \tag{2.19}$$

At this point, the position $F_\phi = (-F_{\phi x}, F_{\phi y})$ on the beam-port contour for an input port corresponding to an arbitrary scan angle ϕ can be calculated. The ray angle η corresponding to the desired scan angle ϕ is given by

$$\eta = \arcsin\left(\frac{\sin\phi}{\gamma}\right) \tag{2.20}$$

The angle ξ can be determined using the law of sinus

$$\xi = \arcsin\left(\frac{1-r}{r}\sin\eta\right) \tag{2.21}$$

with

$$\frac{F_{\phi x}}{f_1} = f_{\phi x} = (1-r) + r\cos(\eta + \xi) \tag{2.22}$$

and

$$\frac{F_{\phi y}}{f_1} = f_{\phi x} = r\sin(\eta + \xi) \tag{2.23}$$

Following the previous design equation, the computation of the conventional Rotman-lens contours is straightforward.

2.2.2 Parametric analysis of conventional Rotman lens

When designing a Rotman lens, usually the beam-scan angles, the number of antenna radiating elements, and the element spacing are specified by the

system requirements. The remaining design parameters are α, β, γ and f_1/λ. Thus, the design task is to choose the optimal combination of these parameters. The lens shape – based on the focal length f_1, the beam-port contour, and the array-port contour – has not only an impact on the overall lens size but also on the performance in terms of losses and phase errors. In order to avoid asymmetric amplitude tapers and large phase errors, it is important for the two port contours to be similar in height.
Figure 2-3 and Figure 2-4 show the effects of the design parameters for a lens that operates at 10 GHz. The beam-port contours are on the left-hand side, while the array-port contours are on the right-hand side in the figures. Markers indicate the port positions. The horizontal axis represents the number of free space wavelengths λ_0, whereas the vertical axis is using the element spacing d as a scale, which is for all figures $d = \lambda_0/2$. The depicted lenses have a focal length of $f_1 = 4\lambda_0$ and feature nine beam ports and eleven array ports; the array ports are equally spaced, in order to accommodate a linear antenna array. Asterisks mark the three perfect focal points.

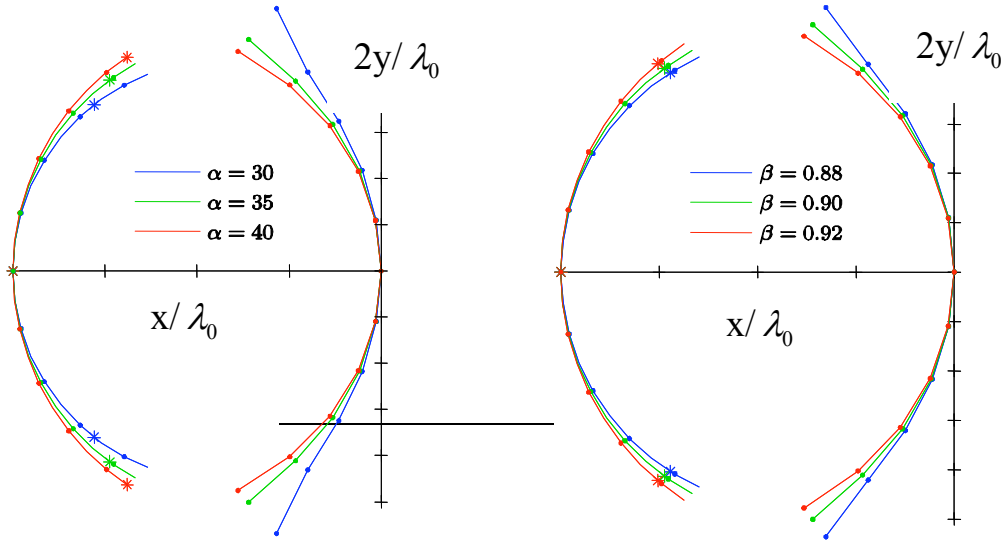

Figure 2-3 a)Variation of angle α while $\beta = 0.9$ b) Variation of β while $\alpha = 35^\circ$. For both $\gamma = 1.1$, $f_1 = 4\lambda_0$, $\varepsilon_r = 6$, $\phi = \pm 10^\circ, 20^\circ, 30^\circ, 40^\circ$

For the first analysis, all parameters except α are fixed. Figure 2-3 illustrates that increasing α opens the beam-port contour and closes the array-port contour. Port positions on the contours remain unchanged, only the off-axis

focal points show distinctive changes in their locations. The value of α should be selected in such a way that the phase error over the aperture is minimized. The value can also be used to equalize the contour heights. Increasing the value of angle β while holding all other parameters fixed, exhibits an effect similar to that obtained previously, i.e., the beam-port contour opens up, and the array-port contour closes. Figure 2-3 shows that the port locations are again unchanged. However, changing the value of β has only a minimal effect on the position of the focal points. Again, the value of β can be chosen in such a way that both port contour heights be equalized. One can identify pairs of α and β values that yield roughly the same lens shape and port positions for any set of the remaining design parameters. Nevertheless, since the positions of the off-axis focal points vary with α, the phase error over the aperture for each beam will be different.

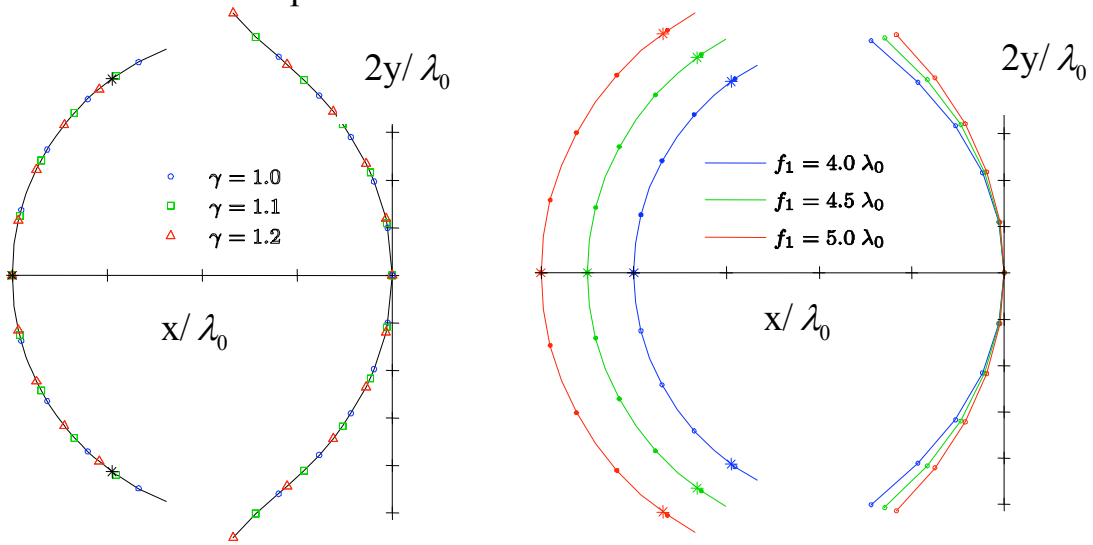

Figure 2-4 a)Effect of angle ratio γ, with $\alpha = 35^\circ$, $\beta = 0.9$, $f_1 = 4\lambda_0$, $\varepsilon_r = 6$, $\phi = \pm 10^\circ, 20^\circ, 30^\circ, 40^\circ$

b) Effect of focal length f_1, with $\alpha = 35^\circ$, $\beta = 0.9$, $\gamma = 1.1$, $\varepsilon_r = 6$, $\phi = \pm 10^\circ, 20^\circ, 30^\circ, 40^\circ$

Varying the value of γ leaves both port contours unchanged. However, increasing the value of γ moves the beam ports closer together, while the array ports are spread apart, as is shown in Figure 2-4. Although the focal points remain fixed, their relative position changes because the port contours also change. Additionally, the value of γ can modify the lengths of both contours.

In Figure 2-4 a) all values of γ are greater than one. This is due to the large maximum scan angle ϕ. For small scan angles, e.g., $\phi_{max} = 30^{\circ}$ values of γ smaller than one are appropriate, as they provide a strongly curved lens.

Increasing the focal length f_1, i.e. the width of the lens, results in a bigger separation between the end ports on the two curves. However, changing f_1 / λ also changes all other dimensions since the lens equations are normalized to f_1. As it is shown in Figure 2-4 b), varying f_1 / λ also changes the array port curve and spacing between the array ports.

2.2.3 Phase-error analysis of conventional Rotman lens

The design procedure described in Section 2.2.1 results in a perfect beam scanning for three angles. These are the scan angles corresponding to the three perfect focal points. For all other points on the beam-port contour, the path-length equalities are not fulfilled. This is equivalent to a phase error – superimposed on top of the desired progressive phase – at the antenna elements. In terms of radiation pattern, the phase error can lead to modified sidelobe levels (SLLs) as well as angular shifts of the main lobe. The target for a wide-angle scanning lens is to have a small phase error not only for the three focal points but also for the other beam ports on the beam-port contour. The path-length error for a beam port F_ϕ, corresponding to a scan angle ϕ, can be expressed as

$$\Delta L = \overrightarrow{F_\phi P} + \widetilde{W} + N\sin(\phi) - \overrightarrow{F_\phi O} \tag{2.24}$$

or

$$\Delta L = \sqrt{(F_{\phi x} - X)^2 + (F_{\phi y} - Y)^2} + \widetilde{W} + N\gamma\sin(\eta) - \frac{F_{\phi x}}{\cos(\eta)} \tag{2.25}$$

Normalizing (2.25) with respect to the focal length f_1 results in

$$\frac{\Delta L}{f_1} = \Delta l = \sqrt{(f_{\phi x} - x)^2 + (f_{\phi y} - y)^2} + w + \zeta\sin(\eta) - \frac{f_{\phi x}}{\cos(\eta)} \tag{2.26}$$

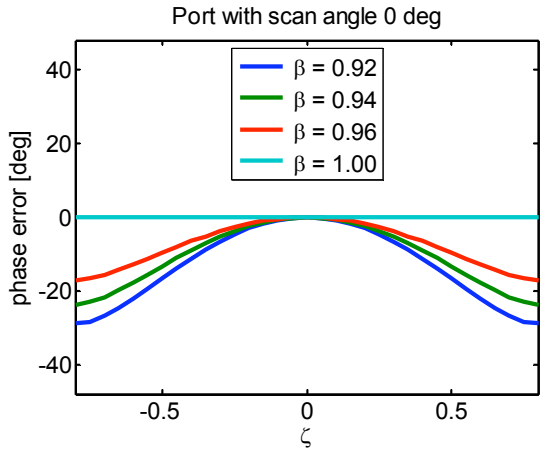

Figure 2-5 Phase error for a beam port with on axis focal point; scan angle $\phi = 0^{\circ}$

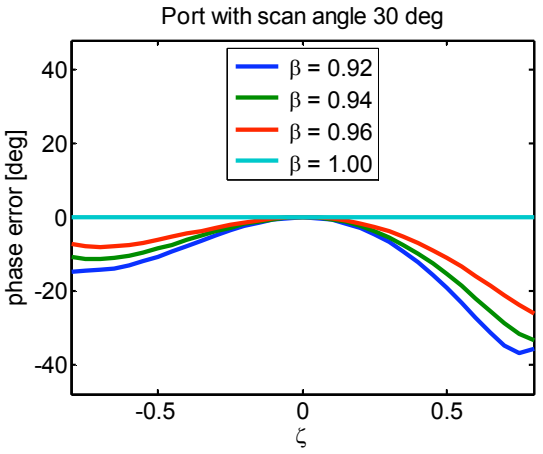

Figure 2-6 Phase error for a beam port at the off-axis focal point; scan angle $\phi = 30^{\circ}$

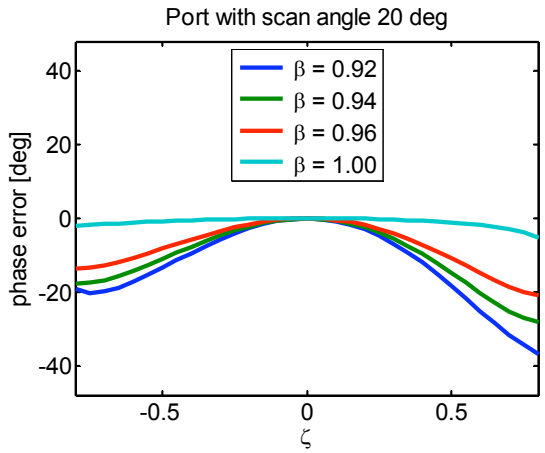

Figure 2-7 Phase error for a beam port between the focal points; scan angle $\phi = 20^{\circ}$

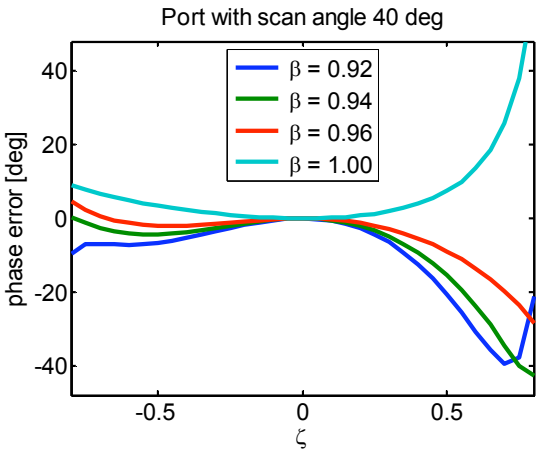

Figure 2-8 Phase error for a beam port outside of the off-axis focal point; scan angle $\phi = 40^{\circ}$

Using (2.13)-(2.23), the normalized path-length error can be expressed as a function of design parameters α, β and ζ and the scan angle. The phase error at the antenna array deteriorates the scanning ability of the Rotman lens. The phase error is given by (2.27) respectively.

$$\Delta\Phi = \frac{\Delta l}{\lambda} \cdot 2\pi \qquad (2.27)$$

In Figure 2-5-Figure 2-8, the phase error is plotted against the normalized scaled aperture size ζ for different values of β. In the plots $\alpha = 30$ degrees and $\gamma = 1$. We distinguish between beam ports located on a focal point (Figure 2-5 and Figure 2-6), beam ports located outside the off-axis focal points (Figure 2-8), and between the focal points (Figure 2-7). As it can be seen in Figure 2-5 and Figure 2-6, the phase error of a beam port located at the focal point vanishes only for $\beta = 1$. Path-length error, respectively phase error, depending on design parameters and scan angles, are also shown in [4, 9], [11, 12] and [13].
In order to get an optimum design for wide-angle scanning, Rotman and Turner [4, 9] suggest choosing β as

$$\beta = \frac{2}{2 + \alpha^2} \qquad (2.28)$$

Hansen [13] shows that an optimum value of β only exists for a certain range of ζ and a fixed ray angle η. In particular, the optimal value of β is different for ray angles between the perfect focal points and ray angles outside of those, which can be seen in the figures above.

2.3 Rotman lens with split substrate

Abstract-This section describes the design procedure for a more compact Rotman lens, built with two and three different substrate segments. The path-length equality equations for the lenses with two and three dielectric substrate segments are derived. The resulting lens is more compact then the conventional Rotman lens. The effects of the design parameters are analyzed with respect to the goal of size reduction.

The design methodology described in section 2.2 is extended to a new type of Rotman lens based on several different substrates. The new lens consists of two or three regions with different relative permittivity. The authors in [26] present for the first time the split-dielectric Rotman lens concept. In contrast to [26], where the dielectric interface contour is wedge shaped, the contour to be analyzed in this work is a straight line. Straight interfaces between the

different dielectrics help to derive an analytical formulation, which will be developed in this work.

The design in [26] proves that a loss reduction can be achieved with this new lens type. As an extention to [26] an in-depth analysis of the multi-dielectric Rotman lens will be undertaken in this chapter. We focus on the analytic formulation of the multi-dielectric lens and the design parameters. Full-wave simulations and measurements of two lenses at 10 GHz demonstrate improved performance characteristics.

The goal of the dielectric staggering inside the lens should be a better focusing, which allows a substantial reduction of the focal length. Advantages and drawbacks of the new Rotman lens design are discussed in this chapter based on different simulated, realized, and measured lenses.

2.3.1 Design of lens with two substrate segments

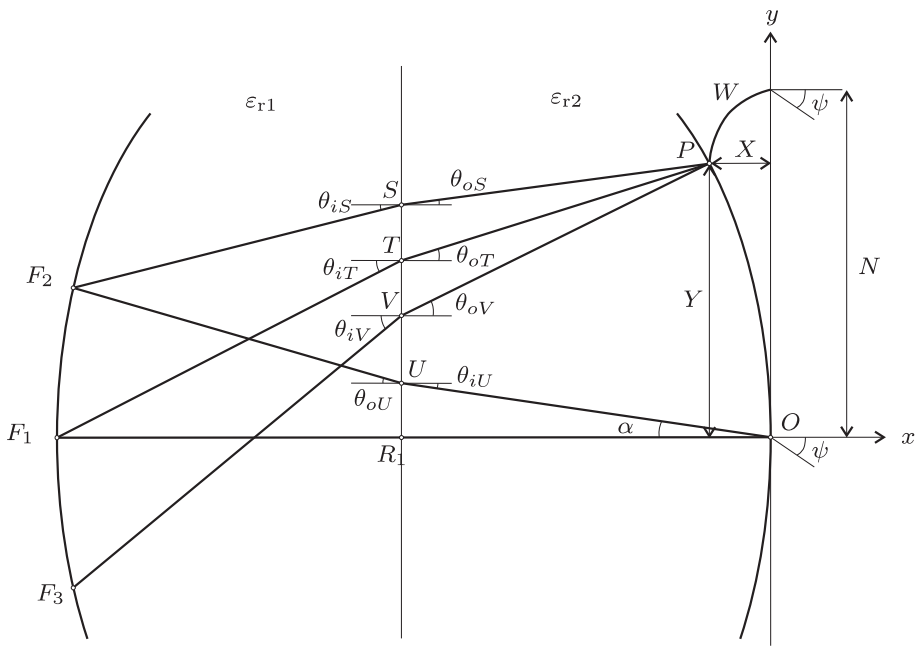

Figure 2-9 Geometrical parameters of lens with split-dielectric

In the design procedure described in this section, the array port positions are calculated based on the three focal points, similar to what is done in the case

of the conventional Rotman lens. Then, the optimum beam port position is calculated in terms of the mean path-length error to all fixed array ports.

The path-length equality equations for the three focal points F_1, F_2 and F_3 for the lens shown in Figure 2-9 become

$$\begin{aligned}
&\overrightarrow{F_1T}\sqrt{\varepsilon_{r1}}+\overrightarrow{TP}\sqrt{\varepsilon_{r2}}+W\sqrt{\varepsilon_{r2}}=\overrightarrow{F_1R_1}\sqrt{\varepsilon_{r1}}+\overrightarrow{R_1O}\sqrt{\varepsilon_{r2}}+W_0\sqrt{\varepsilon_{r2}}\\
&\overrightarrow{F_2S}\sqrt{\varepsilon_{r1}}+\overrightarrow{SP}\sqrt{\varepsilon_{r2}}+W\sqrt{\varepsilon_{r2}}+N\sin\psi=\overrightarrow{F_2U}\sqrt{\varepsilon_{r1}}+\overrightarrow{UO}\sqrt{\varepsilon_{r2}}+W_0\sqrt{\varepsilon_{r2}} \quad (2.29)\\
&\overrightarrow{F_3V}\sqrt{\varepsilon_{r1}}+\overrightarrow{VP}\sqrt{\varepsilon_{r2}}+W\sqrt{\varepsilon_{r2}}-N\sin\psi=\overrightarrow{F_2U}\sqrt{\varepsilon_{r1}}+\overrightarrow{UO}\sqrt{\varepsilon_{r2}}+W_0\sqrt{\varepsilon_{r2}}
\end{aligned}$$

where the symmetry of the focal points F_2 and F_3 is used.
While the design parameters α and γ are the same as they were defined in Chapter 2.2.1 , parameter β has to be adapted to the non-uniform substrate to take the different propagation velocities in the two regions into account. So, β becomes

$$\beta=\frac{\overrightarrow{F_2U}\sqrt{\varepsilon_{r1}}+\overrightarrow{UO}\sqrt{\varepsilon_{r2}}}{\overrightarrow{F_1R_1}\sqrt{\varepsilon_{r1}}+\overrightarrow{R_1O}\sqrt{\varepsilon_{r2}}} \quad (2.30)$$

Since there are two media with different permittivity, a ray passing the media interface is refracted. Therefore, Snell's law has to be applied to get the relation between angle of incidence θ_i and refraction angle θ_t . It is

$$\sin\theta_i = e\sin\theta_t \quad (2.31)$$

where $e=\sqrt{\frac{\varepsilon_{r_2}}{\varepsilon_{r_1}}}$

Considerations should be given to the fact that there are always reflections when passing from one region into another with a different dielectric constant. The part of the field that is transmitted into the second region is given by the transmission coefficient. The transmission coefficient depends on the propagation mode, the angle of incidence, and the dielectric constant ratio. A quantification of the reflection will be done later in simulation and measurements.

Array-port contour calculation

The coordinates of point U are

$$U_x = -R_1 \quad and \quad U_y = R_1 \tan\alpha$$

in addition, $\overrightarrow{UO}$ can be written as

$$\overrightarrow{UO} = \frac{R_1}{\cos\alpha} \tag{2.32}$$

The angle of incidence θ_{oU} on the beam port side of the material interface and the angle of refraction θ_{iU} on the antenna array side at point U are given by

$$\theta_{iU} = \alpha \quad and \quad \theta_{oU} = \arcsin(e\sin\alpha).$$

Further, the coordinates of the off-axis focal point F_2 can be written as

$$F_{2x} = R_1 + \overrightarrow{F_2U}\cos\theta_{iU} \tag{2.33}$$

$$F_{2y} = R_1\tan\alpha + \overrightarrow{F_2U}\sin\theta_{iU}, \tag{2.34}$$

where

$$\overrightarrow{F_2U} = \beta\left((F_1 - R_1) + eR_1\right) - \frac{eR_1}{\cos\alpha} \tag{2.35}$$

can be derived from (2.30). Now, the remaining lengths from (2.29) are given as follows

$$\begin{aligned}
\overrightarrow{F_1T} &= \frac{F_1 - R_1}{\cos\theta_{iT}} \\
\overrightarrow{TP} &= \sqrt{(R_1 - X)^2 + (Y - (F_1 - R_1)\tan\theta_{iT})^2} \\
\overrightarrow{F_2S} &= \frac{F_{2x} - R_1}{\cos\theta_{iS}} \\
\overrightarrow{SP} &= \sqrt{(R_1 - X)^2 + (Y - ((F_{2x} - R_1)\tan\theta_{iS} + F_{2y}))^2} \\
\overrightarrow{F_3V} &= \frac{F_{2x} - R_1}{\cos\theta_{iV}} \\
\overrightarrow{VP} &= \sqrt{(R_1 - X)^2 + (Y - \left((F_{2x} - R_1)\tan\theta_{iV} - F_{2y}\right))^2}
\end{aligned} \tag{2.36}$$

Substituting these lengths in the path-length equality equations (2.29) yields the following three equations for the three parameters X, Y, and $\widetilde{W}$ of the array-side lens contour.

$$\begin{aligned}
&\frac{FR}{\cos\theta_{iT}}\sqrt{\varepsilon_{r1}} + \sqrt{(R_1 - X)^2 + (Y - FR\tan\theta_{iT})^2}\sqrt{\varepsilon_{r2}} + \\
&+\widetilde{W}\sqrt{\varepsilon_{r2}} - C_1 = 0
\end{aligned} \tag{2.37}$$

$$\begin{aligned}
&\frac{FXR}{\cos\theta_{iS}}\sqrt{\varepsilon_{r1}} + \sqrt{(R_1 - X)^2 + (Y - (FXR\tan\theta_{iS} + F_{2y}))^2}\sqrt{\varepsilon_{r2}} + \\
&+\widetilde{W}\sqrt{\varepsilon_{r2}} - C_2 + C_3 = 0
\end{aligned} \tag{2.38}$$

$$\begin{aligned}
&\frac{FXR}{\cos\theta_{iV}}\sqrt{\varepsilon_{r1}} + \sqrt{(R_1 - X)^2 + (Y - (FXR\tan\theta_{iV} - F_{2y}))^2}\sqrt{\varepsilon_{r2}} + \\
&+\widetilde{W}\sqrt{\varepsilon_{r2}} - C_2 - C_3 = 0
\end{aligned} \tag{2.39}$$

where the following abbreviations are used

$$\begin{aligned}
FR &= F_1 - R_1 \quad FXR = F_{2x} - R_1 \quad \widetilde{W} = W - W_0 \\
C_1 &= FR\sqrt{\varepsilon_{r1}} \quad C_2 = \overrightarrow{F_2U}\sqrt{\varepsilon_{r1}} + \overrightarrow{UO}\sqrt{\varepsilon_{r2}} \quad C_3 = N\sin\psi
\end{aligned} \tag{2.40}$$

The computation of the array-side lens contour is completed by solving these three equations for each of the antenna elements.

Beam-port contour calculation

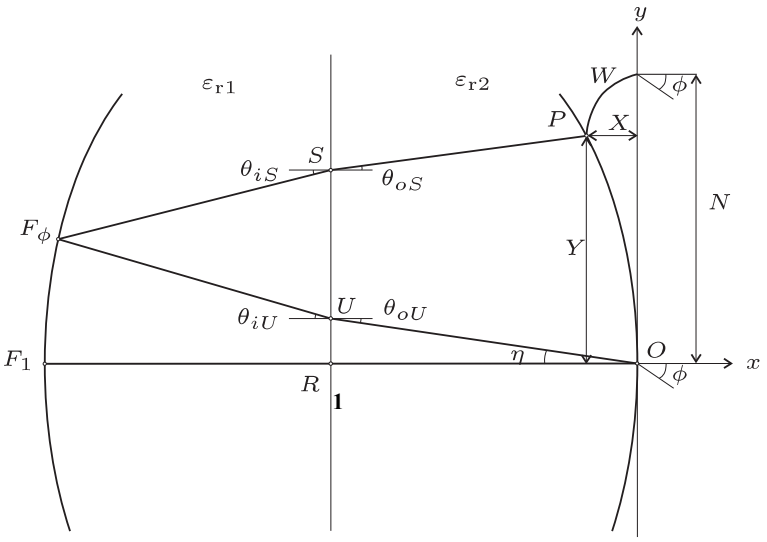

Figure 2-10 Geometrical parameters of lens with split dielectric for beam-port contour calculation

In contrast to the conventional Rotman lens, the assumption that the beam ports lie on an arc through the three focal points has been modified. The ports are placed in the positions with the smallest mean quadratic path-length error to all array ports. The calculation of the beam port position F_ϕ corresponding to a scan angle ϕ, as it is shown in Figure 2-10, is described in the following steps.
The ordinate $F_{\phi y}$ can be written as

$$F_{\phi y} = R_1 \tan\eta + (F_{\phi x} - R_1)\tan\theta_{iU}, \qquad (2.41)$$

with

$$\sin\eta = \frac{\sin\phi}{\gamma} \quad and \quad \sin\theta_{iU} = e\sin\eta.$$

Another relation for $F_{\phi y}$ is

$$F_{\phi y} = Y - (R_1 - X)\tan\theta_{oS} - (F_{\phi x} - R_1)\tan\theta_{iS}. \tag{2.42}$$

Solving (2.41) and (2.42)for the beam port position yields

$$\begin{aligned} F_{\phi x} &= \frac{Y + X\tan\theta_{oS} - (\tan\eta - \tan\theta_{iS} - \tan\theta_{iU} + \tan\theta_{oS})}{\tan\theta_{iS} + \tan\theta_{iU}} \\ F_{\phi y} &= \frac{\tan\theta_{iU}(Y + X\tan\theta_{oS}) + R_1(\tan\eta\tan\theta_{iS} - \tan\theta_{iU}\tan\theta_{oS})}{\tan\theta_{iS} + \tan\theta_{iU}} \end{aligned} \tag{2.43}$$

Together with the four lengths

$$\begin{aligned} \overrightarrow{UO} &= \frac{R_1}{\cos\eta} \\ \overrightarrow{F_\phi U} &= \frac{F_{\phi x} - R_1}{\cos\theta_{iU}} \\ \overrightarrow{F_\phi S} &= \frac{F_{\phi x} - R_1}{\cos\theta_{iS}} \\ \overrightarrow{SP} &= \frac{R_1 - X}{cos\theta_{oS}} \end{aligned} \tag{2.44}$$

the expression for the path-length error from this beam port F_ϕ to the antenna element with array port $P = (-X, Y)$ can be found as

$$\Delta L = \overrightarrow{F_\phi S}\sqrt{\varepsilon_{r1}} + (\overrightarrow{SP} + \widetilde{W})\sqrt{\varepsilon_{r2}} + N\sin\phi - \overrightarrow{F_\phi U}\sqrt{\varepsilon_{r1}} - \overrightarrow{UO}\sqrt{\varepsilon_{r2}} \tag{2.45}$$

Now, the position F_ϕ of the beam port for a scan angle ϕ is determined by minimizing the sum over the quadratic path-length errors to all array ports P_k.

$$\begin{aligned} F_\phi = argmin_{F_\phi} \sum_{k=1}^{NE} \Big[& \overrightarrow{F_\phi S}_k \sqrt{\varepsilon_{r1}} + (\overrightarrow{SP}_k + \widetilde{W}_k)\sqrt{\varepsilon_{r2}} + \\ & + N_k \sin\phi - \overrightarrow{F_\phi U}\sqrt{\varepsilon_{r1}} - \overrightarrow{UO}\sqrt{\varepsilon_{r2}} \Big]^2 \end{aligned} \tag{2.46}$$

2.3.2 Parametric analysis of Rotman lens with split substrate

In this section, the effects of the different design parameters on lens shape and port positions of the new Rotman lens with non-uniform substrate are discussed. Similarly, to the conventional Rotman lens, scan angles, the number of antenna elements, and the element spacing are usually specified from the system requirements. The remaining design parameters are α, β, γ, f_1/λ and the new parameters R_1, ε_{r1} and ε_{r2}. Thus, the task is to choose the optimal combination of these six design parameters.
Figure 2-11-Figure 2-12 show the effects of the design parameters for Rotman lenses on a non-uniform substrate. All lenses have nine beam ports and eleven array ports. The axis notation is maintained from the previous chapter. The interface between the two regions with different dielectric constant is placed in the middle of the lens width, i.e. $R_1 = 0.5 f_1$. Even though the lenses with the new design can be designed much smaller, Figure 2-11 shows lenses of the same width as those in the previous chapter for a better comparison of different lenses.

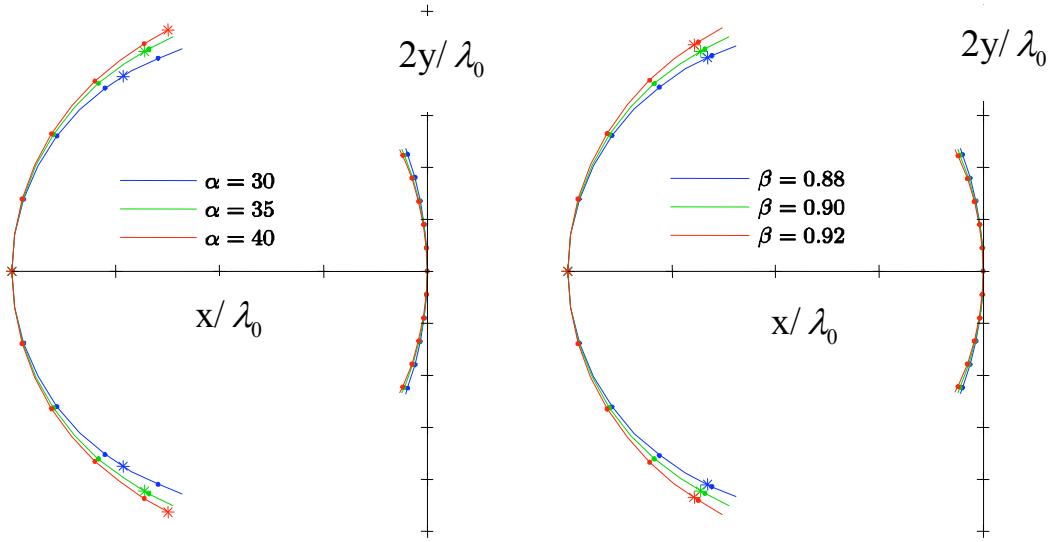

Figure 2-11 a) Effect of ray angle α, with $\gamma = 1.1$, $\beta = 0.9$, $f_1 = 4\lambda_0$, $R_1 = 0.5 f_1$, $\varepsilon_{r1} = 4$, $\varepsilon_{r2} = 6$, $\phi = \pm 10^\circ, 20^\circ, 30^\circ, 40^\circ$.

b) Effect of focal ratio β, with $\gamma = 1.1$, $\alpha = 35$, $f_1 = 4\lambda_0$, $R_1 = 0.5 f_1$, $\varepsilon_{r1} = 4$, $\varepsilon_{r2} = 6$, $\phi = \pm 10^\circ, 20^\circ, 30^\circ, 40^\circ$.

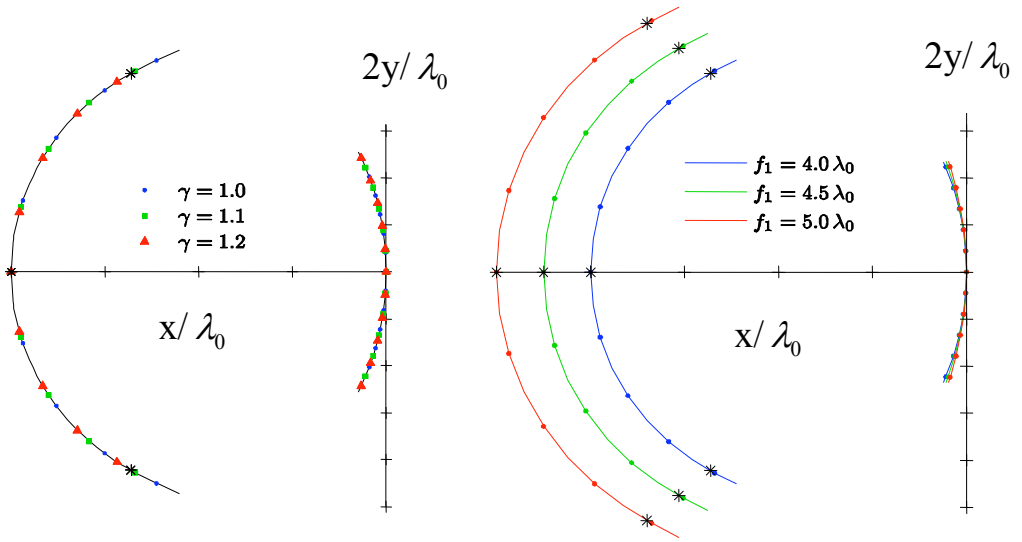

Figure 2-12 a) Effect of angle ratio γ, with $\alpha = 35$, $\beta = 0.9$, $R_1 = 0.5 f_1$, $\varepsilon_{r1} = 4$, $\varepsilon_{r2} = 6$, $\phi = \pm 10^\circ, 20^\circ, 30^\circ, 40^\circ$

b)Effect of focal length f_1, with $\alpha = 35$, $\beta = 0.9$, $\gamma = 1.1$, $R_1 = 0.5 f_1$, $\varepsilon_{r1} = 4$, $\varepsilon_{r2} = 6$, $\phi = \pm 10^\circ, 20^\circ, 30^\circ, 40^\circ$

Varying the design parameters one can see in Figure 2-11 and Figure 2-12 the similar effect on the lens shape and port position as described by Hansen in [13]. The beam curve opens and the array curve closes with increased α. As expected, the focal points move outwards on the beam curve. Increased β shows a similar effect to an increased α, but with only a minimal change in the focal point position. Varying γ does not change the port curves. Instead increased γ moves the beam ports closer together, while the array ports are spread apart. The distance between the two port curves rises when the focal length f_1 is bigger. Since all equations are normalized to f_1, all spacings change when f_1 / λ is changed.

The focal length of the lenses in Figure 2-11 and Figure 2-12 and all other parameters have the same values as the one of the conventional Rotman lens. Therefore, the port curves of the conventional Rotman lenses and the new lenses can be compared. A second material in the lens has only a small influence on the beam port curve. The important changes are on the array port curve. The diffraction brings the array ports closer together and the effects of the different parameters on the array port curve is considerable smaller compared to the conventional Rotman lens (Figure 2-3 - Figure 2-4).

2.3.3 Phase-error analysis, optimization, and miniaturization of Rotman lens with split substrate

In the design approach described above, the array ports are calculated according to the focal points. For all other points, the path-length equality equations are not fulfilled. Therefore, there is a phase error at the antenna elements, which reduces the scanning ability of the antenna array. To visualize these path-length errors the optimum beam port position corresponding to each array port is calculated for all scan angles. This is shown in Figure 2-13. The larger the spreading of these optimal port positions, the larger is the phase error.

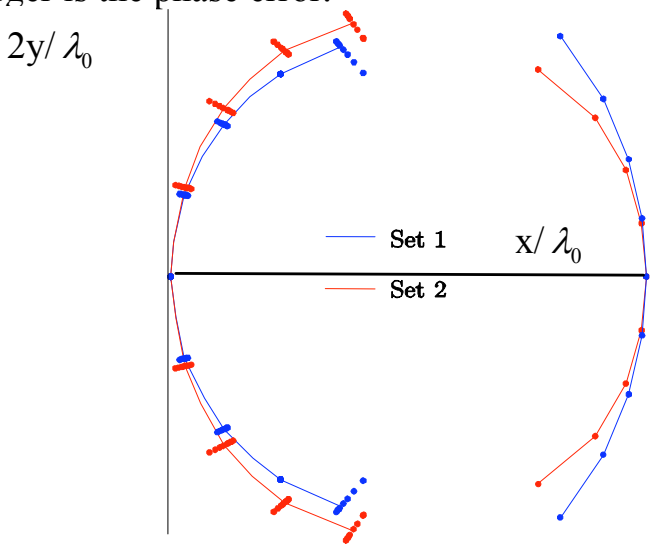

Figure 2-13 Beam port spreading of the new Rotman lens design for different parameter sets

The sets in Figure 2-13 have scan angles $\phi = \pm 10, 20, 30, 40$ degrees. For set 1, the focal point is placed on the beam port position of scan angle 30 degrees, such that this port shows no spreading, whereas the outer most beam port shows a wide spreading of the optimal port position. For set 2, the focal point is placed at $\alpha = 35$. For this set, all ports but the central beam port show spreading. The mean spreading is wider but the maximal spreading is smaller.

Since the new lens design with two different dielectric constants has the advantage of better focusing on the array ports, it is possible to design a lens with a small array port curve. Therefore, in this second design procedure, the phase error leads to different array ports when optimized for a given beam port curve. Figure 2-14 shows the spreading of the optimal array port position for different parameter sets.

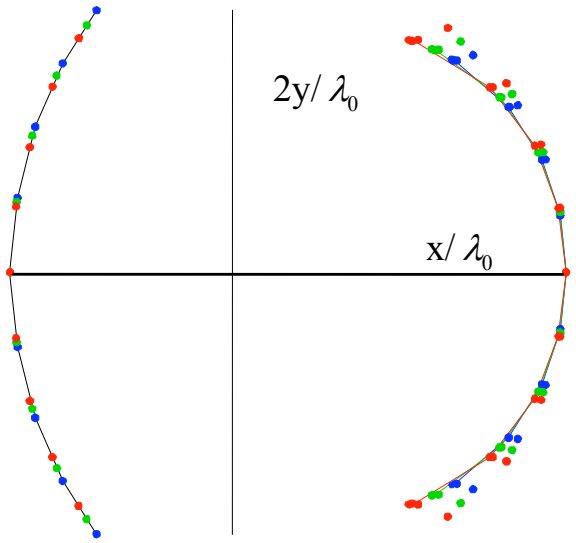

Figure 2-14 Array port spreading for a lens with all beam ports as focal points

It is obvious that the larger the array arc the larger the spreading, and therefore the larger the phase error. For the parameter sets used in Figure 2-14, only the parameter γ varies such that the beam port curve remains the same and only port positions change. The optimal array port curve is more or less the same for all parameters. Nevertheless, the spreading increases when the ports drift apart on the array port curve.

In order to optimize the lens, i.e. the port contours and the port positions, one has to consider the overall influence on the lens performance. Therefore, the design of a Rotman lens must involve all part of the lens. It is not possible to minimize the path-length errors trough the lens, which is equivalent to minimizing the phase errors, without keeping in mind that also the amount of reflections at the material interface is strongly dependent on the lens design, especially on the maximal angle of incidence. The balance between the phase

error and magnitude of reflections is only one trade-off when designing the Rotman lens on a non-uniform substrate.
The pattern of a linear antenna array qualifies to quantify the influence of the phase error. The array factor is evaluated for the array with uniformly fed isotropic radiators employed as the radiating elements. The phase distribution from the analytical lens design is inserted into the array factor calculation.
Different distributions of the phase error were noted for different design parameter variations. If the phase error distribution over the array elements is relatively symmetrical with respect to the center element, the side lobe level will rise with the magnitude of the phase error. For an asymmetric distribution, the side lobe level rises only on one side. Additionally in this case the scanning direction of the main lobe is shifted. This shift is proportional to the magnitude of the phase error.
The corresponding phase error is calculated from the port positions for a test lens. The resulting array factor including the phase error is plotted in Figure 2-15. The orthogonal beam distribution and the constant side lob level prove that it is possible to design a lens with two different substrates that has negligible phase errors and achieves good scanning properties. To investigate the phase errors that originate within the lens due to additional wave reflections, the synthesized lens design is simulated later with a full wave electromagnetic field solver. The results are discussed later in chapter 3.

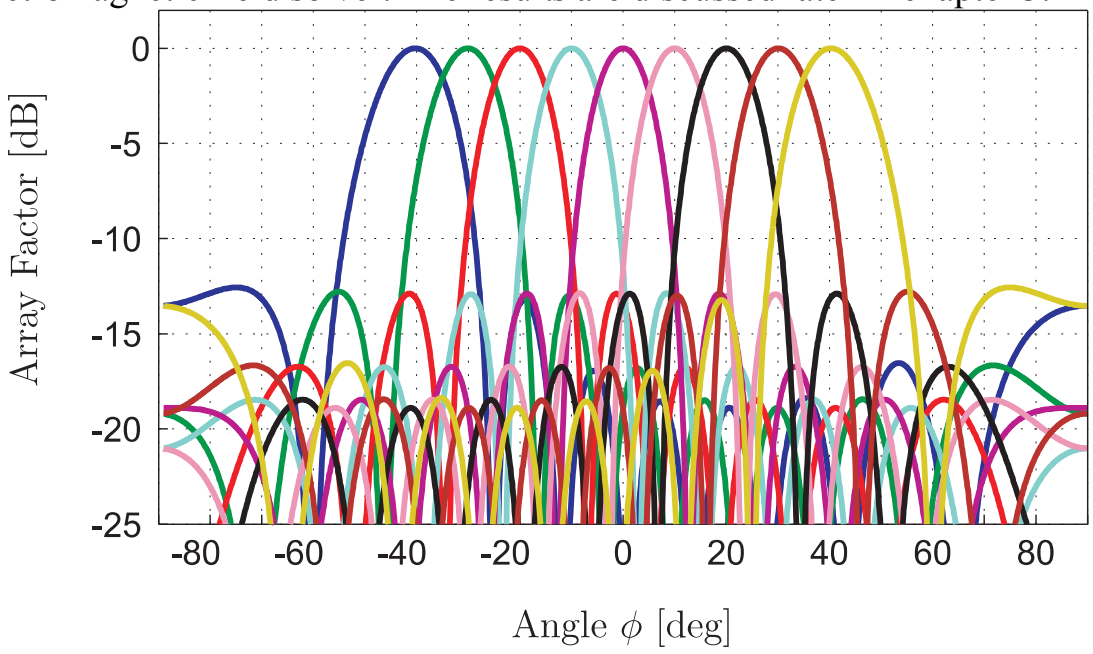

Figure 2-15 Normalized array factor including the calculated phase error

2.3.4 Relationship between lens size and phase error for conventional and split-substrate Rotman lenses

An automatic search routine for the optimal lens design has been implemented. The design parameters --namely frequency, focal length, material parameters, and element spacing of the antenna array -- are kept constant for all lenses, while the remaining lens parameters are subject to optimization. For each beam port, the root-mean-squared path-length error (PLE_{rms}) to all array ports is calculated. Then the lens with the smallest mean PLE_{rms} over all beam ports is chosen as the optimum design.

To exclude mathematical results that correspond to non-physical results or to lens forms that cannot be realized, several constraints have to be imposed on the lens form. Firstly, there has to be a minimal spacing between the port curves for otherwise it is not possible to place a port at the outermost port position. Secondly, the ports of the new design need to have a minimal distance to the material interface to avoid undesired reflections. Thirdly, both port curves should be of similar height. The smaller one should be at least 85% of the larger one according to Hansen [13]. Finally, all ports have to be inside the opening of the opposite curve. Lenses that break one or more of these rules are discarded in the optimization.

This automation routine with the above-mentioned constraints is applied to the design equations for conventional Rotman lenses as well as the new design procedure for a lens on two substrates. All lenses were designed for a frequency of 10 GHz and use substrates with a uniform relative dielectric constant of 6, respectively 10 and 6. For both lens types, three different designs are investigated to examine the relation between the focal length and mean the PLE_{rms}. The first design has nine array ports and nine beam ports for scan angles $\phi = \pm 40,30,20,10$ and 0 degree. The second design uses also nine array ports, but only seven beam ports with a maximal scan angle of 30 degrees. For the third design, the number of array ports is reduced to seven, the maximal scan angle is 30 degrees. The results in terms of PLE_{rms} are shown in Figure 2-16. The results for lenses according to Hansen are plotted with dashed lines, while the results for the lenses on two different substrates are plotted with solid lines.

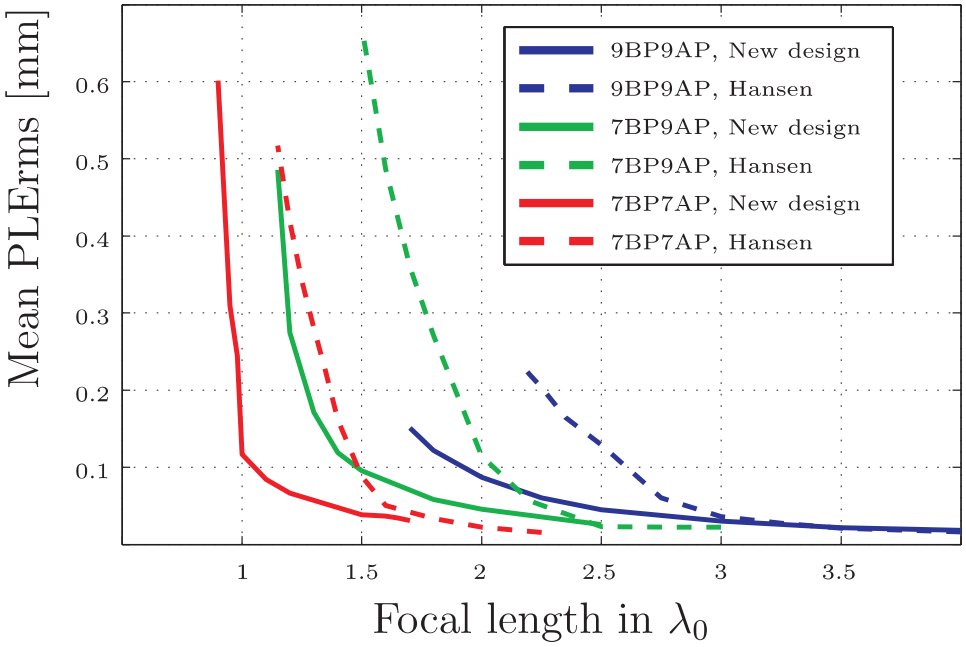

Figure 2-16 Mean PLE $_{rms}$, plotted over focal length

In Figure 2-16 one can see that it is possible to reduce the focal length of the lens for a given mean PLE $_{rms}$ by introducing a non-uniform substrate, even though about half of the lens is on a substrate with a smaller dielectric constant. With a second substrate, it is possible to design smaller lenses than on a single substrate with the same number of ports and identical scan angles. The second substrate makes it possible to design a lens with smaller PLE $_{rms}$ for a given focal length.

Amplitude errors on the antenna elements cannot be quantified analytically and result from multi-path propagation due to reflections inside the lens. Full-wave simulation showed that the reflections at the boundary between the different substrates increase with the angle of incidence or the ratio of the relative dielectric constants of the two adjacent media. A reduction of the reflections can be achieved by increasing the number of dielectrics used. The next section briefly introduces the analytical derivation for a three dielectric Rotman lens

2.3.5 Design of lens with three substrate segments

An additional region with a third dielectric constant ε_{r3} is accounted for in the analytical derivation. The geometry of such a lens having two substrate interfaces at $x = -R_1$ and $x = -R_2$ is shown in Figure 2-17

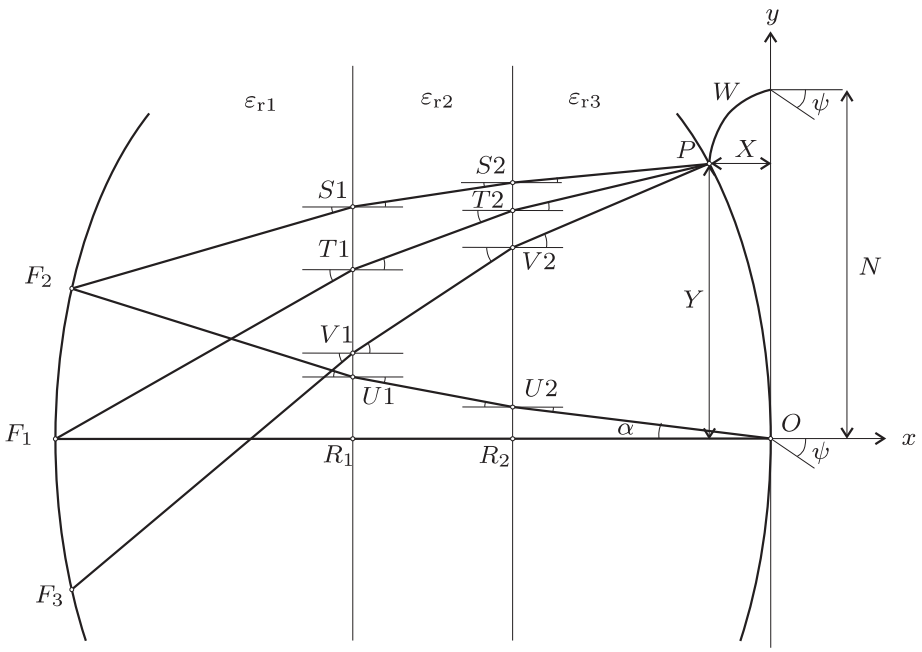

Figure 2-17 Lens parameters for the Rotman lens with three different substrates

For Rotman lenses with three different substrates, the path-length equality equations becomes

$$\begin{aligned}&\overrightarrow{F_1T_1}\sqrt{\varepsilon_{r1}} + \overrightarrow{T_1T_2}\sqrt{\varepsilon_{r2}} + \overrightarrow{T_2P}\sqrt{\varepsilon_{r3}} + W\sqrt{\varepsilon_{r3}} = \\ &\overrightarrow{F_1R_1}\sqrt{\varepsilon_{r1}} + \overrightarrow{R_1R_2}\sqrt{\varepsilon_{r2}} + \overrightarrow{R_2O}\sqrt{\varepsilon_{r3}} + W_0\sqrt{\varepsilon_{r2}}\end{aligned} \tag{2.47}$$

$$\begin{aligned}&\overrightarrow{F_2S_1}\sqrt{\varepsilon_{r1}} + \overrightarrow{S_1S_2}\sqrt{\varepsilon_{r2}} + \overrightarrow{S_2P}\sqrt{\varepsilon_{r3}} + W\sqrt{\varepsilon_{r3}} + N\sin\psi = \\ &\overrightarrow{F_2U_1}\sqrt{\varepsilon_{r1}} + \overrightarrow{U_1U_2}\sqrt{\varepsilon_{r2}} + \overrightarrow{U_2O}\sqrt{\varepsilon_{r3}} + W_0\sqrt{\varepsilon_{r3}}\end{aligned} \tag{2.48}$$

$$\overrightarrow{F_3V_1}\sqrt{\varepsilon_{r1}}+\overrightarrow{V_1V_2}\sqrt{\varepsilon_{r2}}+\overrightarrow{V_2P}\sqrt{\varepsilon_{r3}}+W\sqrt{\varepsilon_{r3}}-N\sin\psi = \overrightarrow{F_2U_1}\sqrt{\varepsilon_{r1}}+\overrightarrow{U_1U_2}\sqrt{\varepsilon_{r2}}+\overrightarrow{U_2O}\sqrt{\varepsilon_{r3}}+W_0\sqrt{\varepsilon_{r3}} \quad (2.49)$$

Again, the symmetry of the focal points F_2 and F_3 was used in equation (2.49).

Array-port contour calculation

Similarly to the previous section, β is adapted, considering the different propagation velocities in the three regions of the non-uniform substrate. Thus, β becomes

$$\beta=\frac{\overrightarrow{F_2U_1}\sqrt{\varepsilon_{r1}}+\overrightarrow{U_1U_2}\sqrt{\varepsilon_{r2}}+\overrightarrow{U_2O}\sqrt{\varepsilon_{r3}}}{\overrightarrow{F_1R_1}\sqrt{\varepsilon_{r1}}+\overrightarrow{R_1R_2}\sqrt{\varepsilon_{r2}}+\overrightarrow{R_2O}\sqrt{\varepsilon_{r3}}} \quad (2.50)$$

Using Snell's law and the following relations

$$\overrightarrow{U_2O}=\frac{R_2}{\cos\alpha} \quad e_2=\sqrt{\frac{\varepsilon_{r3}}{\varepsilon_{r2}}} \quad \sin\theta_{iU_2}=e_2\sin\alpha$$

$$\overrightarrow{U_1U_2}=\frac{R_1-R_2}{\cos\theta_{iU2}} \quad e_1=\sqrt{\frac{\varepsilon_{r2}}{\varepsilon_{r1}}} \quad \sin\theta_{iU_1}=e_1\sin\theta_{iU_2}$$

$$\overrightarrow{F_2U_1}=\frac{\beta\left(\overrightarrow{F_1R_1}\sqrt{\varepsilon_{r1}}+\overrightarrow{R_1R_2}\sqrt{\varepsilon_{r2}}+\overrightarrow{R_2O}\sqrt{\varepsilon_{r3}}\right)-\left(\overrightarrow{U_1U_2}\sqrt{\varepsilon_{r2}}+\overrightarrow{U_2O}\sqrt{\varepsilon_{r3}}\right)}{\sqrt{\varepsilon_{r1}}}$$

the position of the off-axis focal point F_2 can be written as

$$\begin{aligned} F_{2x} &= R_1+\overrightarrow{F_2U_1}\cos\theta_{iU_1} \\ F_{2y} &= R_2\tan\alpha+(R_1-R_2)\tan\theta_{iU_2}+\overrightarrow{F_2U_1}\sin\theta_{iU_1} \end{aligned} \quad (2.51)$$

The position of the focal point F_3 is derived through symmetry. At this point the array port positions $P=(-X,Y)$ and the corresponding electrical length

W to connect the array ports with the antenna elements can be calculated by solving (2.47)-(2.49).

Beam-port contour calculation

Similarly, to the lens on two different substrates, the beam port positions for a lens on three different substrates are calculated by minimizing the sum over the quadratic path-length error to all array ports. The path-length error can be written as

$$\Delta L = \overrightarrow{F_\phi S_1}\sqrt{\varepsilon_{r1}} + \overrightarrow{S_1 S_2}\sqrt{\varepsilon_{r2}} + (\overrightarrow{S_2 P} + \widetilde{W})\sqrt{\varepsilon_{r3}} + N\sin\phi - \overrightarrow{F_\phi U_1}\sqrt{\varepsilon_{r1}} - \overrightarrow{U_1 U_2}\sqrt{\varepsilon_{r2}} - \overrightarrow{U_2 O}\sqrt{\varepsilon_{r2}} \tag{2.52}$$

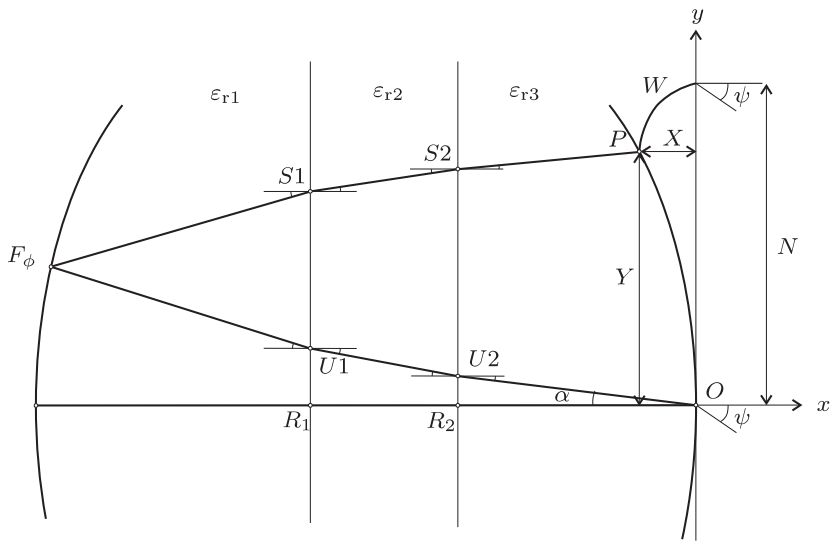

Figure 2-18 Lens parameters for the beam port calculation for the design with three substrate segments

Finally, the beam port position F_ϕ corresponding to a scan angle ϕ is given by (2.53).

$$F_\phi = argmin_{F_\phi}\sum_{k=1}^{NE}\Big[\overrightarrow{F_\phi S_1}_k\sqrt{\varepsilon_{r1}} + \overrightarrow{S_1 S_2}_k\sqrt{\varepsilon_{r2}} + (\overrightarrow{S_2 P}_k + \widetilde{W}_k)\sqrt{\varepsilon_{r3}} + N_k\sin\phi - \overrightarrow{F_\phi U_1}\sqrt{\varepsilon_{r1}} - \overrightarrow{U_1 U_2}\sqrt{\varepsilon_{r2}} - \overrightarrow{U_2 O}\sqrt{\varepsilon_{r3}}\Big]^2 \tag{2.53}$$

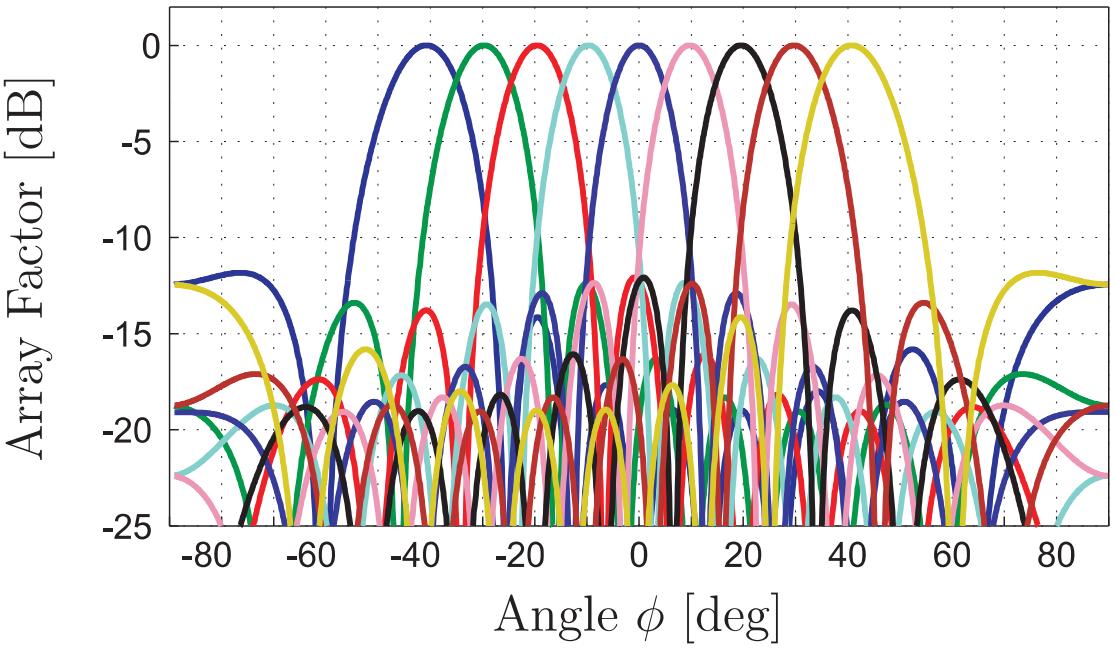

Figure 2-19 Normalized array factor for an antenna array including the phase error calculated from a lens design with three substrates.

The beam port curve is found by solving this equation for all desired scan angles. This completes the design procedure for the Rotman lens with three different substrates.
From the path-length, error given in equation (2.52), the phase errors for each beam port to all array ports can be calculated. The array factor for a linear antenna array including the calculated phase errors is calculated and plotted in Figure 2-19.

Chapter 3

Results of non-uniform dielectric lenses

Abstract - The theory of non-uniform dielectric lenses introduced in Chapter2 is used to design lenses of different sizes on split-dielectric substrate. Focusing and reflections due to the non-uniform substrate will be investigated on a lens with a large focal length. Larger lenses allow better visualization of the specific effects. Subsequently a smaller lens is realized and measured to prove that the size reduction is possible with the new split-dielectric approach.

3.1 Introduction

The focusing effect of the new Rotman lens is the most important feature of the new lens type and will be investigated first. This is done by comparing two similar lenses, one realized on a single and the other on a split substrate. The analysis shows the transmitted power to the different ports, and qualitative based on the current distributions along the two lenses. The two lenses are chosen to have equal focal lengths and equal numbers of ports. In the second part of this chapter, the substrate splitting is taken a step further by replacing the two zone dielectric lens by a triple zone dielectric lens. Improved focusing and reduced reflections at the dielectric boundaries are demonstrated. The last part of the chapter exemplifies the miniaturization of the Rotman lens with a dual dielectric lens. Using a conventional single dielectric substrate such miniaturization would not be possible.

3.2 Design and realization of a dual dielectric lens

Within the constraints of availably, two substrates with dielectric constants of 3 and 6 are chosen for the split-dielectric lens. For the uniform lens, the higher dielectrical constant is used. Both substrates have a thickness of 10mil. The design frequency is set to 10GHz. For a better observation of the refraction, both lenses are relatively large with a focal length $f_1 = 3.5\lambda_0$. Each lens has nine beam ports, corresponding to the scan angles $\phi = \pm 40,30,20,10$ and 0 degree and nine array ports. To avoid reflections, seven dummy ports are placed on each side. All ports have a triangular shape with an opening angle of $30°$.
The remaining design parameters are β, γ and R_1 as defined in Figure 2-9. The parameter values are $\beta = 1$, $\gamma = 1.7$ and $R_1 = 0.7 f_1$. All beam ports are made to coincide with the focal points, as described in the previous sections. The mean quadratic path-length error (PLE_{rms}) to all array ports is calculated for each beam port. Then the lens with the minimum mean PLE_{rms} over all beam ports is chosen among the lenses that fulfill the geometrical constraints.

Based on the given parameters, the Rotman lens is synthesized using the optical ray-tracing algorithm described in the previous section. The algorithm is programmed in *MATLAB*. Due to the complexity of the synthesized structure, an automatic *MATLAB* routine is made to generate its proper full-wave model. This resulting structure is analyzed by means of *HFSS* [27]. In the design of Rotman lenses, the full-wave simulation has the same importance as the underlying mathematical equations for a functional result. Only a full-electromagnetic simulation can characterize the standing and the propagation of the wave with all the necessary details. As a result of the simulation, the current and field distribution along the lens is obtained. All other parameters of interest, such as standing waves, aperture illuminations, matching of ports and lens can be extracted from the current distribution.

Therefore, a good way to investigate focusing and reflections is to plot the magnitude of the surface current of the lens. Figure 3-1 shows the current plots of the single and split-dielectric lenses with the central beam port active. The focusing can be discussed best by comparing the two current distributions. In the split-dielectric lens, the wave opens strongly until it

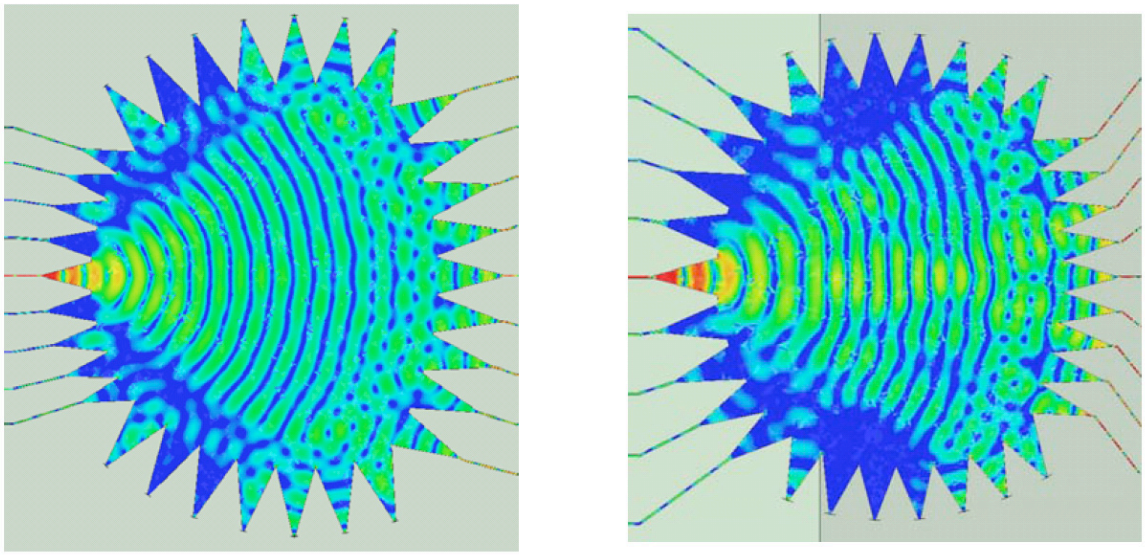

Figure 3-1 Snapshot of the current magnitude distribution of a single- and a split-dielectric lens, with excitation applied at the central beam port

intercepts the interface of the dielectrics. From that point on, it can be seen that the angle reduces. The same effect can also be seen when looking at the current distribution at the dummy ports placed at the lateral lens sides. The dummy ports can be distinguished from beam and array ports, by not having a microstrip line to guide the signal to the board edge. The microstrip lines are omitted in order to minimize the already demanding computational requirements for the simulation. The dummy ports are closed with lumped ports that provide the same effect as microstrip terminated ports.

The dummy ports of the first lens absorb more power than those of the split-dielectric lens. An interesting fact is that the first dummy port viewed from the beam-port side absorbs more power in the split-dielectric case than in the uniform case. At this point, the dielectric step provides a reflection strong enough to be seen as an increase in absorption in that port. It is expected that with a larger incident angle the reflection should increase. This effect should be seen more clearly when the lens is fed at the outermost beam ports.
Indeed, the outermost beam ports exhibit the strongest reflections due to the largest angle of incidence on the material interface. In Figure 3-2 one can see that reflections are not only caused by the material interface, but also occur at the array ports and the lens outline. This increased reflection results from the port geometry as seen by the incident wave. The different angles of incidence

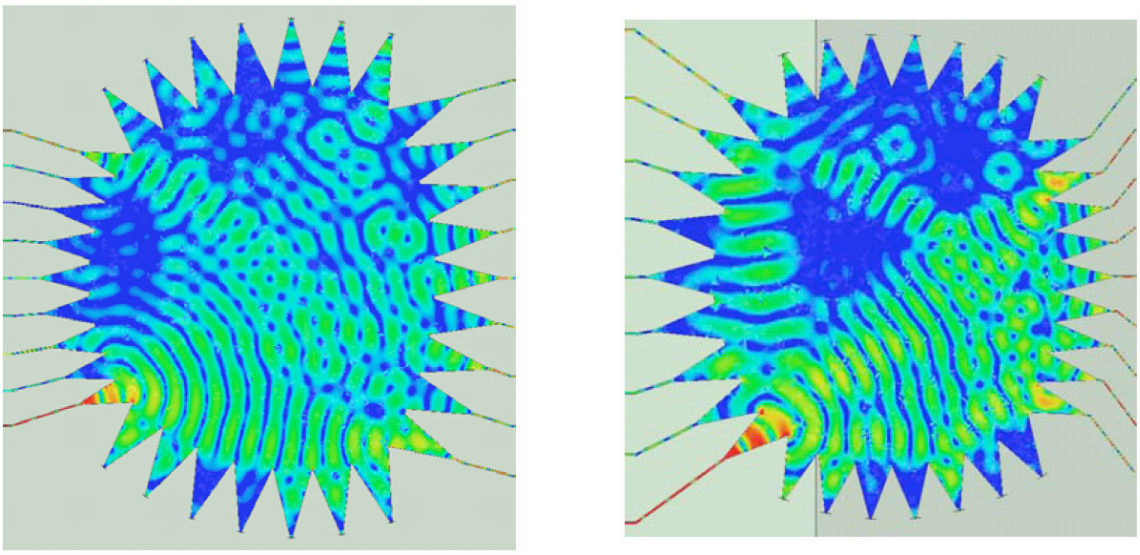

Figure 3-2 Current distribution of a single- and a split-dielectric lens, with the excitation applied at the outermost beam port

provide a different structure and lead to different reflections. Increasing the lens size and reducing the port openings would reduce this effect.
In order to examine the fraction of the transmitted power that is reflected at the substrate interface, the transmission parameters are calculated for groups of ports. Figure 3-3 and Figure 3-4 show the power flow in the single dielectric and split-dielectric lenses, respectively.

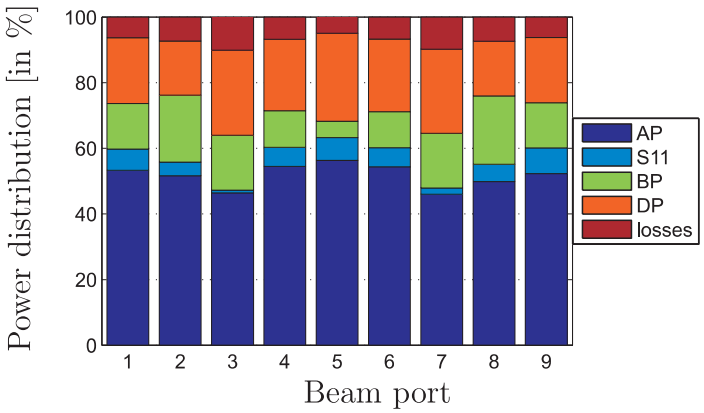

Figure 3-3 Power distribution over port groups for a single substrate lens. Array port(AP), Beam Port(BP), Dummy Port(DP), Input return loss(S11)

The total flow is separated into the power transmitted to the array ports (AP), the dummy ports (DP), and the beam ports (BP), the losses within the lens including radiation (losses), and the reflection (S11).
In the first part of the comparison, we focus on the potential for increasing the efficiency of the lens. The study in [26] claims that this increase in efficiency is the result of the focusing effect. The power absorbed in the dummy ports, especially for the outermost beam ports, indeed reduces as seen in Figure 3-4. The reduction comes mainly from the power reflecting back from the dielectric interface into the beam ports. The power transmitted to the array ports remains unchanged or is partly reduced.

This effect is stronger for the outer beam ports because they have larger angle of incidence with respect to the dielectric interface, yielding stronger reflections. Altogether, the power lost into the dummy ports is reduced; the downside, however, is the increased power reflected back into the beam ports. This investigation questions the generality of the claim in [26].
Lens efficiency needs to be treated differently from the focusing properties of the lens. Depending on the lens size and structure as well as the dielectric mismatch, the losses can even increase or lead to complete failure. The ultimate solution to reduce the lens size and maintain or even increase the efficiency can be realized by extending the two dielectric lenses to multiple dielectric ones. This way the power flow can be redirected from the beam ports to the array ports without increasing the reflection.

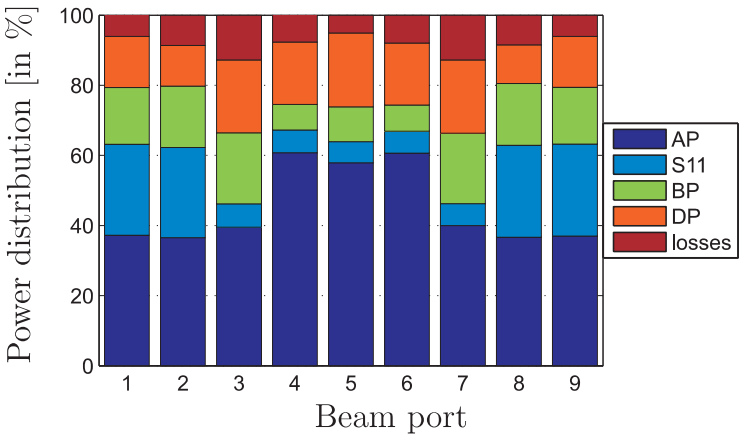

Figure 3-4 Power distribution over port groups for the lens on a split substrate Array port(AP), Beam Port(BP), Dummy Port(DP), Input return loss(S11)

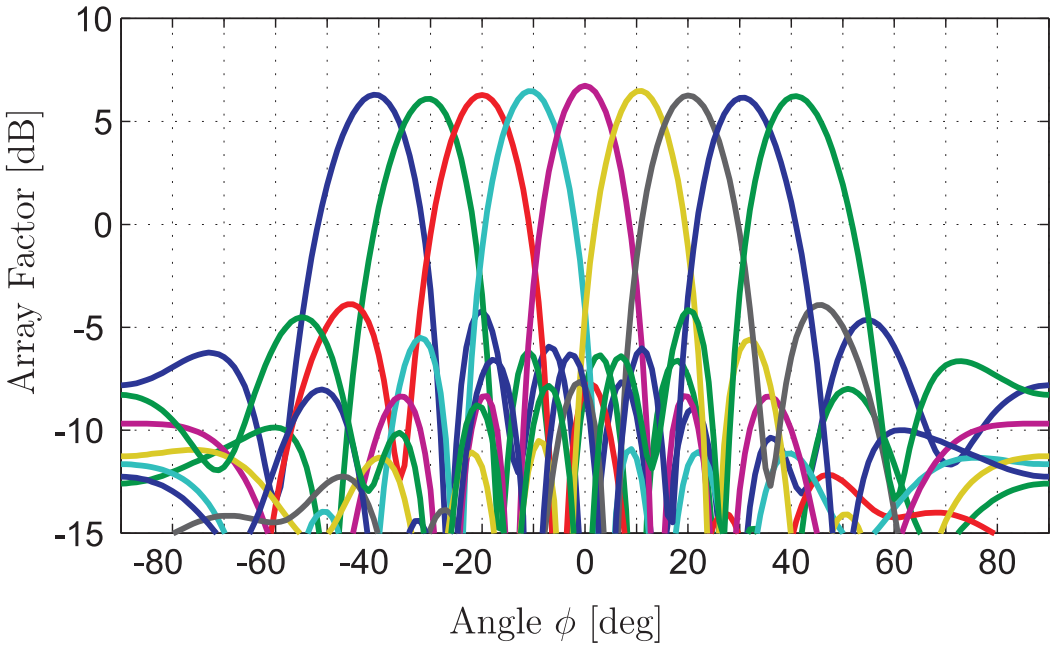

Figure 3-5 Array factor, calculated from simulated results

The current distribution is an early indicator of the lens performance. The array factor ultimately shows the beam-scanning ability of the lens. In Figure 3-5 the array factor is calculated from the amplitudes and phases of the S-parameters obtained from the full-wave simulation.

Beam port	Designed scan angle	Simulated results	Measured results
BP1	-40	-40.8	-43.2
BP2	-30	-30.4	-31.5
BP3	-20	-20.0	-20.1
BP4	-10	-10.6	-9.9
BP5	0	0	0
BP6	10	10.6	9.9
BP7	20	20.0	20.2
BP8	30	30.6	31.7
BP9	40	40.8	43.5

Table 3-1 Scan directions of the beam ports in degree

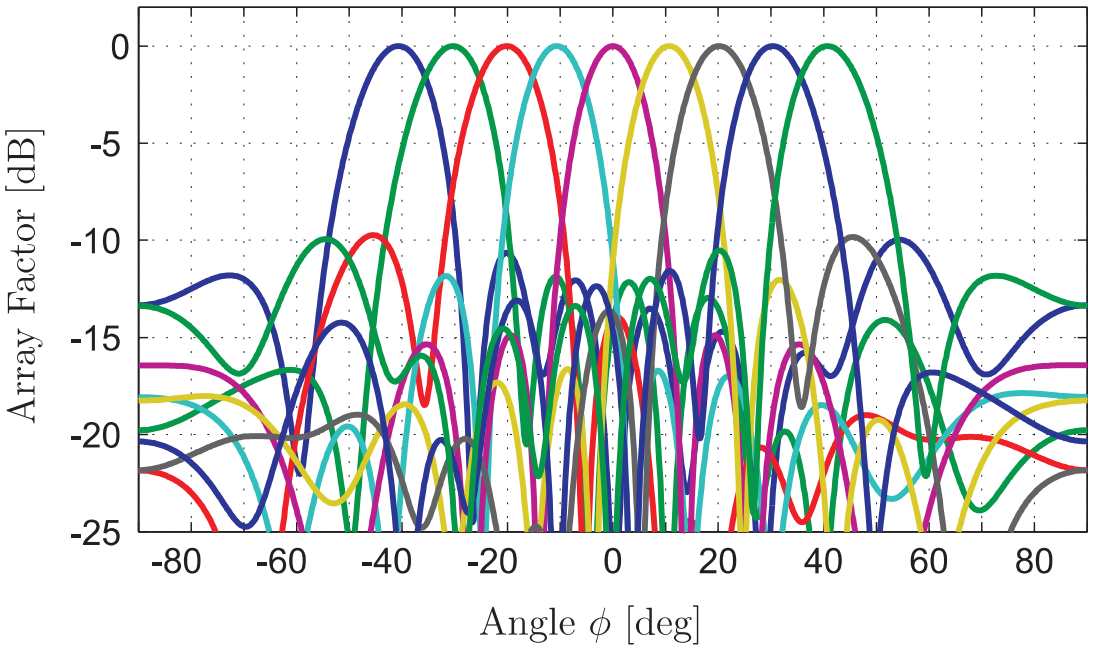

Figure 3-6 Normalized array factor, calculated from simulation results

First a calibration has to be carried out because the electrical lengths at the array ports in the designed and simulated lenses differ from the calculated value of $\widetilde{W}$. The result is a phase correction for each array port. This is done by assuming the central beam port to have the correct phase distribution. Any phase error of the central beam port feeding affects all other beam port extractions.
For a better overview, the designed, simulated and measured results for each beam port are listed in Table 3-1.

The normalized array factor in Figure 3-6 is more suitable to investigate the performance in terms of beam directions and the maximal side lobe levels (SLL). In order to see the difference between the full-wave and the synthesized results, the normalized array factors obtained using the two methods are plotted in Figure 3-7. As can be seen, the full-wave simulation and the synthesized results are in very good agreement. The largest shift in the main beam directions is 0.8 degrees. The maximal SLL of the synthesized lens is -12.8 dB, around 3.1 dB lower than the SLL of the simulated results. The difference in the SLL and the small shift of the beam directions are caused by the amplitude and phase errors inherent to the synthesized model. The uniform amplitude taper assumed in the synthesis is hard to achieve with equal port size. On the other hand, the equal size provides a constant phase

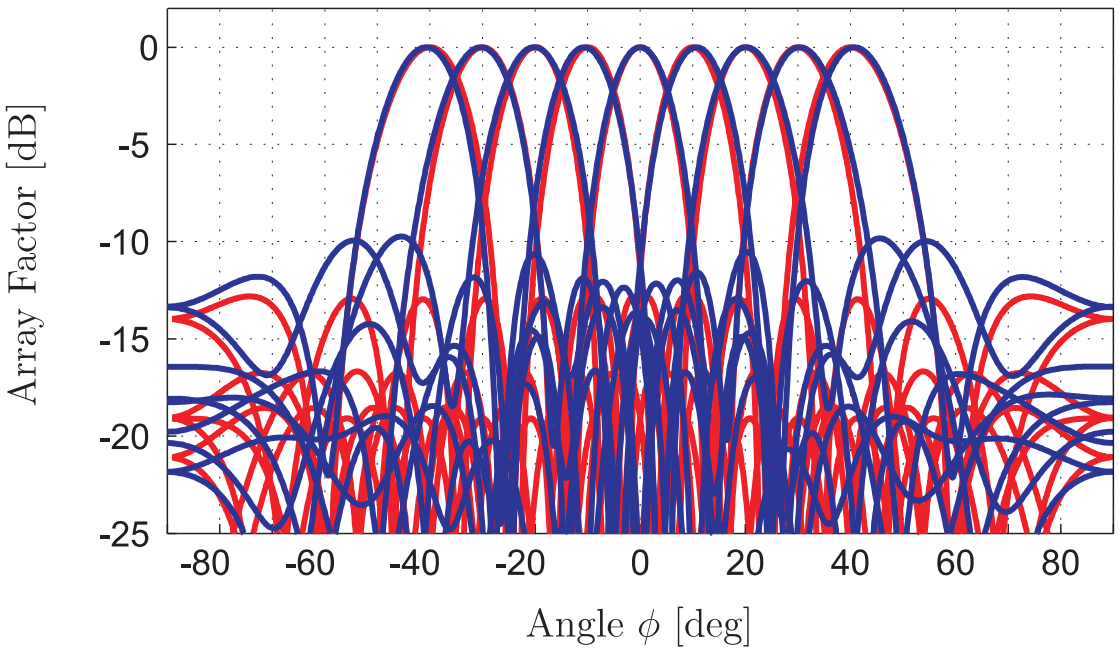

Figure 3-7 Normalized array factor, calculated from simulation results (blue) and from the synthesis (red)

error. The phase center of the port changes with the geometry and frequency and therefore cannot contact the lens at the very exact point of the array or beam port.
To achieve the uniform or any other amplitude taper, the array port sizes and illumination themselves have to be optimized. In this design, the focus was on the accuracy of the beam directions as a measure of the accuracy of the design methodology. Once the design methodology is validated, any split-dielectric lens can be improved in the same way as the conventional Rotman lens.

The designed split-dielectric lens was fabricated using two different substrates. Both substrates are glued to an aluminum plate. The electric connection between the two lens parts is provided by means of a narrow copper band. This band is strip coated with conductive adhesive to both sides of the lens halves. A picture of this lens is shown in Figure 3-8.

The array factor for each beam port is calculated from the magnitude and phase of the measured transmission parameter. It is plotted in Figure 3-9 together with the array factor from the simulation results. There are differences in the main lobe levels in the order of 2 dB. There are several causes for these differences, e.g. the additional losses of the substrate not

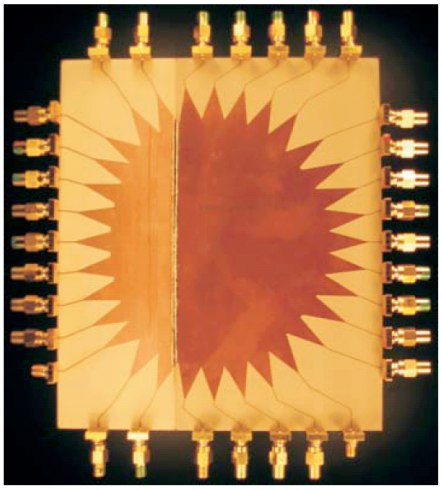

Figure 3-8 Picture of the manufactured split-dielectric Rotman lens

included in the simulation and, more importantly, the transition between the two lens parts. To fabricate such a lens with two different substrates with a seamless material interface is difficult. We have to assume that an air gap is created in-between the two different substrates. A simulation including a gap up to 300 μm shows changes of the main lobe levels encountered in the measurements.

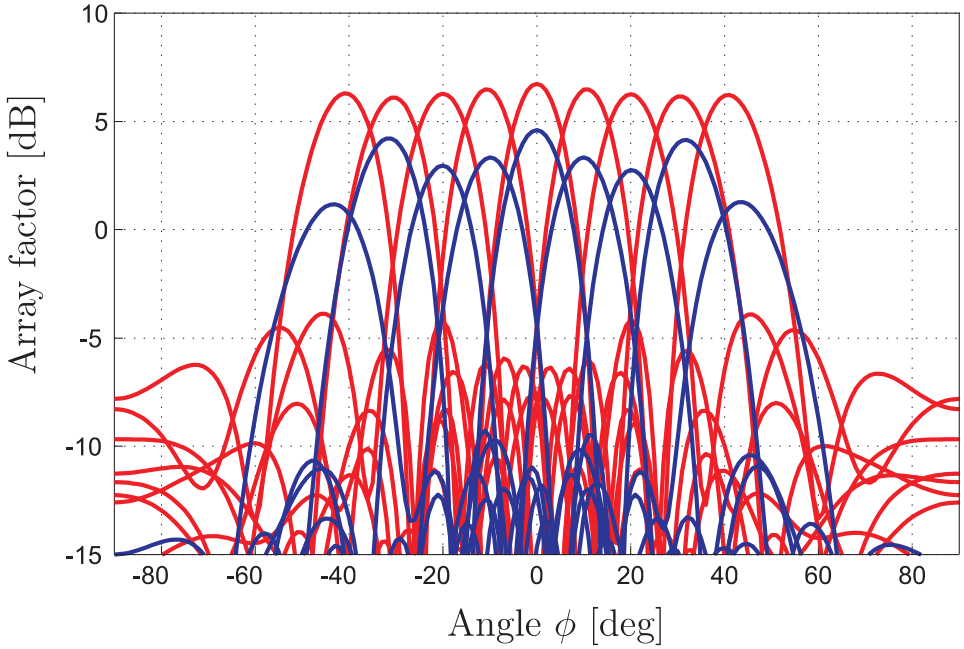

Figure 3-9 Array factor calculated from measurement results (blue) and simulation results (red).

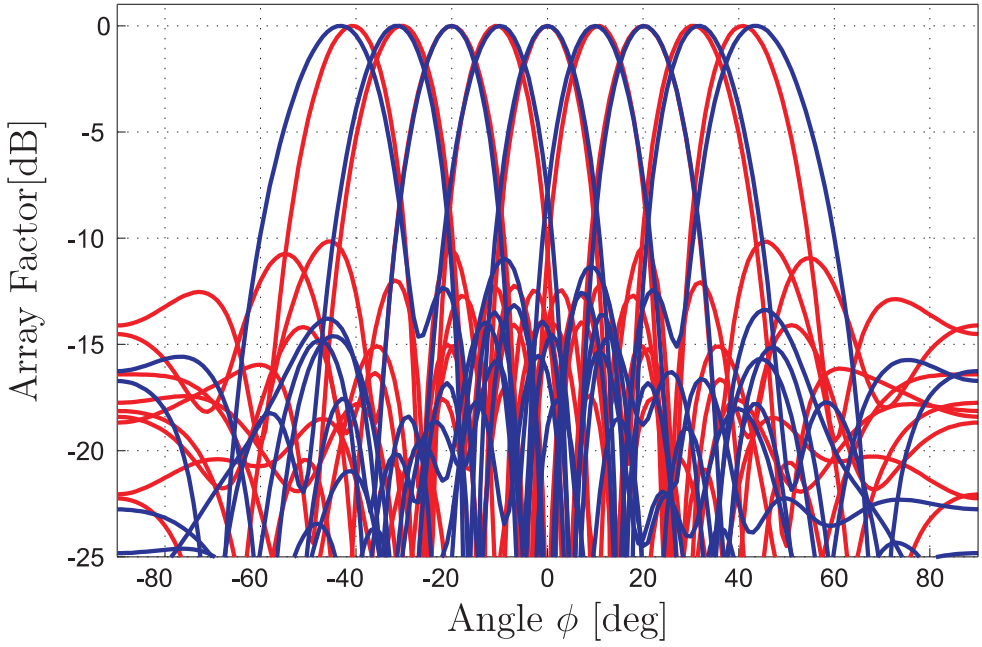

Figure 3-10 Normalized measured array factor at 8GHz-red line; 12GHz-blue line

The normalized array factors of the measurement at different frequencies are depicted in Figure 3-10. The maximum beam squint measured for the outermost patterns is four degree. By evaluating the array factor for different operating frequencies, an optimal frequency, i.e. the frequency where the main scanning directions coincide with the designed scan angles, can be found at 9.8 GHz. Reducing the operating frequency from 10 GHz to 9.8 GHz corrects the scanning directions, but also decreases the beamwidth. This is especially true for larger scan angles. For example, the -10 dB beamwidth for a scan angle of 40 degrees decreases from 29 to 26 degrees when the frequency is reduced from 10 to 9.8 GHz. The explanation for the small frequency shift is a small change of the dielectrical constant of the substrates used as well as the influence of the air gap and the longer current patch due to the artificial interconnect of the two lens parts.

To visualize frequency dependence of the scanning properties the array factor is shown in Figure 3-11 for frequencies from 8 to 12GHz. In subplot *c* of Figure 3-11, one can see that at 9.8GHz the variation of the main lobe level across the beam ports is the smallest. The difference between a scan angle of zero and a scan angle of 40 degrees is 1.7dB at 9.8GHz, and 3.4dB at 10GHz. Over this frequency range of 4GHz, the maximal SLL is not larger than -8dB. The -10dB beamwidth of the central beam changes in a small range between

19 and 22 degrees and increases at the maximal scan angle from 24 to 45 degrees.

Figure 3-12 shows the power distribution from each beam port to the array ports, dummy ports, beam ports as well as losses in the lens obtained from the measurements.

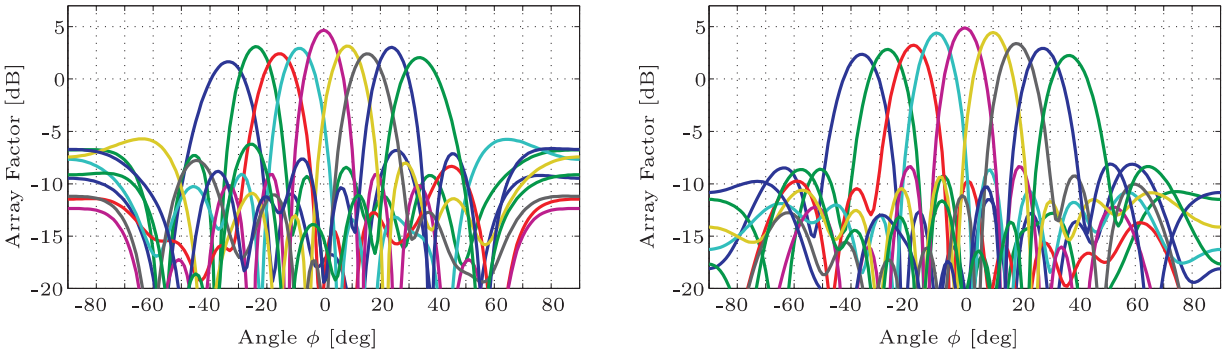

(a) Array factor at 8 GHz

(b) Array factor at 9 GHz

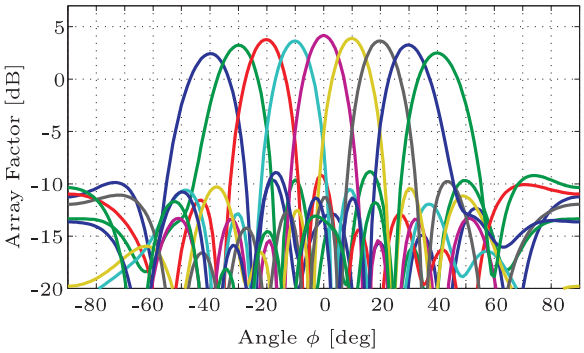

(c) Array factor at 9.8 GHz

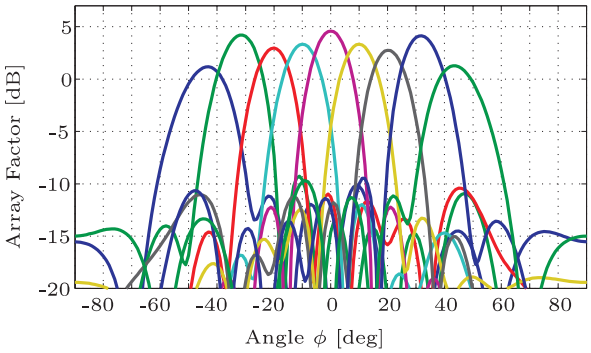

(d) Array factor at 10 GHz

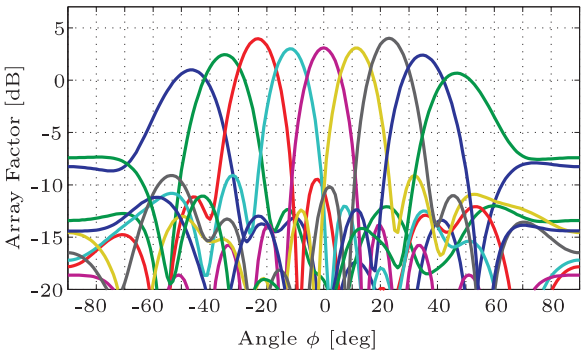

(e) Array factor at 11 GHz

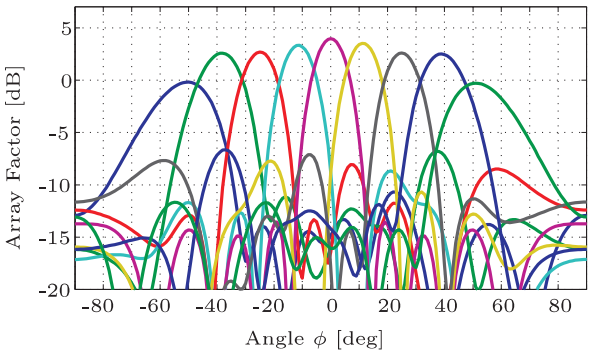

(f) Array factor at 12 GHz

Figure 3-11 Measured array factor at different frequencies of the split-dielectric lens

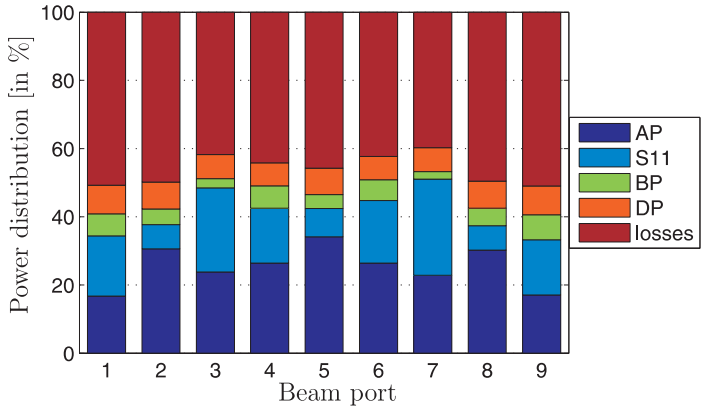

Figure 3-12 Power distribution over port groups for the measured split-dielectric lens

Due to the large dimensions of the lens, the power at the array port side is reduced to half of the inputted power because of the additional losses. This again highlights the importance of focusing the remaining power on the array ports and reducing the power transmitted to the dummy ports.

As has been shown, the full-wave simulation yields a very good approximation of the real measured structure. For this reason, the extension to a three dielectric lens will be verified only in terms of the full-wave simulation results.

3.3 Simulation of a triple dielectric lens

Triple dielectric lens are expected to improve the focusing and reduce the overall reflections at the dielectric regions interfaces. If this assumption is fulfilled an additional extensions of the known design will been achieved.
The triple dielectric lens design selected is similar to the previous uniform and dual dielectric lens. It has nine array ports and nine beam ports with the scan angles $\phi = \pm 40,30,20,10$ and 0 degree. The dielectric constants are $\varepsilon_{r1} = 3$ at the beam port side, $\varepsilon_{r2} = 4.5$ in the middle, and $\varepsilon_{r3} = 6$ at the array port side. The focal length is $f_1 = 3.5\lambda_0$ and the material interfaces are placed at $R_1 = 0.7 f_1$ and $R_2 = 0.3 f_1$.

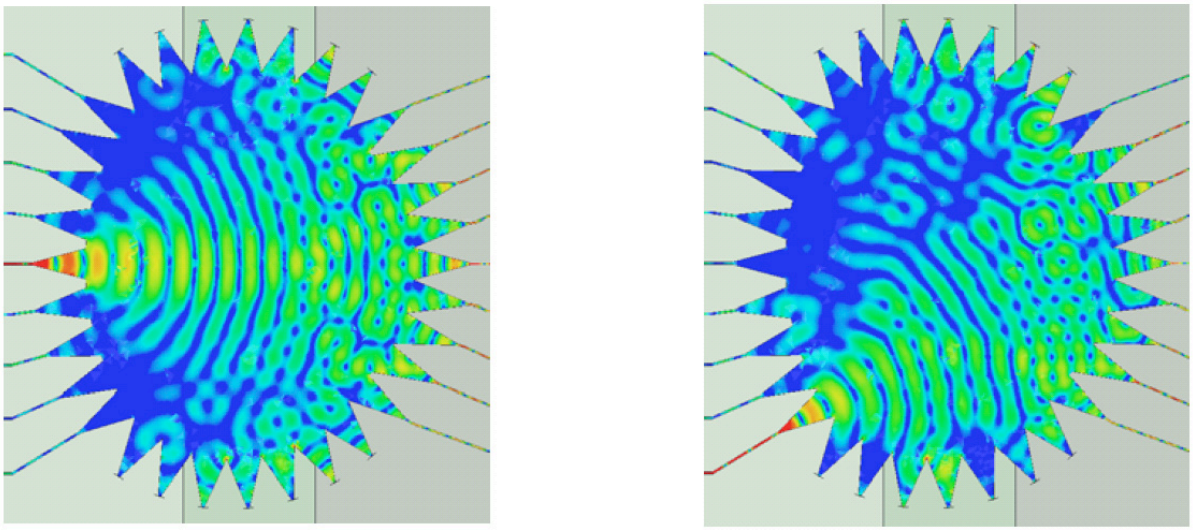

Figure 3-13 Current amplitude plot of a triple dielectric lens fed at the center and the outermost beam port

Following the same design procedure as for the lens with a dual substrate, the current distribution from the full-wave simulation is analyzed. The current plots in Figure 3-13 demonstrate that it is possible to design a lens with three different substrates that has less reflection back to the beam ports than a lens with two substrates. Additionally, the focusing on the array ports can be seen when comparing to the lens with uniform and dual dielectric substrates.

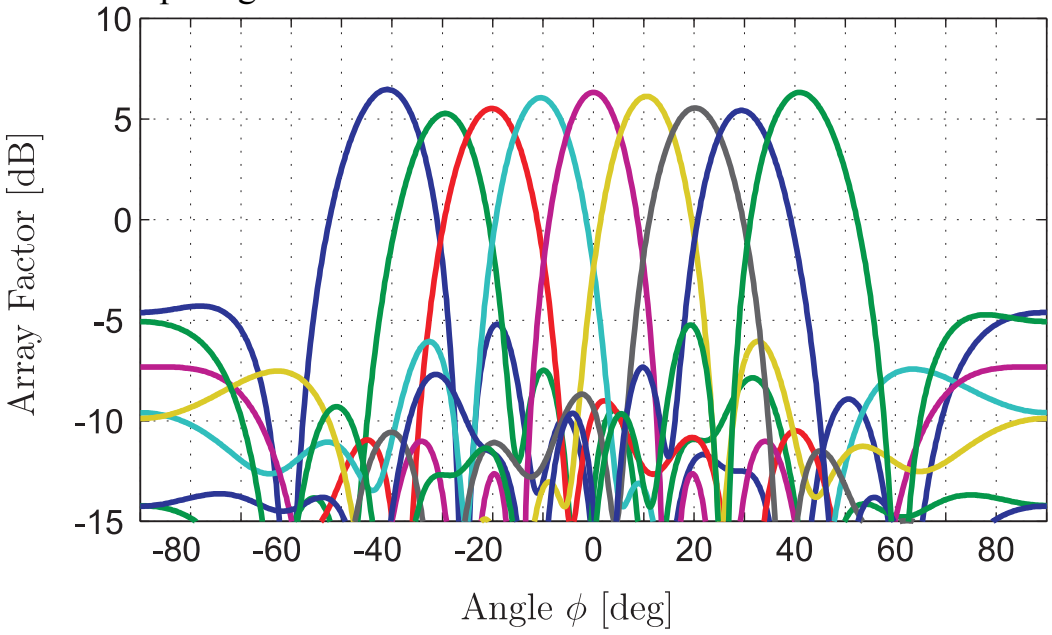

Figure 3-14 Array factor of simulated lens with three different substrates

Increased reflections between the array ports and the first dielectric step are noticed. This leads to the conclusion that the interface close to the array ports causes additional reflections and standing waves and has to be considered in the design of the triple dielectric lens.

Figure 3-14 shows that the gain of the different beam ports of the simulated triple substrate lens has the same distribution as for the lens on two substrates, except for the outermost beam port. Having the highest value implies that the illumination of the array port by the outermost beam port is stronger than in the conventional Rotman lens. Indeed the refraction proves to be an important design parameter. It allows us to illuminate the array ports more efficiently than in the case of the uniform lens.
The Figure 3-15 compares the normalized array factor from the simulation results with the calculated one based on the path-length error. The good agreement can be observed, especially for the beam directions and beam width. This confirms that the design methodology derived for a triple substrate Rotman lens. A fast way of synthesizing this new lens is achieved and additional design freedom is introduced.

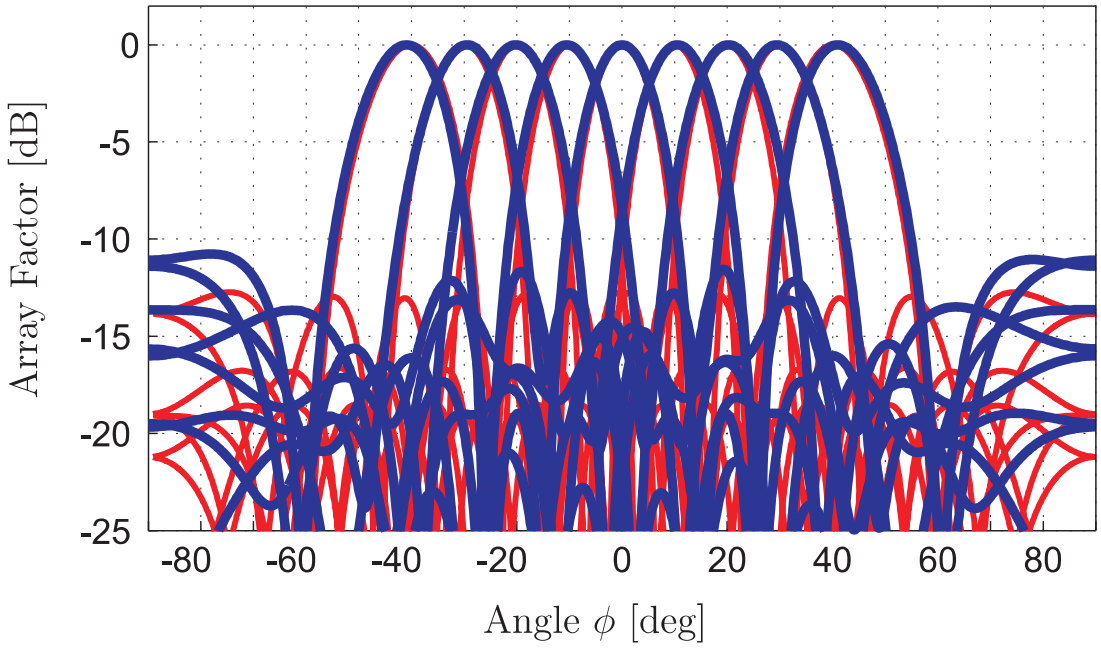

Figure 3-15 Normalized array factor of the simulation (blue) and from the synthesis (red)

Secondly, the maximal SLL of -11dB in the dual dielectric lens corresponds to a more uniform illumination of the array ports and less reflections within of the lens.

3.4 Design and realization of a very small Rotman lens using a dual dielectric substrate

The non-uniform substrate is a key change from the conventional Rotman lens. The split dielectric design increases the number of design parameter compared to the conventional one and therefore it extends the capabilities of the conventional Rotman lenses. The knowledge acquired from the dual and the triple substrate lens is now applied to reduce the size of the Rotman lens beyond what is possible by the conventional approach. Therefore, a small lens is designed and analyzed.

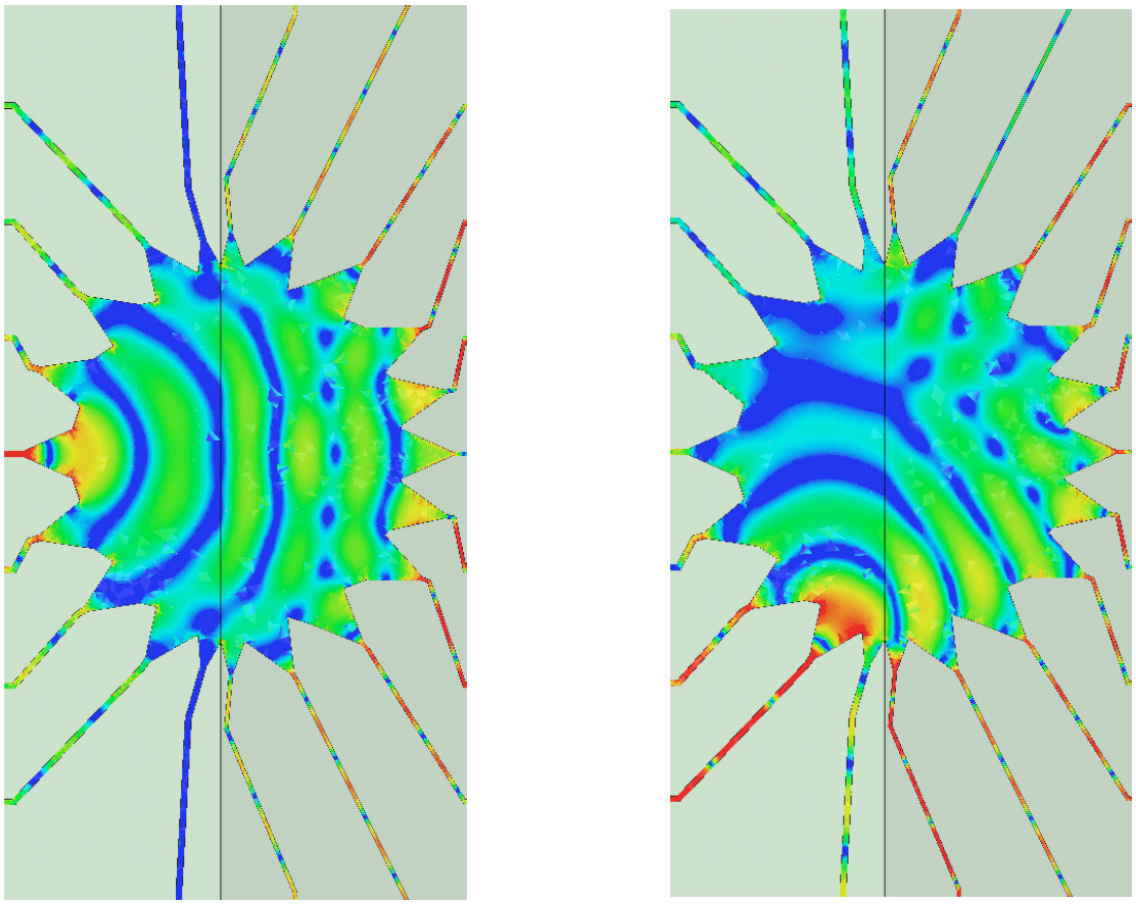

Figure 3-16 Computed current magnitude plot of a small split-dielectric lens, excited at the center and the outermost beam ports

The size of the lens was restricted to maximal 5cm, including the ports focal length and feed lines. This corresponds to a focal length of $f_1 = 1.2\lambda_0$ for an operating frequency of 10 GHz. As the large lens, the small lens also uses two substrates with dielectric constants of three and 6 and thickness 0.254mm. The operating frequency of the lens is again 10 GHz.

The mean PLE_{rms} over the beam ports is minimized by optimizing the remaining design parameters as described previously. The focal length is kept constant with $1.2\lambda_0$. The other design parameters are $\alpha = 26.24$ degrees, $\beta = 0.93$, $\gamma = 0.92$, $R_1 = 0.55 f_1$, $\phi = \pm 30,20,10$ and 7 beam ports and 9 array ports. The simulation results are presented in the following sections.

Figure 3-16 shows the current amplitude plots obtained when the central and the outermost ports are excited. Compared to the large lens the reflection partly increases, especially for the outer ports due to large angles of incidence. For smaller lenses, one can see that interactions of all the lens parts are much stronger, and as a result, the design is prone to many side effects.

The array factor, plotted in Figure 3-17, is used to examine the scan performance of the lens. It can be seen that the beam directions for the central beam port and the maximal scan angle are correct, but the other scan directions are shifted toward smaller angles.

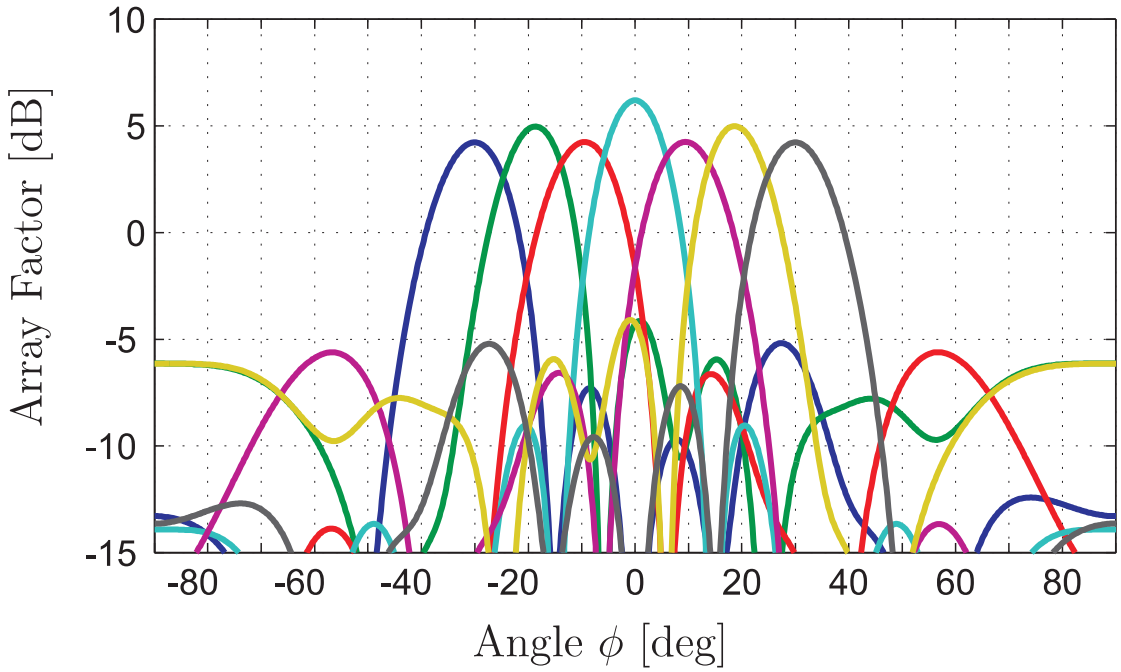

Figure 3-17 Array factor of the simulation results for a small split-dielectric lens

Beam port	Designed scan angle	Simulated scan angle	Measured scan angle
BP1	-30°	-30.0°	-31.0°
BP2	-20°	-18.6°	-19.1°
BP3	-10°	-9.4°	-9.9°
BP4	0°	0°	0°
BP5	10°	9.4°	9.5°
BP6	20°	18.6°	18.8°
BP7	30°	30.0°	32.0°

Table 3-2 Scan directions of the beam ports in degree

The strong coupling of different effects due to the small geometrical size makes it difficult to point out the cause for this beam shift towards smaller angles. The data of the beam directions from the synthesis, simulation, and measurements is given in Table 2.

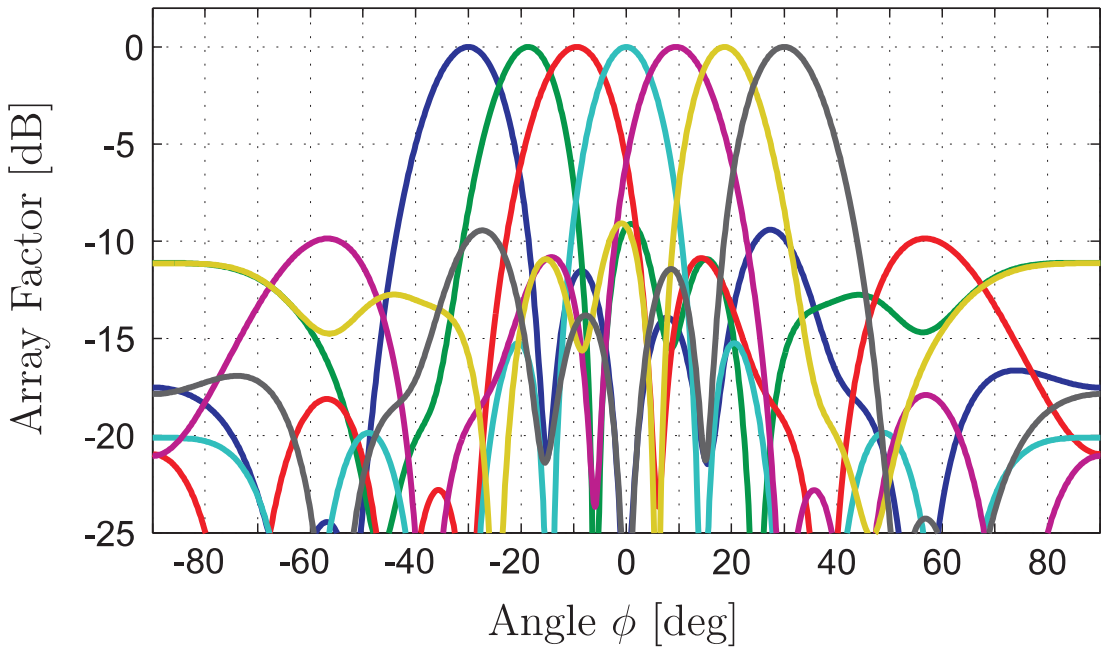

Figure 3-18 Normalized array factor of the simulation results for a small split-dielectric lens

In Figure 3-18 the maximum SLL is -9.1 dB. The -10 dB beamwidth varies between 21 degrees at the central beam port and 25.3 degrees for the outermost scan angle.
The small size of the lens is a limiting factor for a uniform amplitude tapering and therefore the maximum SLL is higher than in the larger lens. The proximity of the array ports to the beam ports makes it more difficult to implement a specific amplitude distribution along the array ports.
The lens with seven beam ports, nine array ports and two small dummy ports was realized on a substrate smaller than 5cm. This size corresponds to the test fixture. The fabrication and the transition between the two lens parts are done in the same way as it is done for the large lens. The lens parts are adhesively attached to a 0.5mm thick copper plate. For the measurement this copper plate is mounted on a brass block. A photograph of the lens is shown in Figure 3-19.

The first test of the lens, and especially of the lens interconnects, is done by verifying the symmetry of the transmission parameters. Figure 3-20 shows the transmission from the beam ports such that a solid line and a dashed line of the same color should corresponds to the symmetric ports. No asymmetries or regions with a bad transition can be identified and it can be concluded that the lens is contacted and working properly.

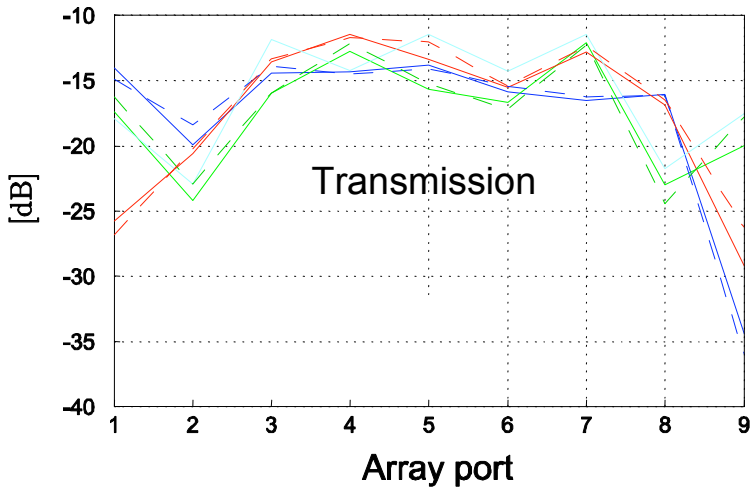

Figure 3-20 Transmission parameters of the small lens

From the S-parameters the array factor for each beam port is calculated. In Figure 3-21 the array factor is calculated from the measurement results and plotted together with the one from the simulation. The difference of the main

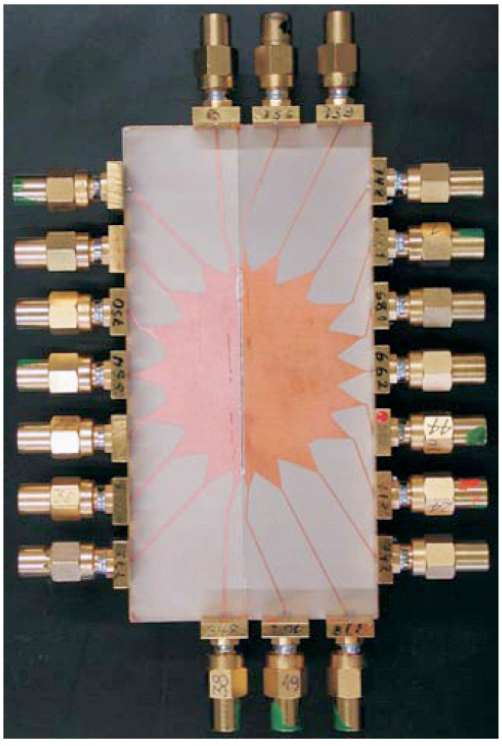

Figure 3-19 Realized small Rotman lens on a split-dielectric

beam level of 1.6 - 3.3dB is smaller than for the large lens, since the losses within the lens and along the shorter transition sections are smaller.

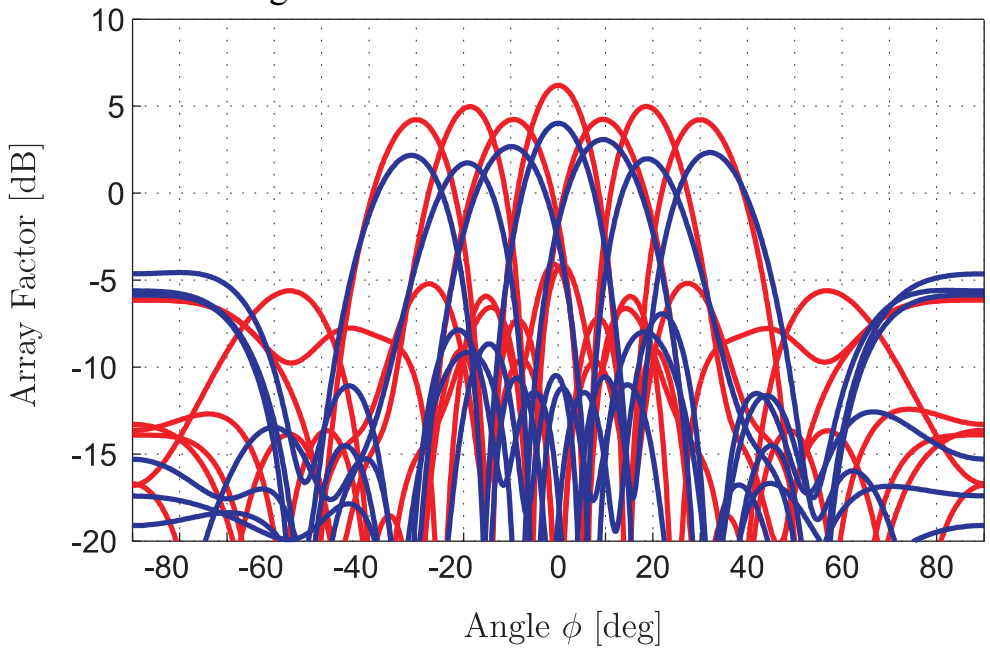

Figure 3-21 Array factor calculated from measured results (blue) and simulation results (red)

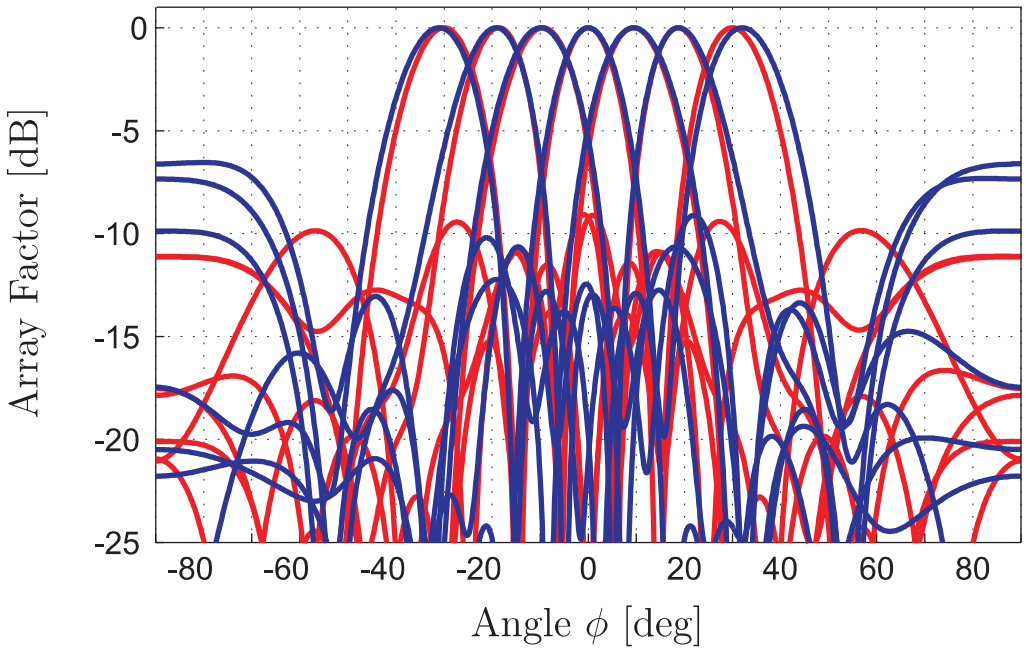

Figure 3-22 Normalized array factor calculated from measurement results (blue) and simulation results (red)

The shift of the principal scan directions can be well seen from the normalized array factor, shown in Figure 3-22. The principal beam directions for all beam ports are listed in Table 3-2. The larger shift for beam port seven may result from the fact that the transition from the connector to the microstrip line of this port was improper soldered.

Contrary to the large lens, there is no frequency at which the main beam directions for all beam ports coincide with the desired scan angles. We hypothesize based on the simulated current distributions that this comes from the fact that the influence of the standing waves within the lens and diffraction on the sharp corners of the ports is bigger than for the large lens and they cause an asymmetric phase error and amplitude tapering.

The Figure 3-23 shows the power distribution over array ports, dummy ports, beam ports and losses in the lens.
Compared to the large lens, the losses within the lens are much smaller, but the reflections increase, such that up to half of the power is reflected back to the beam ports. The power transmitted to the array ports equals the one transmitted to the dummy ports.

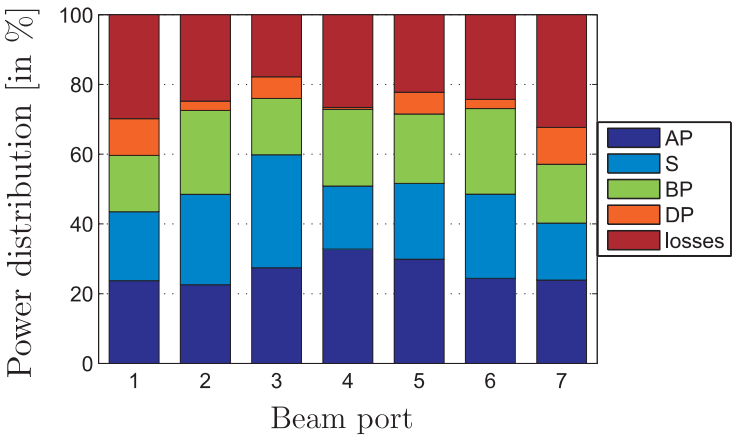

Figure 3-23 Power distribution over port groups for the small dielectric split lens

The small Rotman lens using a split-dielectric approach opens new application for integration of small lenses in diverse low-cost front ends.

Chapter 4

Folded Rotman lens based on LTCC

Abstract - The dielectric splitting of the conventional Rotman lens introduced in the previous chapter can still be insufficient in terms of size reduction for integration into a very compact RF front end. A major drawback is also the realization of different dielectric permittivities in one single material layer. In this chapter two key components, folding of the structure and gradual change of the dielectric constant will be elaborated. In LTCC technology, one can introduce empty vias in different densities to alter the effective dielectric constant. Additional folding of the lens structure across different layers leads to structures that are more compact.

4.1 Introduction

The inner lens, the tapered input and output ports as well as the absorbing sidewalls determine the real-estate requirement of the Rotman lens. This is a major drawback for utilization in compact systems. In order to make the design more compact, a new folded design of the Rotman is presented at 5 GHz.

Such folded 2D lens can be realized in LTCC technology. The gradual modification of the dielectric constant along the lens is achieved by using a periodic lattice of air vias similarly to the micro machining technique used in [26]. The difference is that there are no holes in the ground plane, thus avoiding the major problems at higher frequencies as described in [26]. Ellis and Rebeiz [28] state that for a rectangular hole pattern the effective dielectric constant can be calculated as

$$\varepsilon_{eff} = \varepsilon_r \left(1 - \frac{\pi D^2}{4W^2} \right) \qquad (4.1)$$

where D is the hole diameter an W the distance between two adjacent holes.
Another advantage of a realization based on the LTCC compared to a lens using multiple dielectric substrates would be the continuous, uninterrupted metallization eliminating the phase errors due to the interconnections of the lens parts.
The LTCC technology is the key for the folding of the Rotman lens. The lens utilized here to validate the folding principle is a uniform dielectric one. Once the lens-folding concept is validated, it can be easily combined with the concept of split-dielectric.

4.2 Simulation of the folded Rotman lens

First, an unfolded Rotman lens (Figure 4-1) is implemented in stripline at 5 GHz to investigate its performance and to show the effect of the dummy ports.

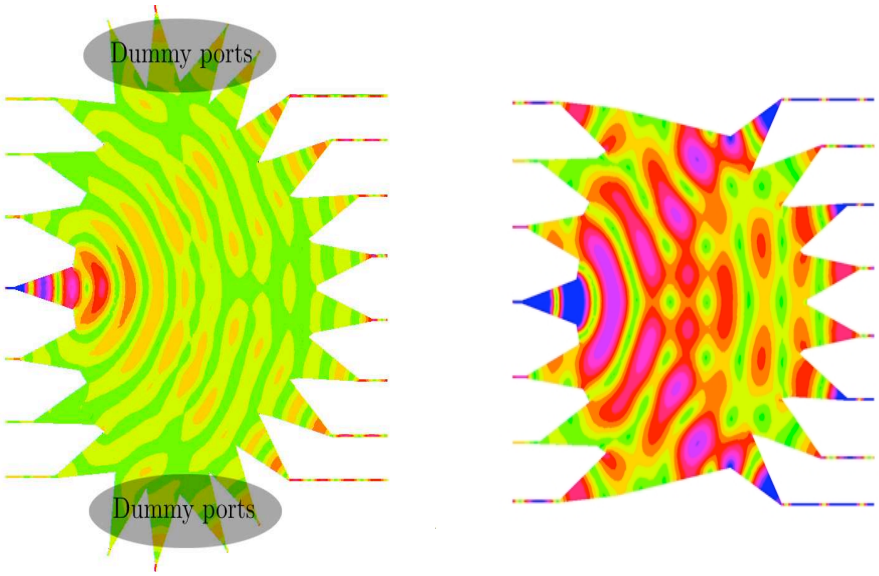

Figure 4-1 Current distributions on the 5GHz Rotman lens with and without dummy ports

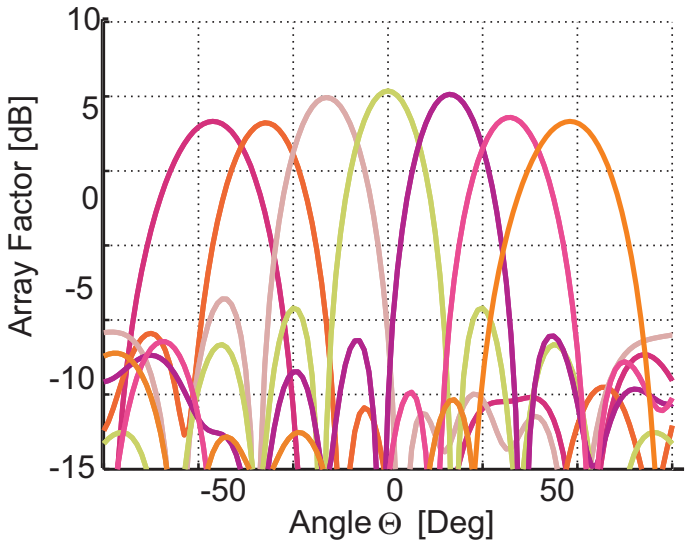

Figure 4-2 Array factor of lens simulated in Designer

The design comprises seven input ports and eight output ports implemented on a $96\mu m$ thick *DuPont 951* LTCC tape system $\varepsilon_r = 7.8$. With a focal length of $f_1 = 3.8\lambda_0$ the lens measures 81.6mm. The input ports on the beam port arc are positioned at $\alpha = [\text{-}32^\circ, -22^\circ, -12^\circ, 0^\circ, 12^\circ, 22^\circ, 32^\circ]$ and the beam directions are $\psi = [-40^\circ, -26^\circ, -13^\circ, 0^\circ, 13^\circ, 26^\circ, 40^\circ]$. The lens is designed to feed an array of eight antennas corresponding to the eight output ports on the right side of the lens.

Figure 4-2 illustrates the simulated array factor including the effect from the dummy ports. The simulation is done using *Ansoft Designer*. The seven beams have a side lobe level (*SLL*) below -10dB over a bandwidth of 2 GHz, centered at 5 GHz. Hence, this lens shows a very good performance over a wide bandwidth.
The stripline ports at the input and output of the Rotman lens are linearly tapered. Due to the taper the length of the ports increases too.
To demonstrate once more the effect of the dummy ports, Figure 4-1 shows two different current distributions of the 5GHz lens with and without the dummy ports. In both cases, the feeding is applied at the center input port corresponding to the broadside beam direction. The wave front of the lens with dummy ports in the left picture of Figure 4-1 shows uniform cylindrical wave propagation. If the spill over at the sidewalls of the lens is not absorbed, it reflects back towards the inside of the lens resulting in standing waves as shown in the right picture Figure 4-1. These reflections change the phase and

amplitude distributions at the output ports and degrade the overall performance of the lens.
Although the performance of the lens without dummy ports deteriorates, we will not consider in a first step the dummy ports for the folded Rotman lens. Later in an LTCC realization, folded dummy ports are included in addition to a double folding of the Rotman lens.

The 5GHz planar lens designed in the previous section cannot be realized in LTCC by most manufacturers because it exceeds the overall size limitations of the standard LTCC process. Therefore a folded Rotman lens has been developed, using the multilayer capabilities of LTCC based on the *DuPont 951* material.

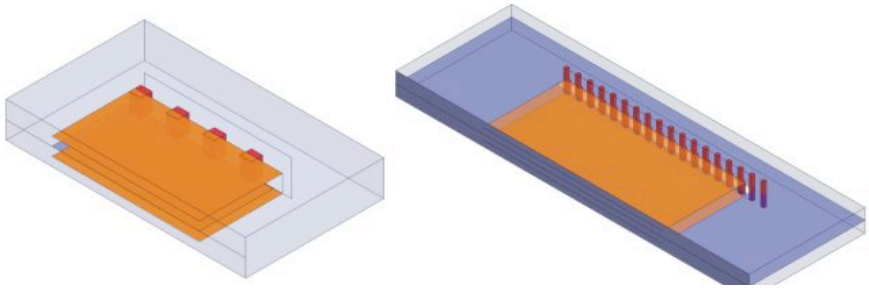

LTCC stripline transition of small and medium width

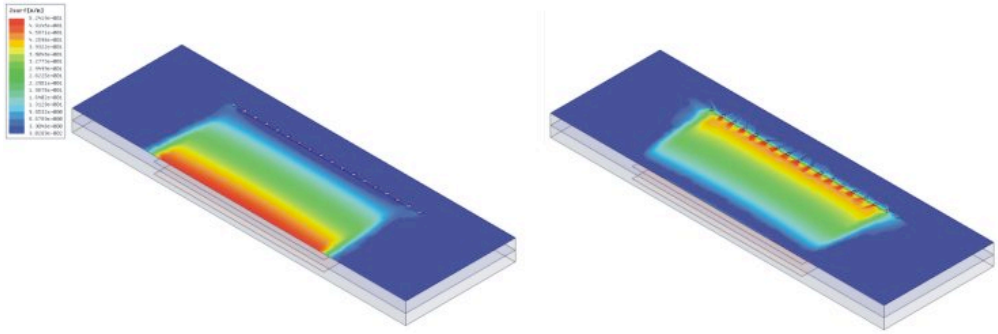

Current flow through the vias of the medium size transition

Figure 4-3 Transition with 4 and 16 vias by constant via spacing. The lowered plots correspond to the current magnitude of the 16 vias transition at different time steps.

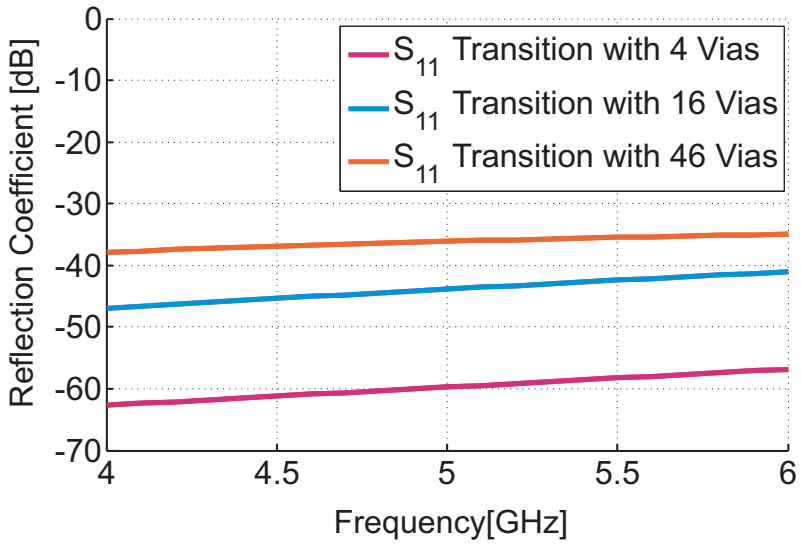

Figure 4-4 Reflection coefficient of the via transition with different widths simulated in HFSS

Essential for folding the lens as drawn in Figure 4-5 is a geometrically wide stripline transition to interconnect the different layers of the lens. This transition consists of a slot opening in the common ground plane of the upper and lower half of the lens. The signal is passed though the slot opening by means of standard vias. The outer ground planes are also connected by means of vias.

First, the transition is optimized separately with the help of a full-wave EM solver, taking the parameters of the slot, the vias, and their positions into account. The tape thickness of the various layers is kept at 0.096mm. The inner ground plane is sandwiched in the middle of four layers of substrate and has a slot opening with the dimensions 0.2-0.25mm. The vias, simplified to a rectangular cross-section of 0.125x0.125mm, have been spaced at a distance of 0.4mm. At the far end of the slot, the two outer ground planes have to be connected by a similar via fence with via spacing of 0.4mm.

Figure 4-4 compares the scattering parameters of this 0.1mm wide stripline transition with a high number of vias to a simplified transition with only four vias and 1.4mm width of Figure 4-3. The input reflection coefficients are determined by the transition geometry and remain in both cases below -30dB over a 50% bandwidth at 5GHz. This was confirmed by a set of simulations including angle-dependent incident wave fronts on the slot region.

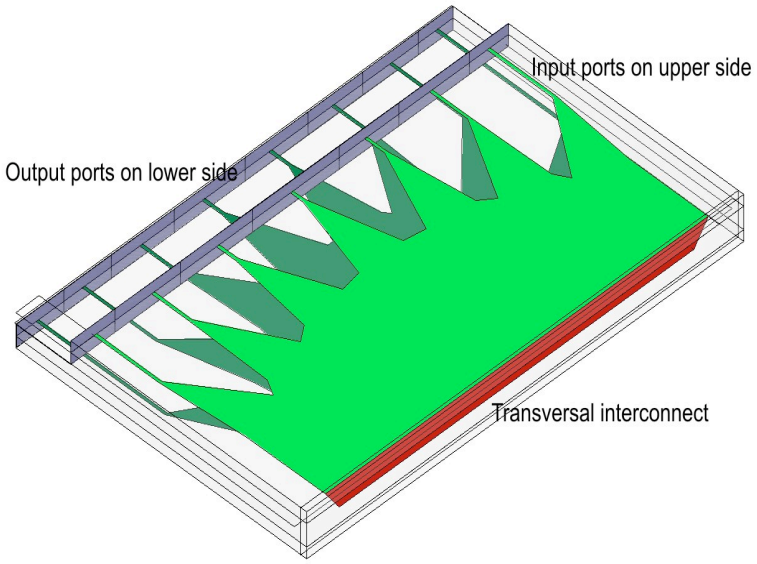

Figure 4-5 Compact folded Rotman lens at 5 GHz without dummy ports

With this optimized transition, the lens can be folded along a middle line as shown in Figure 4-5.

The lens was simulated using *Designer* as well as *HFSS*. *Designer,* based on the Method of Moments (MoM), yields fast results for the overall performance. It includes the option of simulating vias using a 2.5D model. The drawback is the computational effort, which increases significantly with the number of vias.
In a second step, *HFSS* simulation was used and the vias were replaced by a perfect electric sheet in order to reduce the computational effort. This approximation provided excellent results for the simple transition as well as for the complete folded lens. The full 3D *HFSS* and the faster *Designer* together ensure a correct and fast design procedure.

Figure 4-6 and Figure 4-7 show the current distribution of the unfolded and the folded Rotman lens, respectively, both without dummy ports. It can be observed that the current distribution along the lens compare well. This current distribution includes reflection from the lens sidewalls (no dummy ports). Similar standing wave and multiple reflection patterns can be noticed in both the unfolded and the folded design.

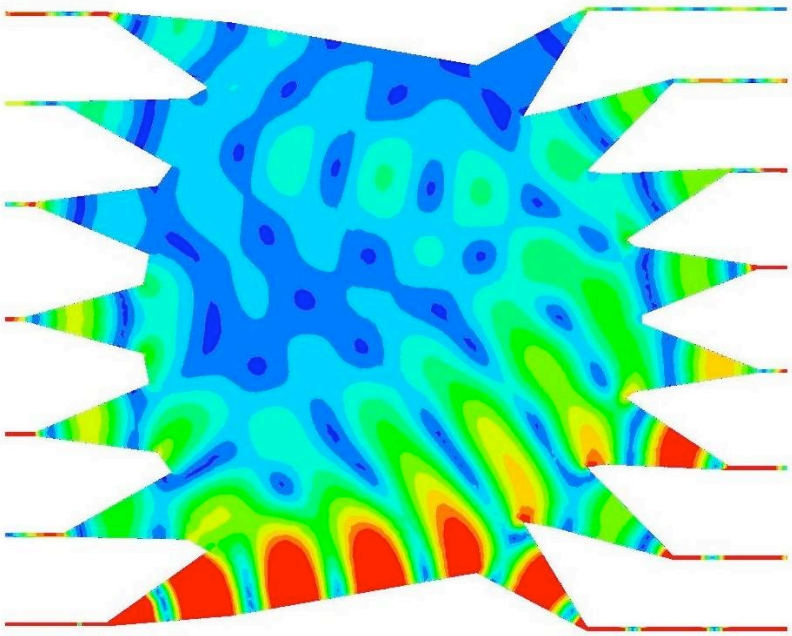

Figure 4-6 Current distribution on the unfolded Rotman lens

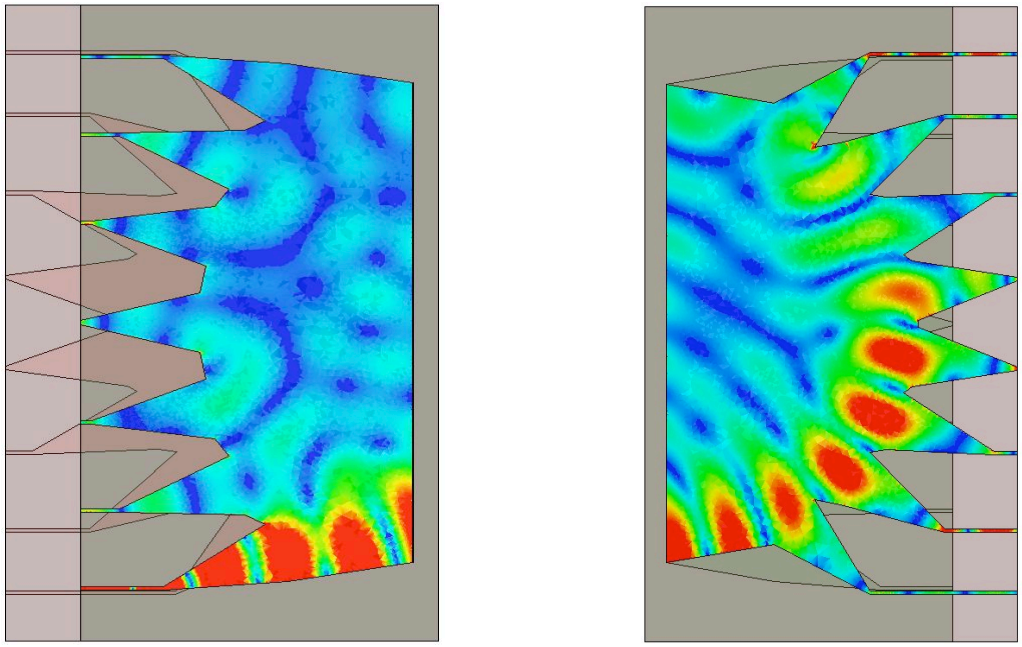

Figure 4-7 Current distribution of the folded Rotman lens

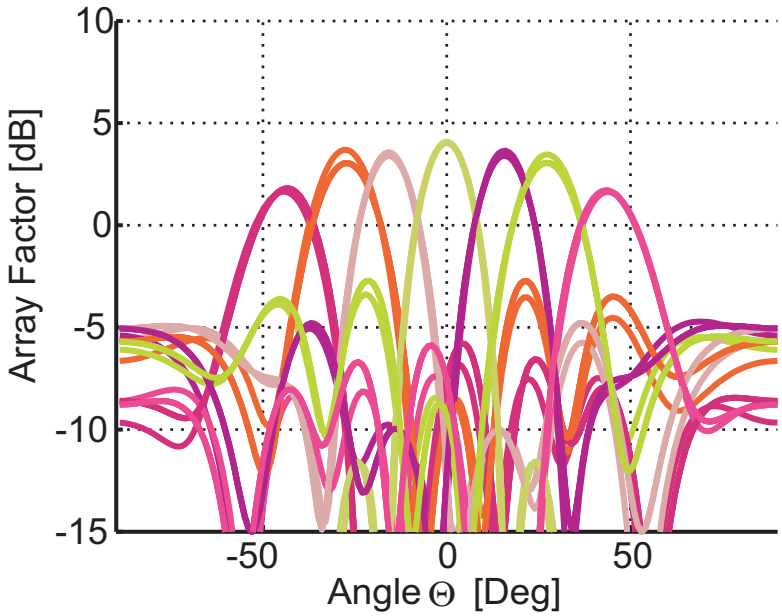

Figure 4-8 Array factor of the folded and unfolded Rotman lenses simulated with Designer (higher amplitude corresponds to the unfolded lens)

Figure 4-8 shows the array factor of a lens-fed 8-radiator array. As expected the array factor deteriorates due to the elimination of the dummy ports. The *SLL* is below -7dB. However, array factors of the unfolded as well as of the folded design agree very well. Once the dummy ports will be connected to the folded Rotman lens the SLL should match the unfolded lens with absorbing ports.

4.3 Realization and measurements of the folded Rotman lens

The results from the previous chapter validate the folding procedure from the simulation perspective. Following the schematic in Figure 4-9 a novel design based on a double folding of the interior lens part and an additional one of the dummy ports is manufactured. The design is realized on an LTCC Ferro tape using 10 stripline layers.

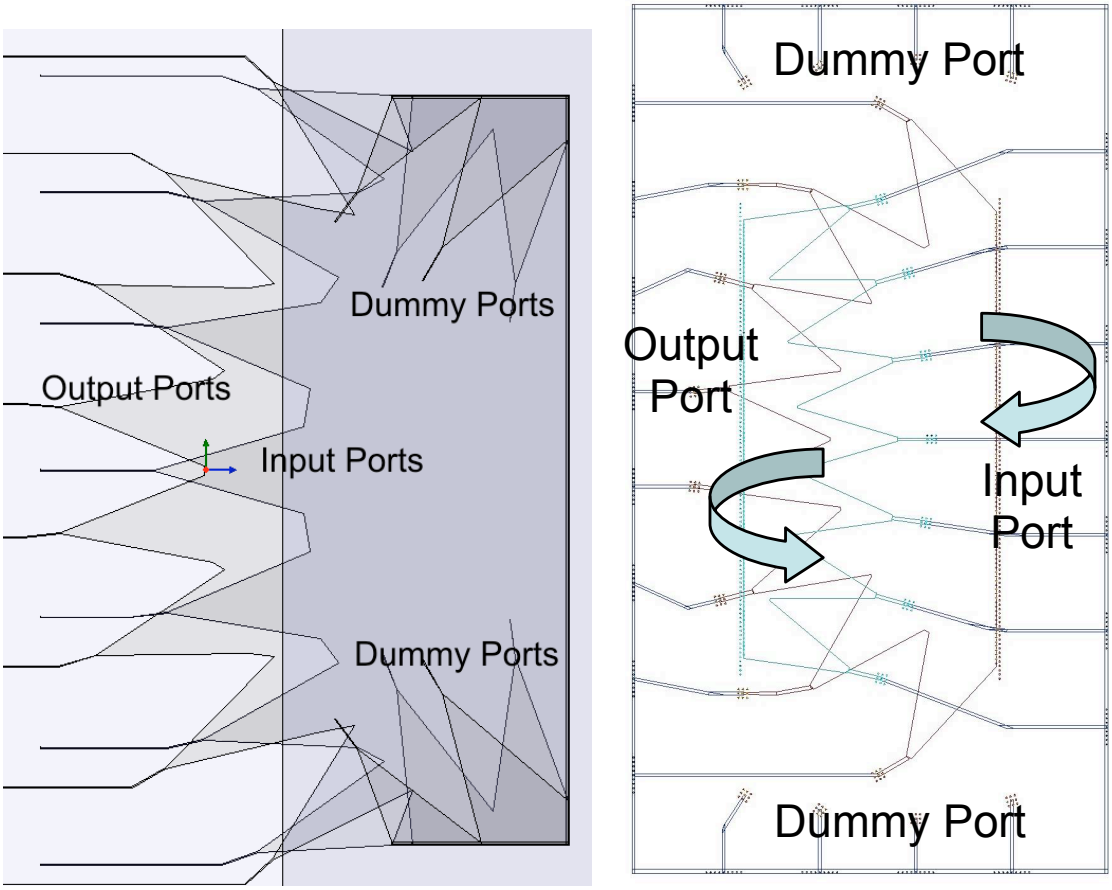

Figure 4-9 Folding map of the stripline lens with one (left) and two (right) folding lines

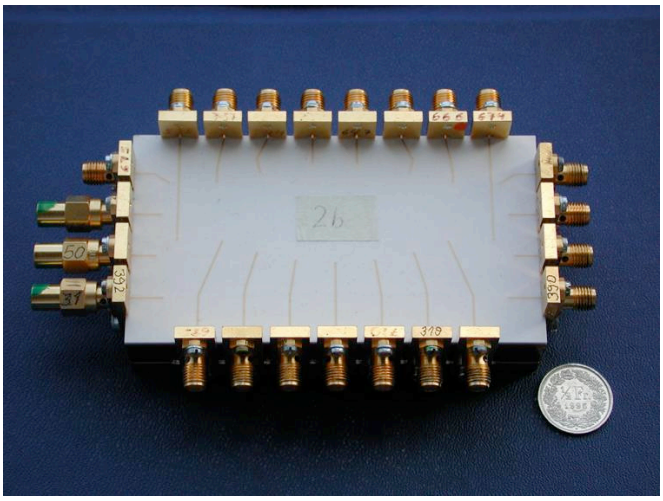

Figure 4-10 Picture of realized double folded Rotman lens (size compared to a Swiss franc)

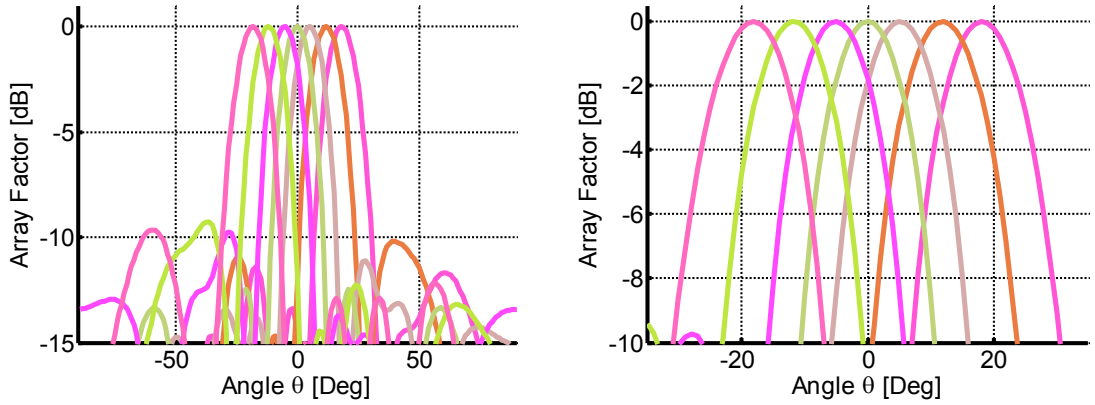

Figure 4-11 Normalized array factor of the measured folded lens

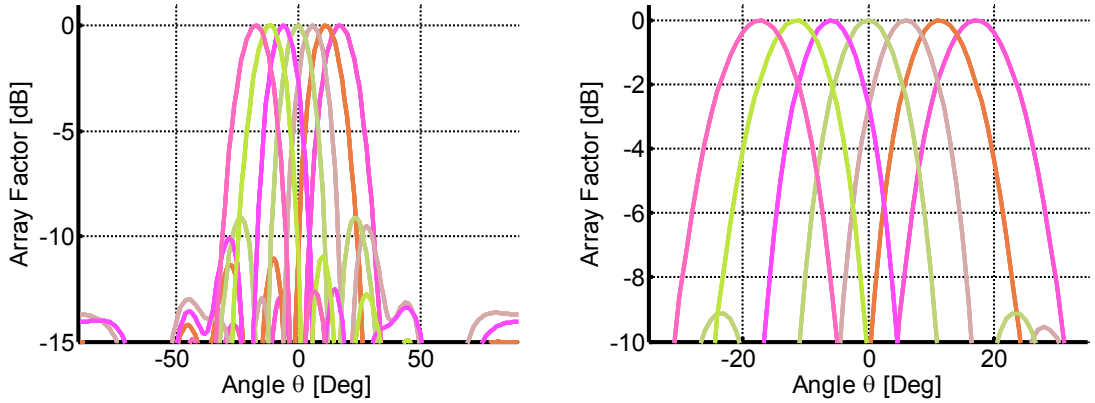

Figure 4-12 Normalized Array factor of simulated folded lens

The measured transmission coefficients are used to compute the array factor of the double-folded Rotman lens. Results of Figure 4-11 are compared with the simulation of the unfolded lens in Figure 4-12.

Summary of the folded Rotman lens

First, a Rotman lens capable of scanning seven different directions using 8 antennas was designed for 5GHz. In order to reduce the overall size of the lens a simple and effective folding concept is introduced. The folding is realized with the help of a wideband stripline transition using the specifications of the LTCC process regarding via spacing. Simulation results

have shown that folding the lens without dummy ports does not deteriorate its performance. Furthermore, the inclusion of dummy ports in the folded lens will result in a performance similar to that of the unfolded design with dummy ports. At this point, a double folded lens with additional folding of the dummy ports was realized. The measured and simulated data match and validate the folding approach. The principle of folding and substrate splitting combined in one single technology is extremely powerful.

Chapter 5

Stripline Butler matrix using LTCC

Abstract - This chapter describes a novel stripline configuration for an 8x8-port Butler matrix centered at 5 GHz. The structure is implemented in LTCC. The main goals are the compact integration using the advantages of three-dimensional structuring. LTCC is by default a multilayer technology optimal for the design of the Butler matrix components: couplers, phase shifters, and especially crossings. The chapter focuses on the possibilities for Butler matrices using stripline design.

5.1 Introduction

The mathematical derivation in the introduction showed that the Butler matrix is the matrix with the lowest number of components compared to any other matrix. This is done using the analogy to the FFT. In Chapter 5 the Butler matrix realizations will be reviewed, limitations will be pointed out and a solution to overcome the limitations will be introduced.
The Butler matrix consists of three building blocks: interconnected and fixed phase shifters, 3 dB power dividers. An example of a $N = 8$ size matrix is shown in Figure 5-1. These building blocks are interconnected in such a way that feeding an input port produces an equal current distribution and a corresponding specific linear progressive phase shift along the output ports. The matrix will produce N orthogonally spaced beams, sometimes called component beams. Orthogonal means that the beams do not couple [25] and overlap at the 3.9 dB level as drawn in the Figure 5-2.

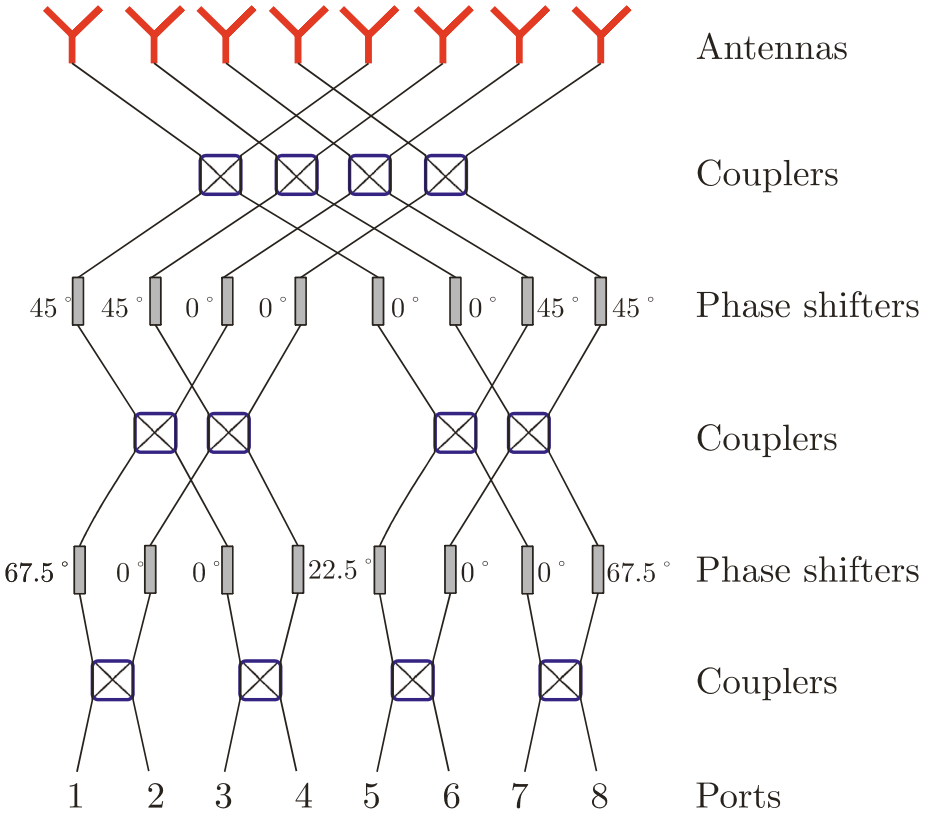

Figure 5-1 Schematic of an 8x8 Butler Matrix

The performance of the Butler matrix depends critically on the bandwidth of the 3 dB couplers and the constant frequency response of the phase shifters. Due to the interconnection of all input ports with all output ports, numerous line crossings occur inside the matrix. The number of couplers (H_a) and corresponding line crossings (C_a) are given by (5.1).

$$C_a = 2C_{a-1} + 2^{a-1}(2^{a-1} - 1), \forall a \geq 3; C_1 = 1, C_2 = 2, \tag{5.1}$$
$$H_a = a\,2^{a-1}$$
$$a = \log_2 N$$

Obviously, increasing the order of the matrix requires an increasing number of couplers, phase shifters and a much higher number of crossings. The number of crossing thus limits the practical realization of a Butler matrix. Therefore, there is a large number of publications considering matrices of order 4 and a smaller number dealing with order 8 and higher.
Butler matrices for high-power applications are generally implemented using rectangular or coaxial waveguides. An interesting approach is also the

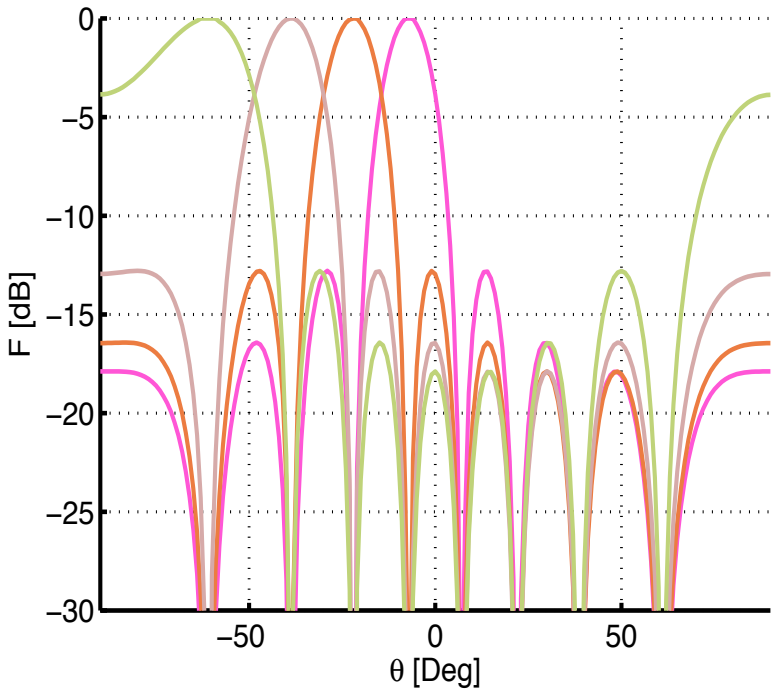

Figure 5-2 Array factor of an ideal 8x8 Butler matrix(only left half)

concept of substrate integrated waveguide using via fences [29] and [30]. The most compact waveguide Butler matrix of order 8 is reported in [31]. The geometry of this matrix is extremely challenging in the design and even more in the realization. This is why the majority of reported matrices of larger size $N \geq 8$ are in the area of lower power and use printed transmission lines. Even these realizations are limited to the order of $N = 8$. Two types of crossings have been developed. The first uses a common ground plane for two different microstrip networks, which can be inter-coupled by means of coupling slots. With the double-sided substrate, the crossings can be avoided as seen in [32] and [33] for two high temperature superconducting Butler matrices. The second approach described first in [34] and implemented also in [35] uses zero degree hybrids as crossing structure. This allows realizing all the crossings in one layer of microstrip. The drawbacks are the overall size, reduced bandwidth and the additional reflections at the crossing points.
Both described structures can be implemented for matrices up to $N \leq 8$. At this point, we introduce the LTCC technology. Having a multilayer tape system the crossings can be realized in different ways.
The 3 dB coupler, the crossings, and the phase shifters can be interconnected on different layers by means of vias transitions. The LTCC technology shows great promise to eliminate the problems mentioned using the 3D integration.

5.2 The 8x8 stripline Butler matrix at 5GHz

The Butler matrix was designed in stripline technology with a characteristic line impedance of 30Ω using five layers of *DuPont 951* material with dielectric constant of $\varepsilon_r = 7.8$. Figure 5-3 shows the structure of a 3dB coupled-line directional coupler in LTCC. Conventional coupled-line couplers exhibit a broad bandwidth (typically around 25%), but achieve loose coupling only (typically less than 10 dB) [36]. In contrast, branch-line or rat-race couplers show 3-dB coupling, with the shortcoming of small bandwidth (typically less than 10%) [37]. A widely used coupler providing both broad bandwidth and tight coupling is the Lange coupler [38]. However, a disadvantage of this coupler is the fact that it requires cumbersome bonding wires with different parasitic effects at high frequencies. The attempt to integrate the bonding wires in LTCC by using vias proved unsuccessful due to the smallest available via diameter. Integrating the coupled-line directional coupler using a stripline approached proved to be the most elegant solution to overcome the poor coupling level while maintaining the high bandwidth.
A directional coupler is characterized by the fact that the input power is transmitted to the output ports 3 and 4 in Figure 5-3, while port 2 is isolated. A phase difference of 90 degrees is achieved between port 3 and 4 over the entire bandwidth of 3-dB coupling. The characteristic impedance of the coupling section is matched to the impedance of the external lines by adjusting the widths of the lines and the selection of the dielectric layer in between.

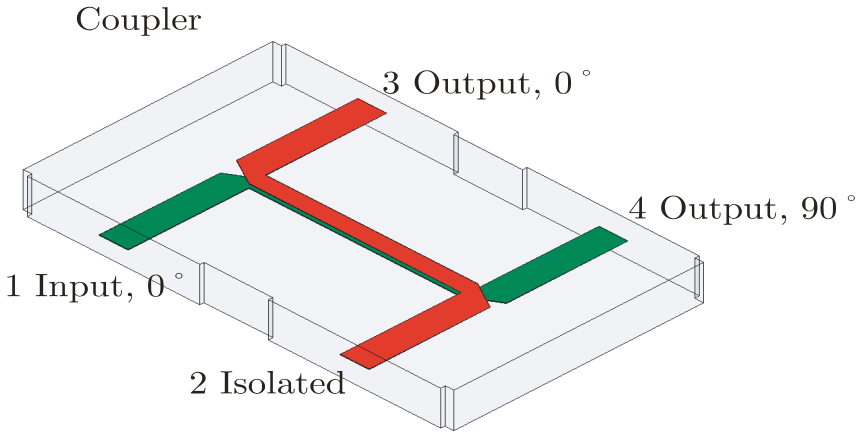

Figure 5-3 Broadside 3dB directional coupler

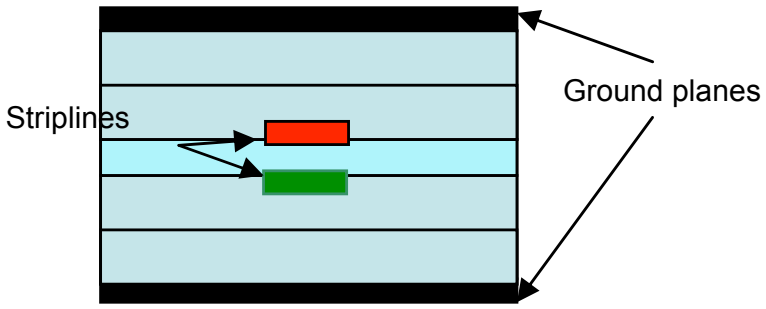

Figure 5-4 Cross section of the coupled striplines

Since the characteristic impedance of the coupling section is determined by the combination of even and odd modes, field simulations using *HFSS* (Ansoft Corp.) are used for the optimization of the coupler. A model for the broadside type of directional coupler was introduced by [39]. Additionally the authors propose an analytical model for compensating the discontinuity in the stripline width.

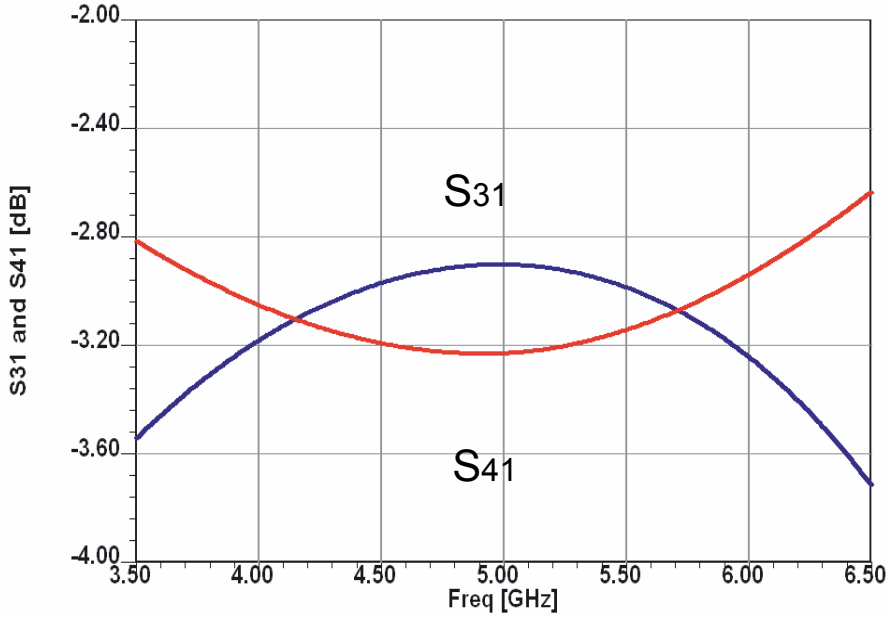

Figure 5-5 Transmission characteristics of the coupler

The thickness of the middle layer of the broadside coupling section in Figure 5-4 is critical for the design of the coupler. *DuPont 951* tape system offers only two tape thicknesses, of 96μm and 208μm after shrinkage from the firing process.
The thinner tape had to be placed between the coupled lines to achieve a near-equal power division (Figure 5-5) between port 3 and port 4, a high isolation between port 1 and port 2, and a low input reflection coefficient as seen in Figure 5-6. The ideal S-parameters of a coupler are given by (5.1).

$$S = \frac{-1}{\sqrt{2}} \begin{bmatrix} 0 & 0 & 1 & j \\ 0 & 0 & j & 1 \\ 1 & j & 0 & 0 \\ j & 1 & 0 & 0 \end{bmatrix} \tag{5.1}$$

It can be seen that both S_{31} and S_{41} have values close to -3dB in the frequency range between 3.5GHz and 6.5GHz. The high isolation of port 2 and low input reflection coefficient are shown in Figure 5-6, where the values of all the three S-parameters (S_{11}, S_{22}, S_{21}), are below -22dB in the frequency range of interest.

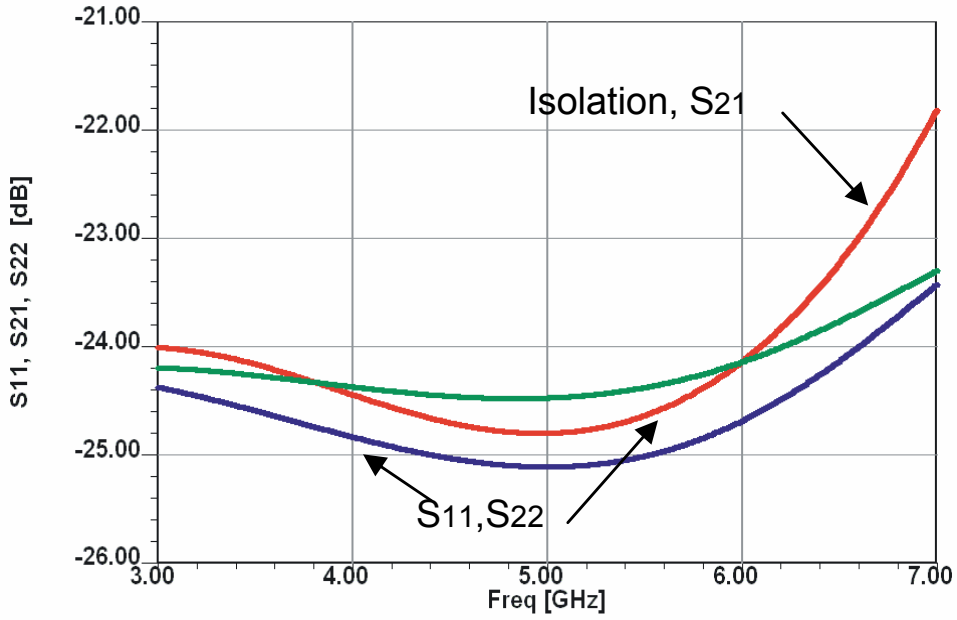

Figure 5-6 Isolation and reflection coefficient of the simulated coupler

The large number of crossovers has been one of the main drawbacks of practical Butler design. In the following LTCC implementation, via transitions are used to cross two striplines on different layers with a height difference of three layers (512µm). Figure 5-7 shows the obtained coupling of less than -35dB. The return loss remains below -30 dB over the bandwidth of interest. This can be achieved by two vias at the edge of the striplines to be connected. The crossing striplines are orthogonal and ensure that the two TEM modes on the lines stay orthogonal, too. An additional crossing with a height difference of two layers (304µm) is designed by removing the metallization in the middle of the wider stripline (Figure 5-8). This reduces the parasitic capacitive coupling and maintains an overall crosstalk below -35 dB. Bona reported in [40] a similar Butler matrix of order four using suspended striplines. The crossings are realized by a reduction of the thickness of the transmission line at the crossover position, which would reduce the strong capacitive coupling. As a result, the matching is deteriorated and has to be compensated by additional open stubs. The stubs, on the other hand, increase themselves the coupling between the crossed lines. An optimum between matching and coupling has to be found in this LTCC design. Help comes from the four layers, which can increase the coupling width and reduce the parasitic coupling capacitance.

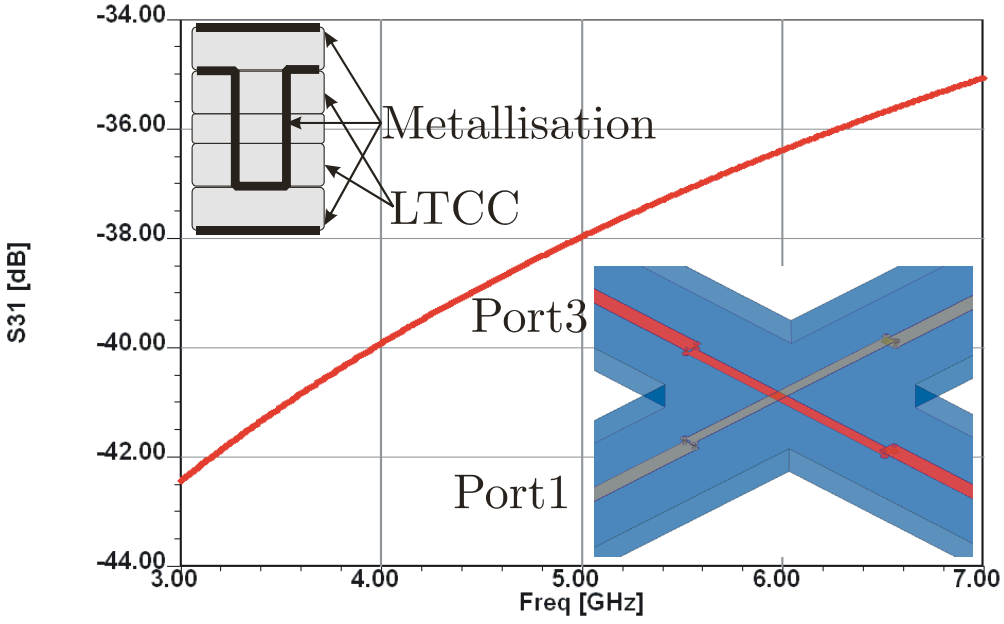

Figure 5-7 Crosstalk S_{31} at the crossover of two perpendicular striplines

The phase shifters are the third component to constitute the matrix. Meandered lines were employed to provide the necessary shifts corresponding to $22^{\circ}, 45^{\circ}, 67.5^{\circ}$. The 3 different line lengths have to match the geometrical requirements of the design ensuring additional compactness of the overall matrix. Each of the meander lines crosses the middle layer using two edge vias. All via transitions of the crossing lines as well as of the meandered lines have to be characterized for the additional phase they introduce and compensated by the corresponding line length.

After designing and optimizing the components to meet the best performance (maintaining the crossover coupling and the return loss below -30dB), the parts were combined to compose the matrix. Figure 5-8 is a print of the integrated Butler matrix in *HFSS* [27] with all the previously specified subcomponents.

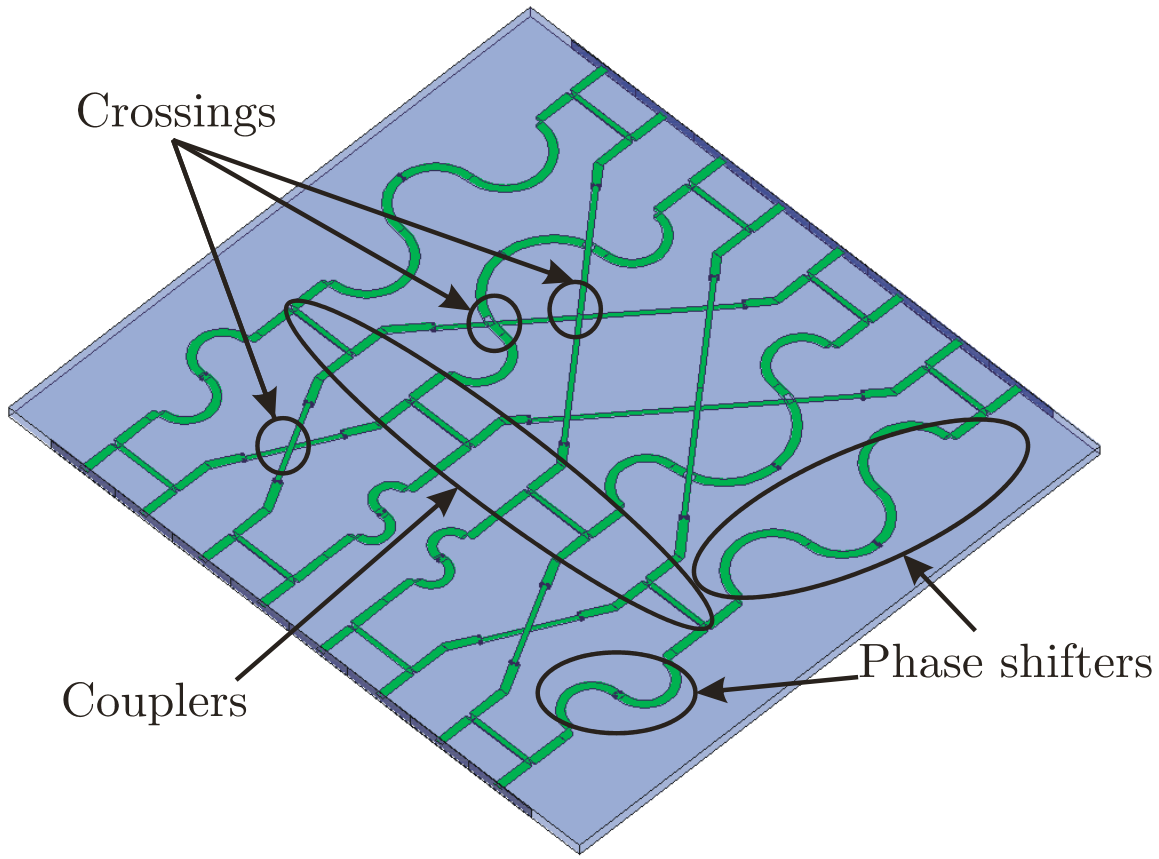

Figure 5-8 Complete Butler matrix using stripline as transmission lines

The entire Butler matrix was simulated using *Designer* and *HFSS* from Ansoft Corp[27]. The simulation of the complete system in *HFSS* proved to be very important because of the spurious parallel-plate modes excited at the numerous transitions, leading to standing waves as seen in Figure 5-9.

In Figure 5-9, one port of the matrix is fed by a source and the current density of one of the ground planes is plotted. The signal routing along the multiple striplines is highlighted by the current magnitude. Overlaid the strong standing wave from top to bottom is visible. This parallel-plate mode can be eliminated by enclosing every stripline with via fences connecting the two grounds as described in [41]. The enclosing of the striplines and couplers by vias changes the characteristics of the individual components, requiring a redesign using *HFSS*.

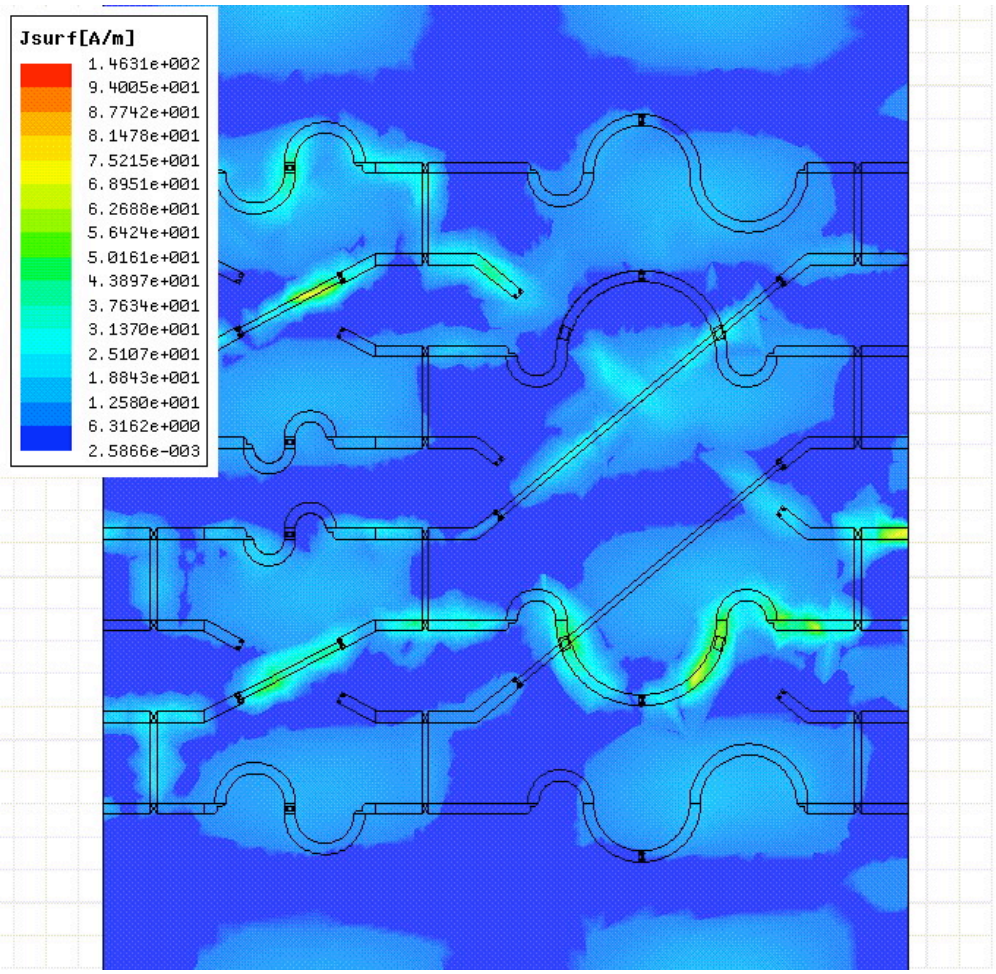

Figure 5-9 Current density in the Butler matrix with one active port

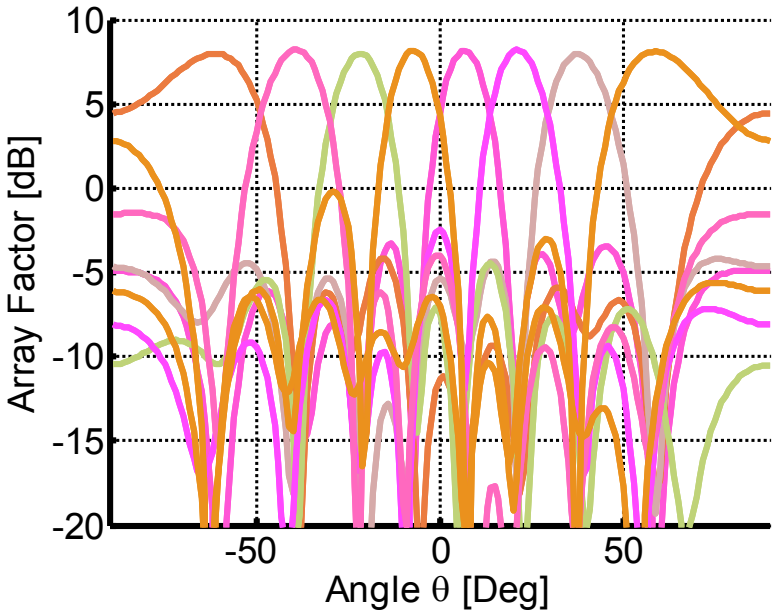

Figure 5-10 Array factor at 5GHz, HFSS simulation

Compared to the ideal array factor plotted in Figure 5-2 the simulated or measured ones will reveal the performance of the matrix.
The amplitude and phase results, from the *HFSS* were used to generate the array factor in Figure 5-10 and Figure 5-11.

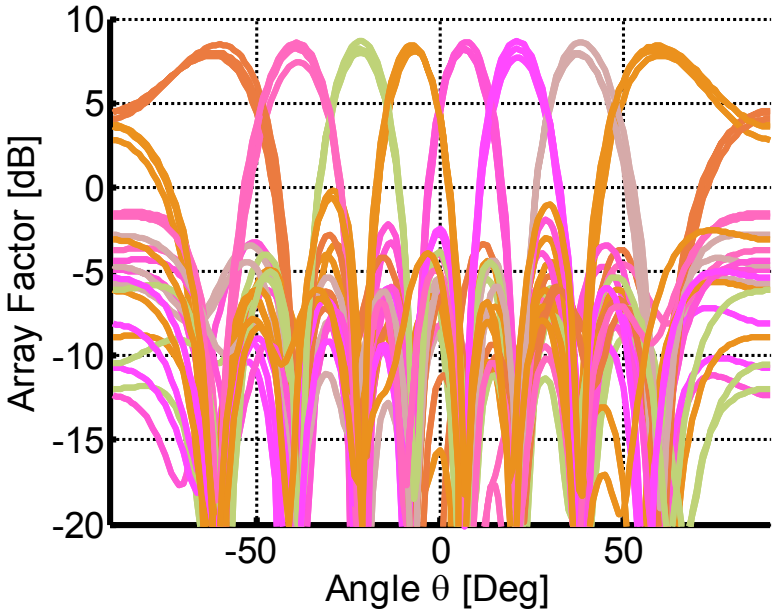

Figure 5-11 Array factor at [4,5,6]GHz, HFSS simulation

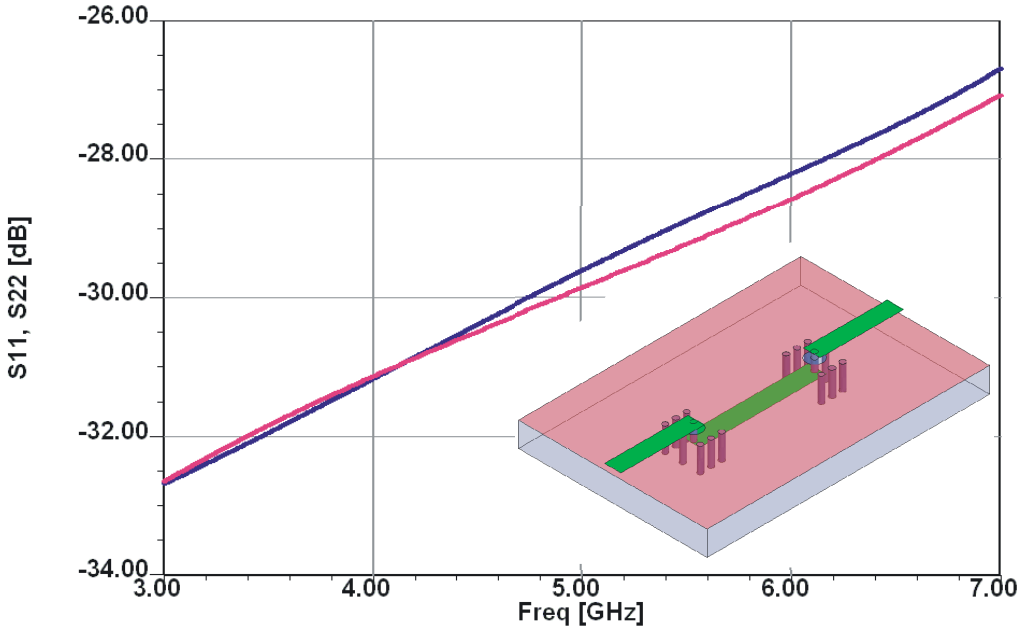

Figure 5-12 Computed stripline-to-microstrip transition for measurement setup

In both plots, one can distinguish the separate eight beams corresponding to the eight active input ports and read the SLL. The SLL is below -10dB over a bandwidth of 2GHz around the center frequency of 5GHz. The simulated beam directions and beamwidths are in excellent agreement with the ideal values.
In the frequency range 4 and 6GHz, the beam directions of the main lobes of the simulated Butler matrix exhibit a maximum variation of ±2º from the desired values. The manufactured matrix is the last step to validate the concept.

In order to measure the matrix structure, a microstrip interconnect is required. Therefore, a transition from stripline to microstrip is required. Different transitions for multilayered structures were reported [42-44]. Figure 5-12 shows the computed input and output return loss off a back-to-back microstrip-to-stripline-to-microstrip transition. The vias positions and the opening in the common ground plane optimize the double transition; the input-reflection coefficient does not exceed -28 dB across the 4-6 GHz band.

5.3 Results of the realized stripline Butler matrix

The complete structure of the LTCC matrix is pictured in Figure 5-13. In the middle part, the outlay of the *AutoCAD* drawing is superimposed on top of the ceramic die. The size of the Butler matrix realized in LTCC is 46mm by 46mm. The size of the LTCC substrate is 100mm by 92mm. The ceramic die includes a separate coupler and different calibration structures. The size of the components and the additional line connections from the structure to the measurement setup add losses and reduce the performance and efficiency of the Butler matrix.
The efficiency calculated from the transmission of the j-th input port to the output ports is defined by (5.1) and has been plotted over frequency in Figure 5-14.

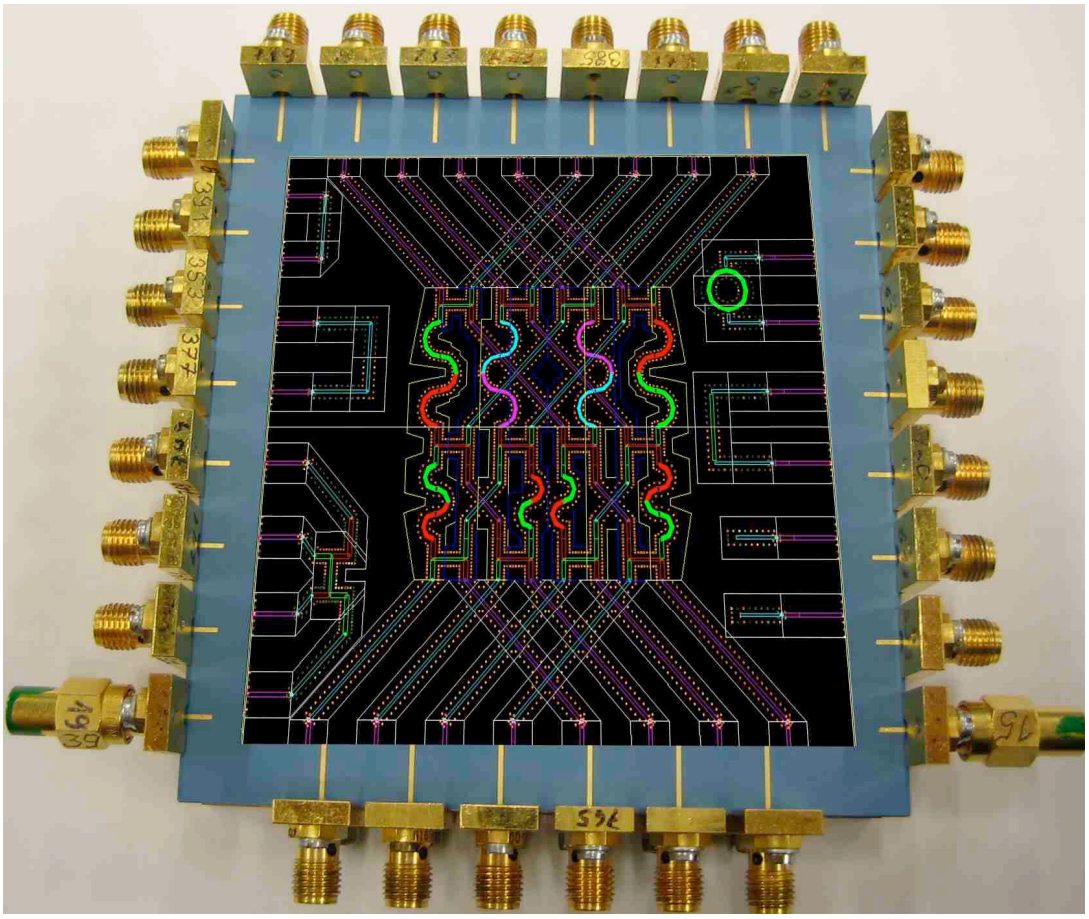

Figure 5-13 LTCC structure with superimposed layout of the Butler matrix

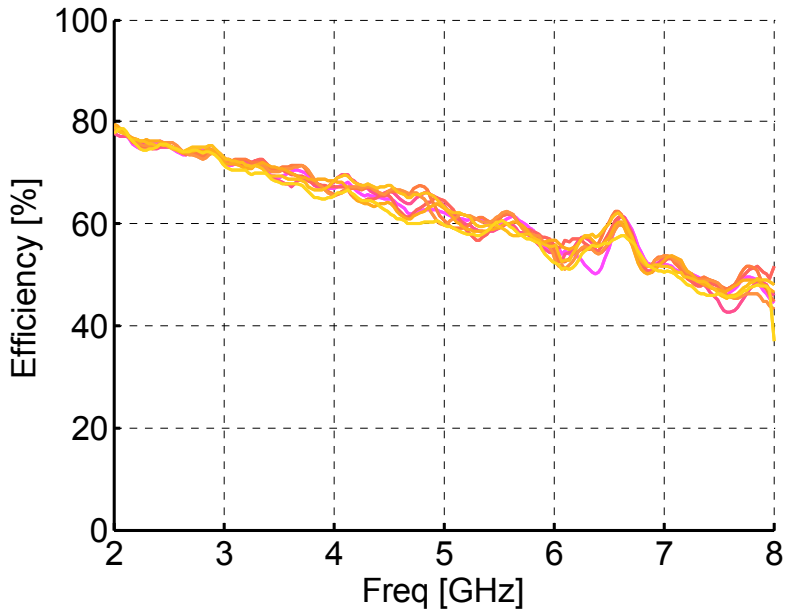

Figure 5-14 Efficiency of the entire Butler matrix

$$Efficiency = P^{transmit,j} = \sum_{i=9}^{16} \left| S_{i,j} \right|^2 \tag{5.1}$$

The efficiency drops over the frequency due to the increased losses. In the range of operation, the efficiency stays above 60% including all the losses of the long interconnecting lines and of the measurement setup. The losses of the matrix itself lead to an efficiency greater than 80%.

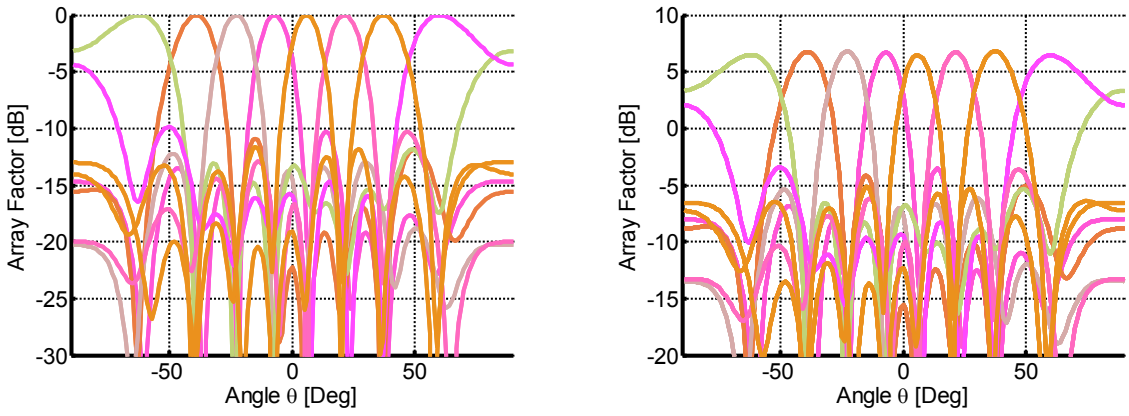

Figure 5-15 Measured normalized/not normalized array factors at 5 GHz

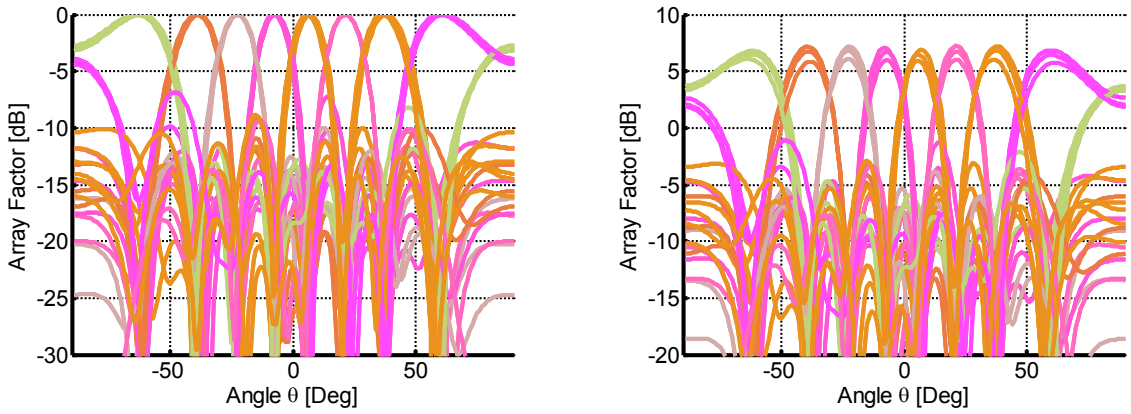

Figure 5-16 Measured normalized/not normalized array factors at 4GHz,5GHz and 6GHz

The array factors for the eight different beam ports measured at the center frequency 5GHz are shown in Figure 5-15. Comparing the obtained results with the target values validates the design. In the frequency range between 4 and 6 GHz, the beam directions of the principal lobes exhibit a maximum variation of ±2º from the desired values as seen in Figure 5-16. This is the same value as in the simulation. The return loss in Figure 5-18 is for all the ports above the 15dB over the operating bandwidth.

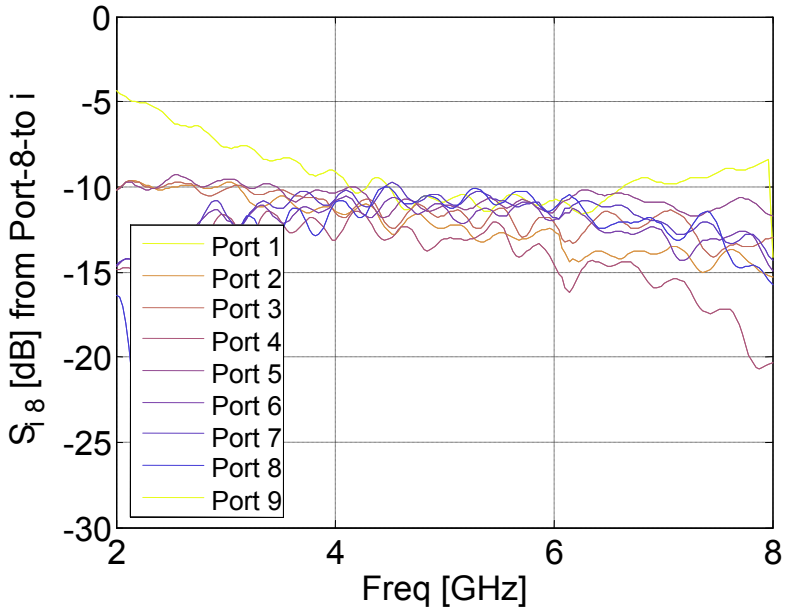

Figure 5-17 Transmission coefficients from Port 8 to the output ports

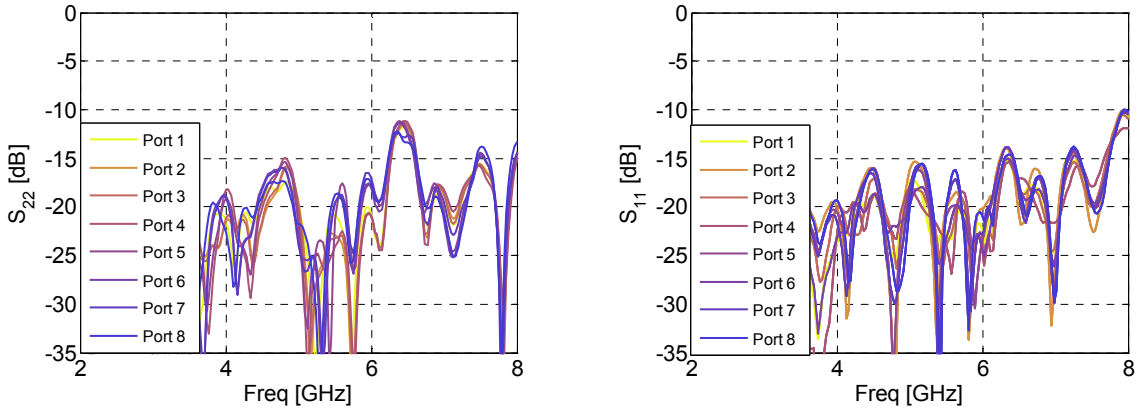

Figure 5-18 Reflection coefficient of the input and output ports

The transmission coefficients, relating the input with the output ports, are plotted in Figure 5-17 They vary between -10dB and -13dB in the range between 4 and 6GHz. Outside this range the coupling coefficients spread as expected due to the limited bandwidth of the directional couplers employed. Despite the increasing spread, one can still distinguish the beams of the array factor in Figure 5-19, where the frequency range is extended to 3 and 7GHz. The SLL deteriorates, except for the outermost beams, to a level of -9dB.

The working bandwidth can be extended from 40% bandwidth at 5GHz to 80% accounting for the degradations drawn in Figure 5-19. The Butler matrix maintains beam directions and directivity.

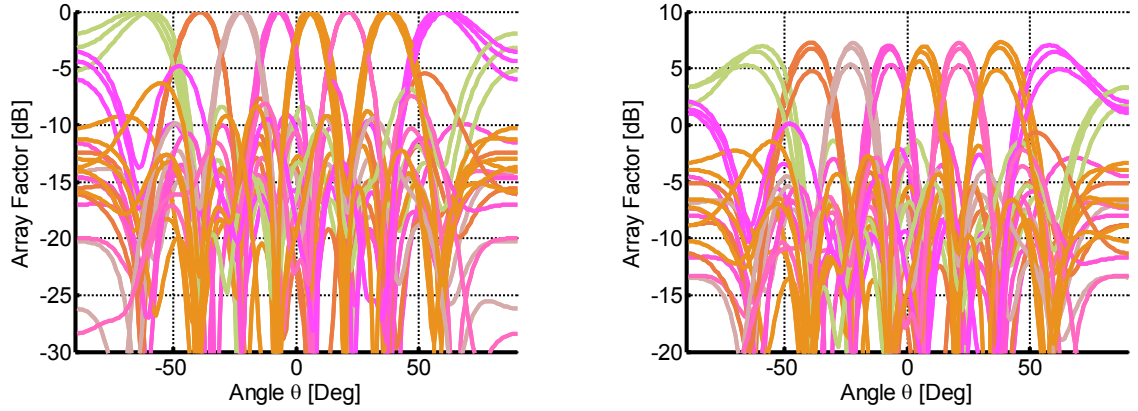

Figure 5-19 Measured normalized/not normalized array factors at 3,5 and 7GHz

The measured data validate the design process where all components (broadside coupler, transitions and crossings) were simulated and optimized separately before integration. The LTCC technology offers new ways to integrate this matrix in a five-layer *DuPont 951*-mixed tape process. A very good agreement between simulation and measurement is observed. This technology opens new opportunities for realization of compact matrices of higher order. This will be underlined in the next chapter based on a folded matrix realized using 40 layers of LTCC tape.

Chapter 6

A novel folded modular Butler matrix based on LTCC

Abstract - This chapter describes the realization of an 8x8 Butler matrix taking full advantage of the 3D packaging capability of LTCC. The novelty of the design lies in the folding and stacking of phase shifters and couplers on 40 layers of LTCC tape to reduce the lateral dimensions of the previously described 5GHz Butler matrix. The size is reduced to less than 1/5 of the original design. Furthermore, the new LTCC realization allows modular extension of Butler matrices to multiples of 8x8.

6.1 Introduction

In Chapter 5 the integration of an 8x8 Butler matrix at 5GHz is shown for the first time in LTCC using new stripline crossings and broadside couplers. Only a few layers of the LTCC tape were used and the full potential for 3D integration has not been utilized. The size of the first Butler matrix together with the interconnecting lines is defined by the maximum standard wafer size of 100x100mm^2.

In this chapter, we introduce several novel design ideas to allow folding and stacking Butler matrix elements, which will lead to a significant size reduction, offer modularization of Butler matrices, and at the same time, maintain excellent electrical performance. In this new design, we use the *Ferro A6-S* LTCC tape system with 40 layers. The matrix incorporates compensated phase shifters and broadband couplers to achieve a 40% bandwidth at 5 GHz, resulting in the smallest size Butler matrix ever reported at this frequency.

6.2 The modular Butler matrix design

All practical 2D realizations reported in the literature to date as well as the one proposed in Chapter 5 offer a limited solution to the crossing problem. In order to overcome this limitation, this chapter introduces a novel folding procedure. In Figure 6-1 the folding is coded with three different colors and can be followed by the numbering given in the figure. In step 1, two blocks of couplers are overlaid. This is the principal step leading to the modularization of the Butler matrix. The resulting submodules are illustrated in Figure 6-2.

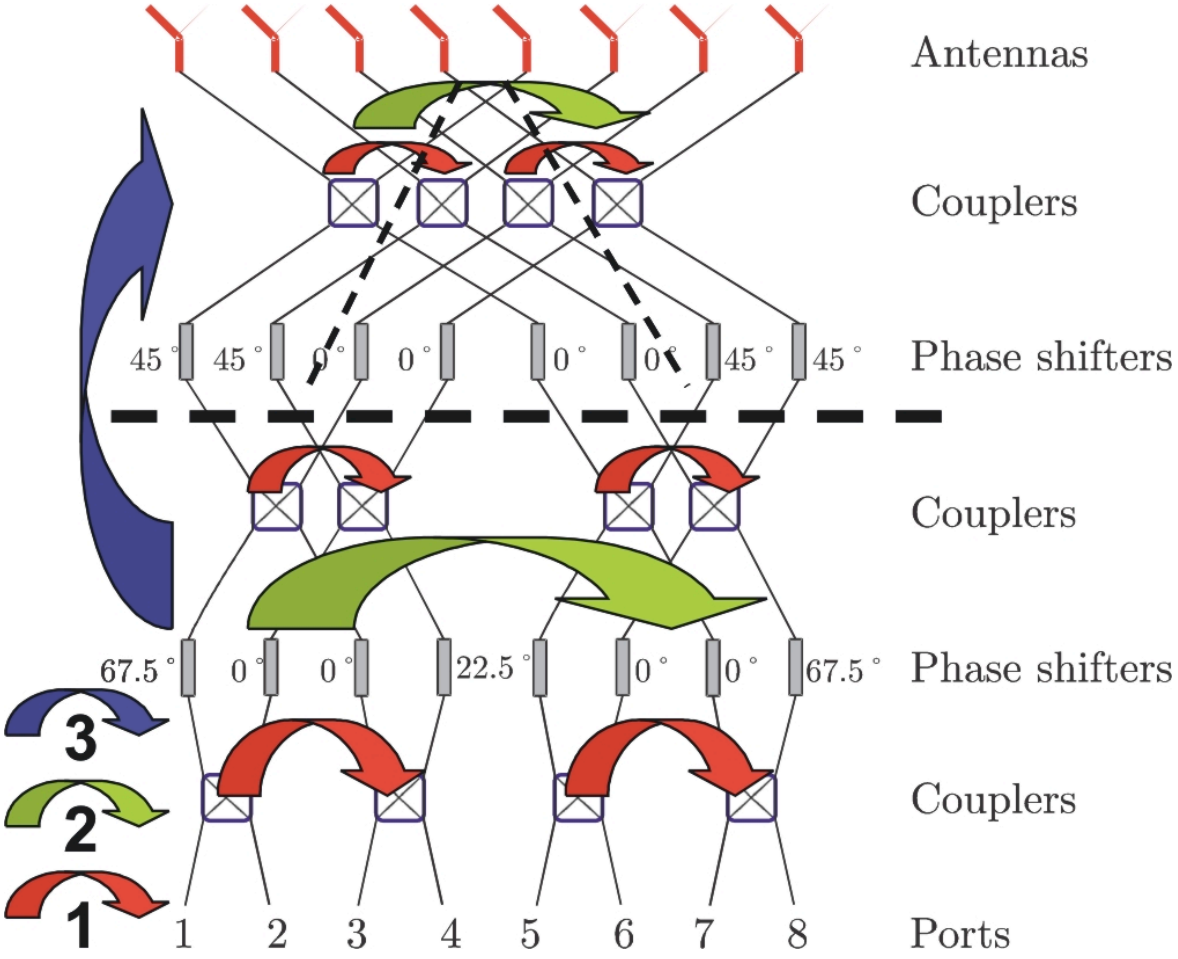

Figure 6-1 Block diagram of the 8x8 Butler matrix in LTCC including the 3 folding steps coded with 3 different colors

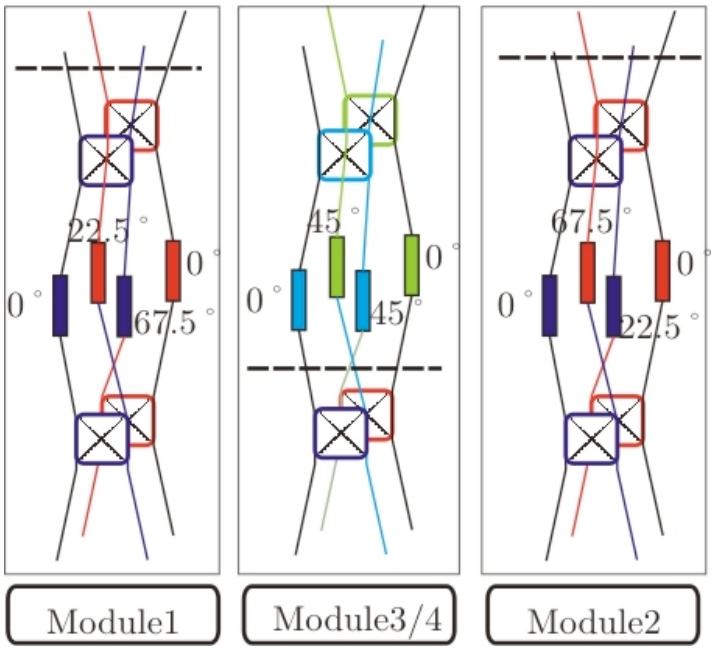

Figure 6-2 Submodules of the Butler matrix after first folding step

The separate modules have to be seen as independent building blocks, which can be used for any higher-order Butler matrix. These modules can only be realized with a multilayer approach, where two overlaid couplers can be build on separate striplines (accounted as two different levels).
Each of these modules includes two serially connected couplers per level. One branch of every coupler can be connected via a zero phase path.

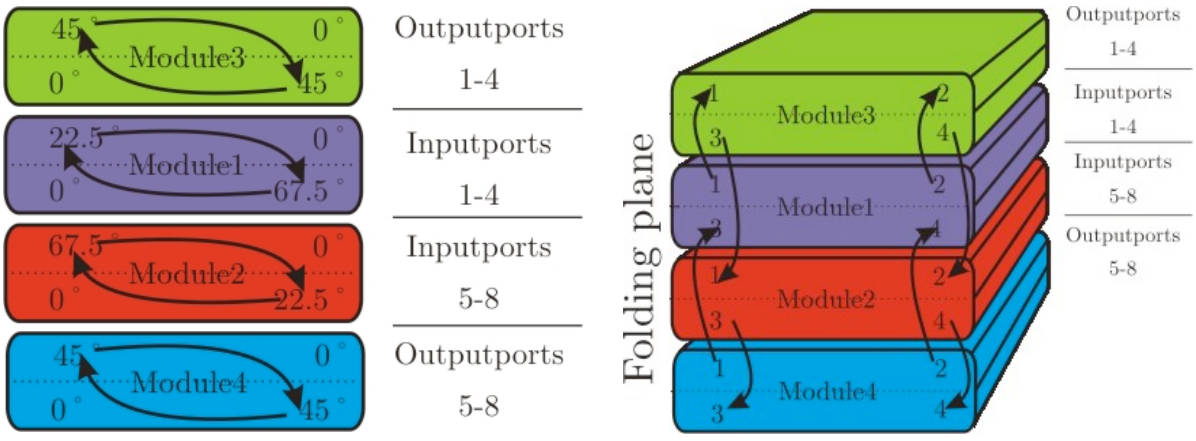

Figure 6-3 Stacking of the 4 sub modules of the 8x8 Butler matrix after the first folding step and interconnection of the 4 sub modules in the third folding step.

The second branch of the coupler connects directly to the specific phase shifter, which is connected to the coupler on the other level, as visualized in Figure 6-3. The crossings in the previous 2D layout translate into a simple crossing of two levels, thus avoiding geometrical conflicts. This is the principal key in breaking the limitation of higher-order Butler matrices due to an increase of the number of geometrically possible crossings.

In the next folding step, sub modules 1 and 2(corresponds to the input) are brought on top of each other as sketched in Figure 6-3. Modules 3 and 4(corresponds to the output) have symmetrical phase shifters and therefore are identical. They are attached to the modules 1 and 2 in the last folding step. This folding step is carried out along the thick vertical line drawn in Figure 6-1 as well as in Figure 6-2. Figure 6-3 shows the interconnection of the four submodules following the signal routing from the input ports to the output ports. This third folding is the second key step used to overcome and translate all signal crossings into transitions between layers of striplines and between different sub modules.

6.3 Implementation of the matrix in LTCC

Wideband couplers and phase shifters required for the folded Butler matrix will be discussed in the following part. The performance of any Butler matrix depends critically on the bandwidth of the 3dB coupler and the constant phase shifters, as already discussed in the Chapter 5. A tandem broadside coupler is chosen for the coupler. The phase shifter is a bandpass filter with dispersive phase.

Hybrid coupler

The stripline technology used in this design is based on a characteristic line impedance of 50Ω with 5 layers of *Ferro AS6-S* material with $\varepsilon_r = 5.9$ and a tape thickness of 96.25μm (post-fired) for every stripline.

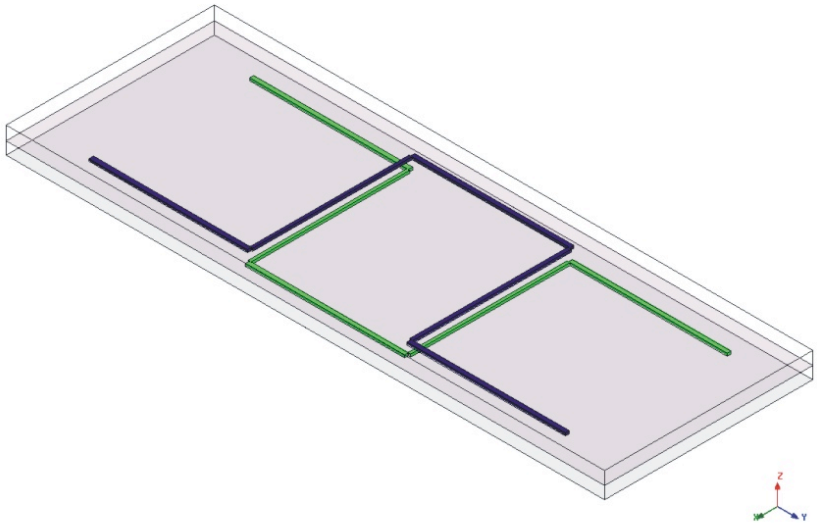

Figure 6-4 Coupled–line hybrid

A tandem hybrid with offset coupled lines is selected for the implementation of the coupler[45]. The authors in [46] propose this tandem coupled-line hybrid, which compensates for the displacement errors. This coupler is able to meet the bandwidth requirements (60% BW@5GHz), the characteristic line impedance (50Ω) and, at the same time, is less sensitive to the manufacturing tolerance inherent to the LTCC process.
Figure 6-4 shows the configuration of the tandem hybrid coupler. Each of the coupled lines achieve 8.34dB coupling. The two couplers are connected in tandem for 3dB coupling. The strip conductors of the two couplers are designed to shift in opposite directions if a vertical misalignment of the 40 layers occurs. The deviation in the coupling characteristics can therefore be reduced by this configuration. By additionally enclosing the coupling sections by vias, one can also reduce the dependence of the coupling on the thickness of the intermediate layers as shown in [46].

The characteristic impedance and the coupling coefficient of the sections are optimized by adjusting the widths of the lines and modifying the transversal shift of the lines. The optimization leads to the thickness of one layer of the material between the coupled lines. Overall, five layers are used to meet the requirements. These five layers add up to a thickness of 480µm and correspond to one level specified in the description of the submodules.

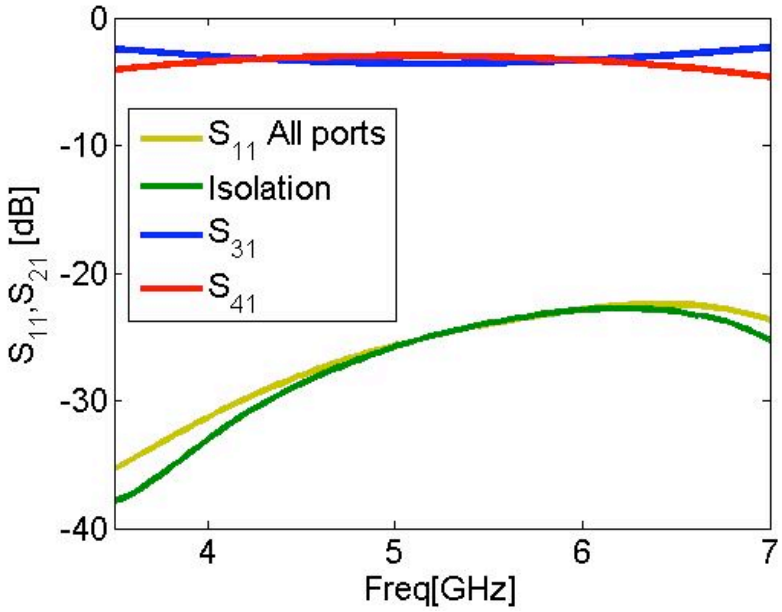

Figure 6-5 Simulation results for the transmission, isolation and return loss of the coupled-line hybrid

The simulation results plotted in Figure 6-5 show that both transmission parameters S_{31} and S_{41} have values close to -3dB over the frequency range between 3.5GHz and 6.5GHz. The transmission to the isolated port and the input reflection coefficient do not exceed the -25dB level in the frequency range of interest.

Phase shifter

In order to achieve broadband operation of the phase shifters, the approach of coupled transmission lines is usually employed. One of the first designs that used the coupled-lines method to construct broadband phase shifters is the Schiffman differential phase shifter [47]. It consists of two transmission lines: the reference transmission line and the folded edge-coupled section. By properly selecting the length of these lines and the degree of coupling, the phase difference between them can be kept constant at 90 degrees over a wide band. The miniaturization of the relatively large Schiffman phase shifter was presented in [48]. It has the drawback of reducing the bandwidth. A second drawback is the reduced line width of the Schiffman phase shifter in

stripline for low phase values. The first paper to report on a wideband Butler matrix was published in [49] including the Schiffman lines as phase shifters. The bandwidth reported there is limited by the smallest-valued phase shifter and is 26%. The search for a more appropriate broadband phase shifter led to the network type phase shifter proposed by [50]. In the last years, an increasing number of phase shifters for ultra-wideband (UWB) applications were presented. A feasible alternative to the phase shifter chosen in this design is the UWB phase shifters based on coupling slots in an ground plane as described in [51]. The paper gives also a good overview of the field of broadband phase shifters.

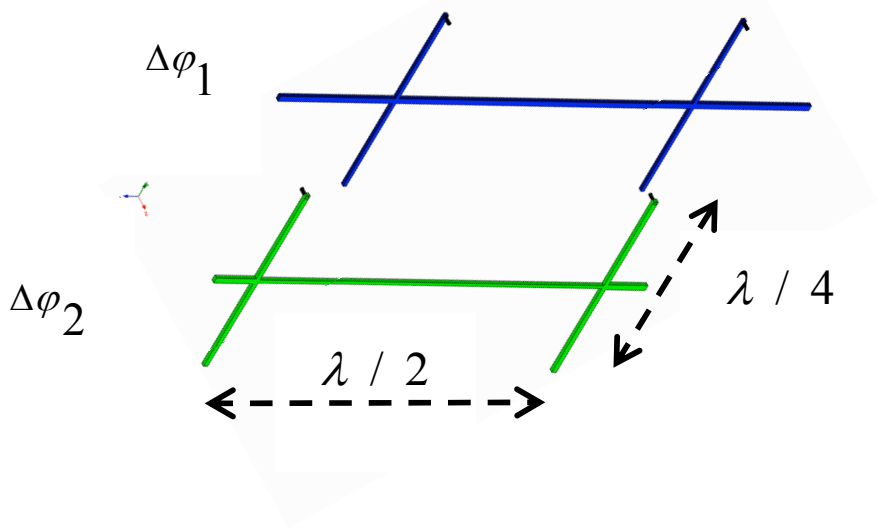

Figure 6-6 Structures of the network-type phase shifters

The phase shifters used for the matrix are based on the bandpass phase shifter introduced in [50] and illustrated in Figure 6-6. The network consists of a main line of length $\lambda/2$ terminated by four $\lambda/8$ parallel open and short stubs. One can control the phase slope using the characteristic impedance and the length of the different sections. The authors in [50] proposed these two bandpass networks especially for lower constant phase differences below 90 degrees. Larger constant phase differences are achieved if one of the branches is of a bandpass type, as described above, and the other is a simple transmission line. Together, the phase shifters are referred of class I and II and provides a set of shifters, which can easily be incorporated into any stripline circuit.

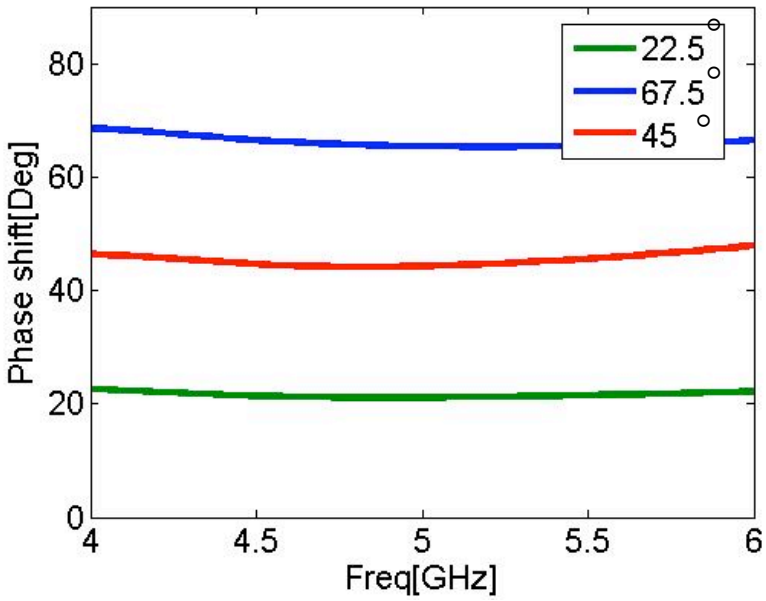

Figure 6-7 Simulation results for the phase of the shifter

The designed phase-shifting networks are impedance matched and show a minimum phase deviation over a broad bandwidth. The phase difference is constant and matched for 50% BW@5GHz as Figure 6-7 illustrates.
Figure 6-8 shows the return loss and transmission coefficients of the separate networks, and one can see that the bandwidth of 2.5GHz at 5GHz is again ensured.

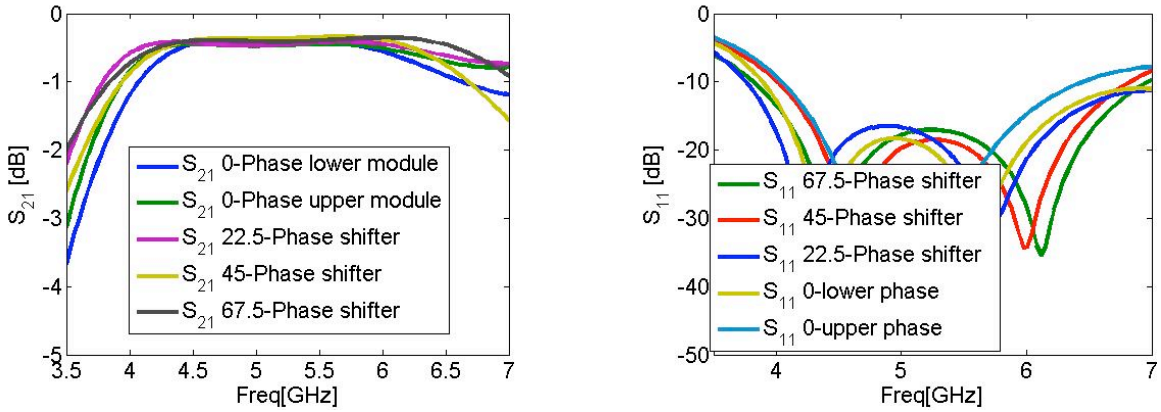

Figure 6-8 Simulation results for the transmission, isolation and return loss of the phase shifters

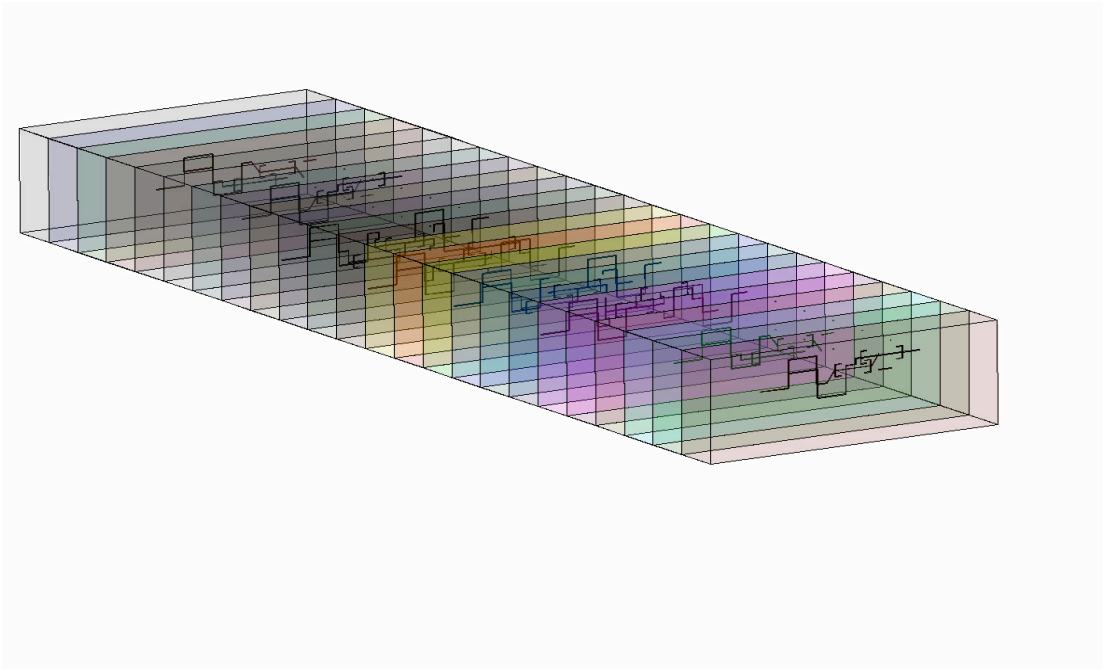

Figure 6-9 Placement of all the components on the 40 layers

The network-type phase shifters provide three constant relative phase differences. The complexity in using them comes from the geometrical placement within the matrix. The positioning of the coupler requires the same geometrical connection points for the different lengths of the phase shifter. A careful staggering avoids additional transmission lines and solves the issue.
With the designed couplers and phase shifters distributed over 40 layers as drawn in Figure 6-9, an elaborated wiring of the components has to be done. The extremely high number of transitions through ground planes requires a careful design. A zoom into two stripline layers with the specific interconnects can be seen in Figure 6-10.

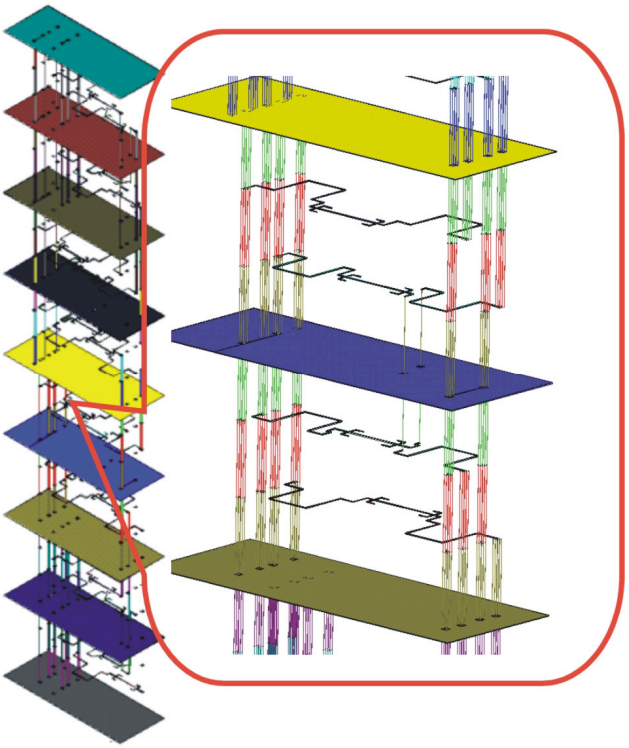

Figure 6-10 Zoom into the structure of the 40 layer folded Butler matrix

The overall structure is too complex for the majority of numerical simulation tools available and has therefore to be realized and measured in order to be validated. The results of the measurements will be presented in the next section.

6.4 Measurement results of the folded matrix

The complete structure of the LTCC matrix is pictured in Figure 6-11. The size of the Butler matrix is 15mm by 35mm within the LTCC substrate of 18mm by 48mm. The thickness of the 40 layers of tape is 4mm. In Figure 6-11 eight openings in the upper ground plane can be seen. In the middle of each opening is placed a via carrying the signal from the striplines. The other eight ports are located on the lower ground plane.

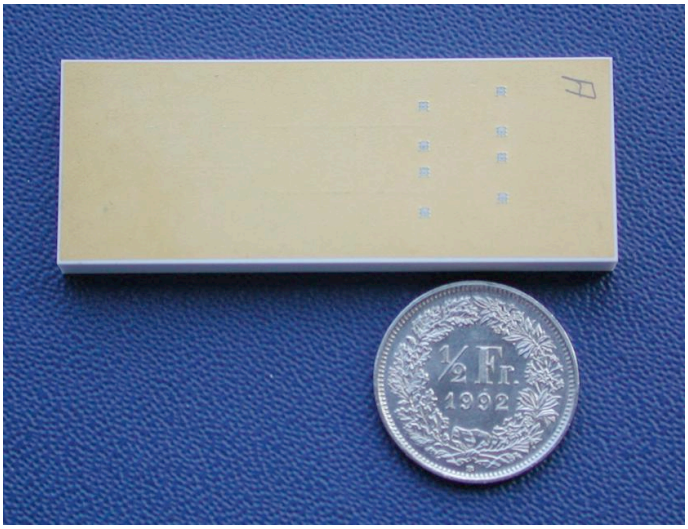

Figure 6-11 Picture of the 40 layer LTCC Butler matrix

In Figure 6-12 the measurement setup for connecting all ports is pictured. The LTCC chip is sandwiched between two soft substrates. The signal line from the LTCC board is connected to a microstrip line trough a slot in the ground plane of the substrate.

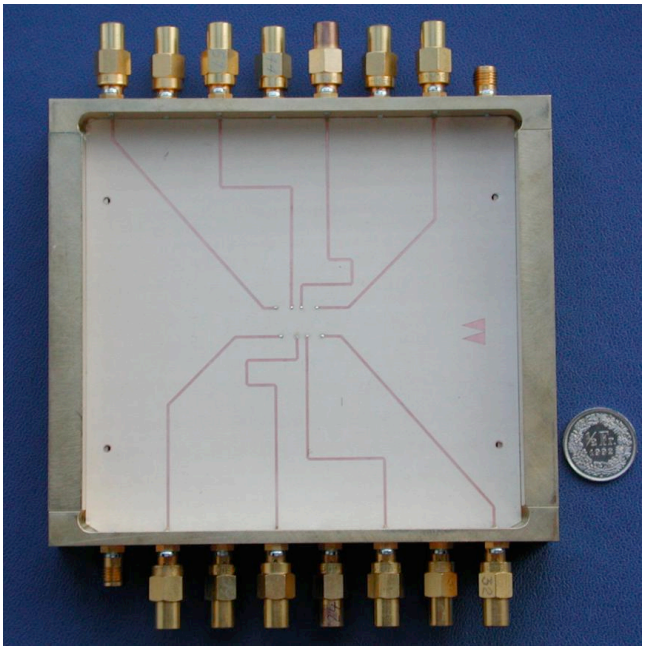

Figure 6-12 Measurements setup needed for interconnecting the LTCC chip

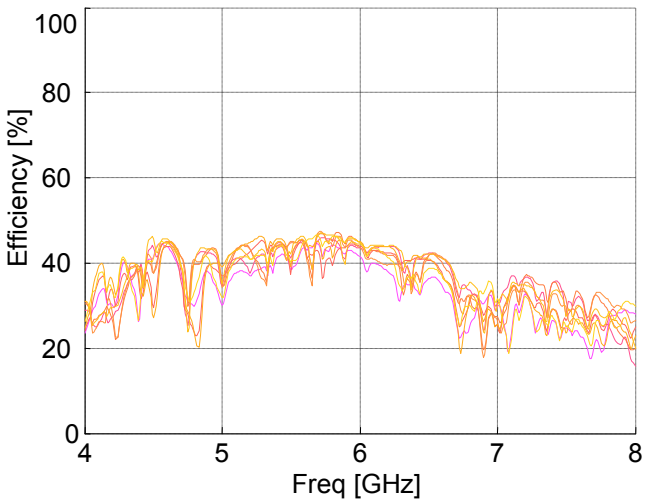

Figure 6-13 Efficiency of the measured 40 layer Butler matrix

The efficiency calculated from the transmission of the j-th input port to the output ports is defined by (5.1) and has been plotted over frequency in Figure 6-13. The efficiency drops at higher frequencies as loss increases. Additionally the bandpass characteristics of the phase shifters can be seen at lower frequencies. In the frequency range of operation from 4GHz to 6GHz, the efficiency stays above 30%-40%.
The smaller efficiency compared to the previous LTCC matrix in Chapter 5 originates from additional losses. The larger dimensions of the coupler and the phase shifters, the higher number of interconnections as well as the different measurement setup are the source of these losses.

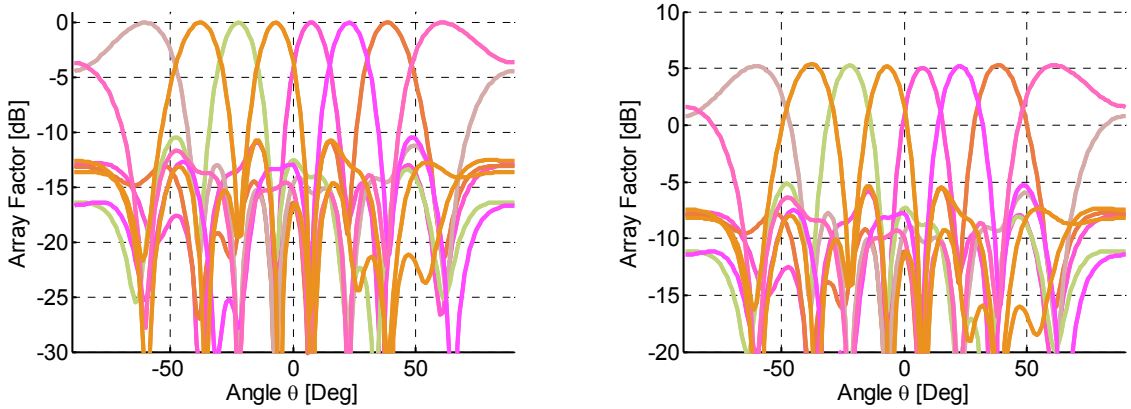

Figure 6-14 Array factor at the central frequency of 5.7GHz (normalized versus not normalized)

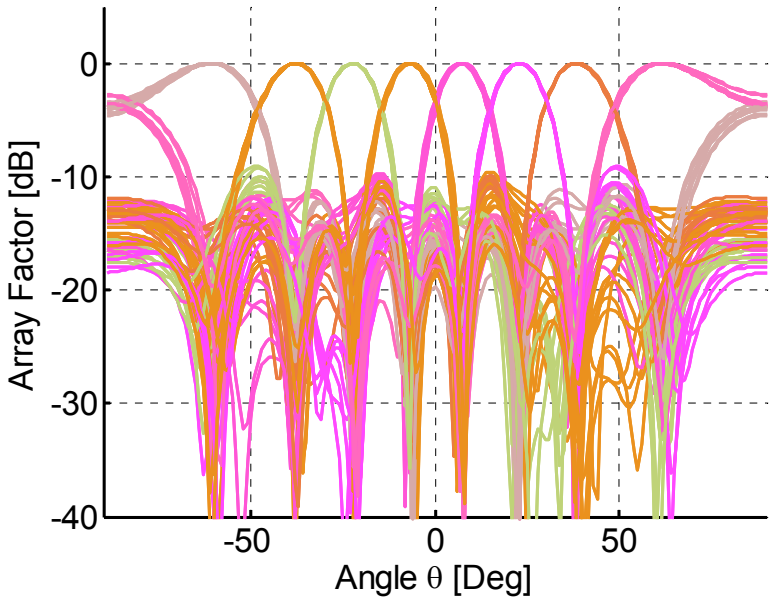

Figure 6-15 Array factors at 10 different frequency points in the range [4.8GHz-6.6GHz] obtained from the measured data

An additional size reduction of the components as well as additional optimization of the transition would bring the two designs to a similar efficiency level.
The measured data shows a frequency upshift of 0.9GHz, which was found to be related to a change in thickness of the processed substrates. In Figure 6-14 and Figure 6-15 one can distinguish the separate eight beams corresponding to the active input ports. The SLLs stays below -11dB over a bandwidth of 1.8GHz around the center frequency of 5.7GHz.
The good measurement values for SLL and the input matching in Figure 6-16 validate the ultra compact design. Over the frequency range 4.8 GHz-6.6 GHz, the beam directions of the main lobes do not exhibit any variation from the desired pointing direction. This can clearly be seen in Figure 6-15, where each beam was plotted at 10 different frequency points in the given frequency interval.
The measured return loss, shown in Figure 6-16, remains below 10dB for the entire measurement range from 4GHz to 8GHz. The transmission coefficients in Figure 6-16 vary between -10dB and -16dB in the range between 4.8 and 6.6GHz. The transmission coefficients differ in terms of smoothness compared with the Butler matrix measurement in Chapter 5. The rippling seen in the transmission coefficients relate to an increased leakage due to missing via fences. The via fence enclosure was excluded in the first run

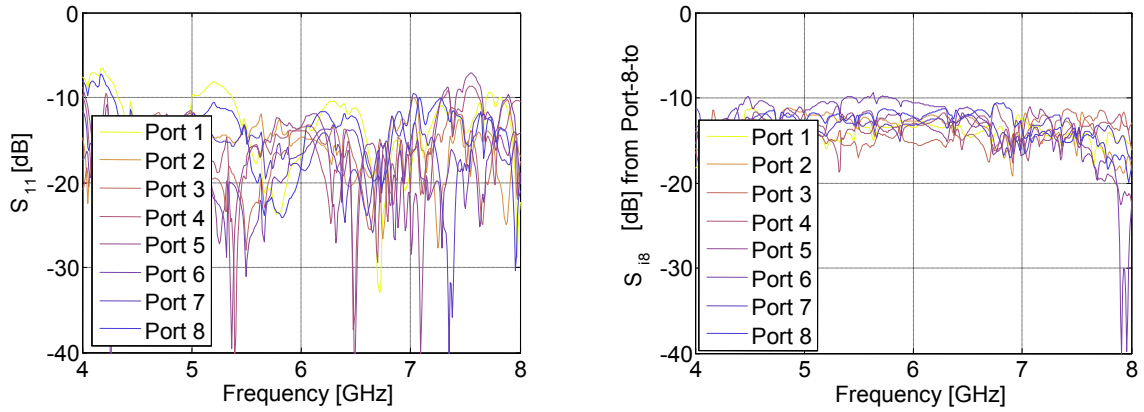

Figure 6-16 Measured reflection and transmission coefficients of the modular Butler matrix

because of the increased technological effort required. In order to reduce this leakage a design with a complete shielding of the striplines is needed.

Outside the 4.8GHz-6.6GHz range the transmission coefficients decrease slowly as expected due to the limited bandwidth of the phase shifters. Despite the bandwidth limitation one can still clearly distinguish the beams of the array factor in Figure 6-17, where the frequency range is extended to 4.5GHz-7.5GHz and in Figure 6-18, where the entire range from 4GHz-7.9GHz is considered.

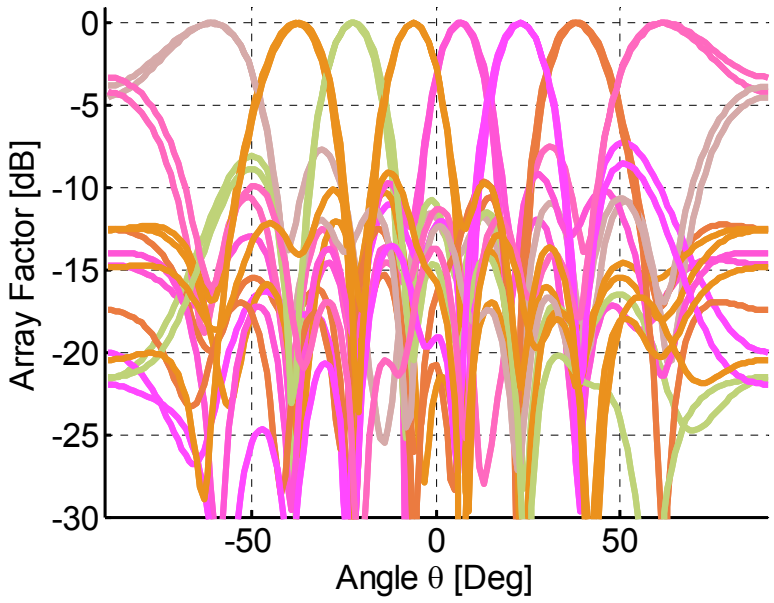

Figure 6-17 Array factor at 4.5GHz and 7.5 GHz spanning 3 GHz BW

The SLL deteriorates for all the beams to a maximum of -8dB in the entire frequency range. Over a bandwidth of 70% at 5.7GHz a relative small degradations of the SLL and a beam squinting below one degree as seen in Figure 6-18, were registered.

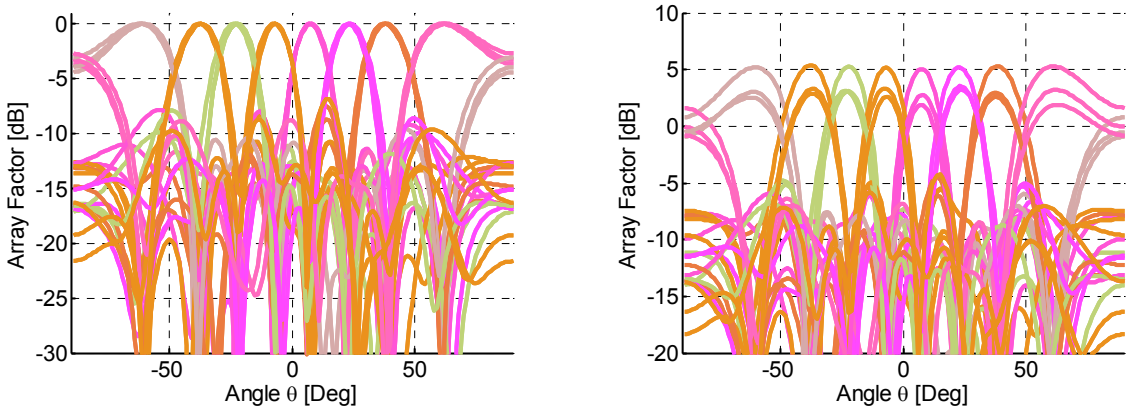

Figure 6-18 Array factor at 4 GHz, 5.7GHz and 7.9 GHz spanning 3.9 GHz bandwidth (normalized/un-normalized)

The modular Butler matrix maintains the beam directions and directivity in the entire design frequency range. Thus, a new modular 8x8 LTCC Butler matrix has been designed, realized, and measured. The principle of modular Butler matrix design is introduced. All subcomponents were simulated only and tested in the final system configuration. The LTCC technology proved to be capable of integrating this matrix in a 40-layer *Ferro AS6-S* tape process. The measurements confirm the validity of the approach.
The tremendous size reduction coupled with new ways of interconnecting the separate submodules makes the higher order Butler matrix for the first time attractive for highly integrated applications.
The improvements for the lower frequency bands were discussed in the previous chapter, in the next one the operating frequency will be shifted to 60GHz.

Chapter 7

60 GHz Butler matrix

Abstract - This chapter describes the realization of an 8x8 Butler matrix taking advantage of the via fence wave guiding in LTCC as well as of the 3D packaging capability at very high frequencies. This design is the first to be reported at 60 GHz matrix in the standard LTCC tape process. The dimensions of the new Butler matrix scale down with increasing frequency maintaining the beamforming capabilities over a wide bandwidth.

7.1 Introduction

The focus of Chapter 6 was on the design of more compact, integrated Butler matrices. The achieved size reduction and the high bandwidth reported make them suitable for high-capacity communication systems at lower frequencies. Another approach for increasing the capacity of a communication system is the use of the V-band frequency range. from 40 to 75 GHz. The licensing authorities have allocated a frequency of 60 GHz for unlicensed, point-to-point, fixed, wireless systems and indoor communications. These systems are primarily used for high-capacity (multi-gigabit), short distance communications.
The reported beamforming networks for high frequencies are limited to the lens type and optical solutions such as those described in [52],[53], and [54]. The last approach uses a photonic beamformer to control a 60 GHz phased array. Optical heterodyning the waves of two laser diodes generates the 60 GHz signals. The drawback is the increased complexity compared to the lens and the matrix beamformers. The gain achieved by an array of four patch antennas, is reported in [54] to be -5dB. Taking into account the gain of each patch antenna, the gain of the four-port beam-forming network is derived as -10dB.

In this chapter, a Butler matrix of order eight is designed for the center frequency of 60 GHz using LTCC. The matrix will prove that integrated passive beamforming using Butler matrices can be realized also at high frequencies. Integrating this matrix in a well-established LTCC technology makes the interconnections with the active circuit MMICs (Monolithic Microwave Integrated Circuits) technologically straightforward.

7.2 LTCC implementation of the 60 GHz Butler matrix

The structure of the realized 8x8 Butler matrix is sketched in Figure 7-4. The Butler matrix is designed using stripline technology. The substrate is made of only two layers of *Ferro AS6-S* material with $\varepsilon_r = 5.9$ and a tape thickness of 192µm (post-fired). The layer stack can be seen in the cross section drawn on the rights side of Figure 7-1. The number of layers required is four. The upper two layers are used for signal-line crossing as seen in Figure 7-1 from the different color-coding of the striplines and substrates.
The additional two layers do help in the simplest way to overcome again the strongest limitation.

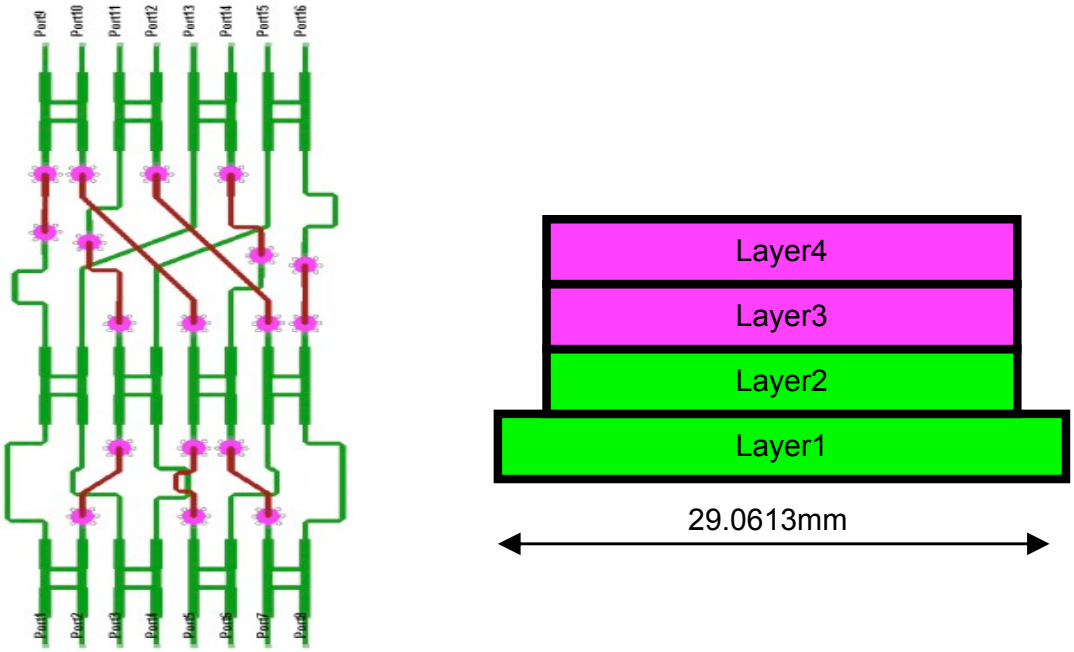

Figure 7-1 Schematic and vertical layer stack for the 8 by 8 Butler matrix at 60 GHz

7.3 Results of the 60 GHz Butler matrix

Branch-line coupler

The branch line coupler is implemented in stripline. This type of quadrature coupler implemented using quarter-wave transmission lines is described in [37] and can be best analyzed by the even-odd mode decomposition. The geometry of the branch-line coupler is shown in Figure 7-2. Two main transmission lines shunt-connected make a branch-line. As it can be seen from the figure, the coupler is symmetric and therefore even/odd mode analysis can be employed.
Riblet proposed additional stubs to achieve a higher bandwidth and a flat coupling characteristic in [55]. This can be achieved with quarter-wavelength transformers attached to all of the ports. Another quarter wavelength short-circuited stub should shunt them. In this design, we use only the quarter wave transformer to match the branch-line coupler to the 50Ω impedance level of the stripline. The size limitation of the entire Butler matrix drawn in Figure 7-4 excludes the use of additional stubs.
The results of the full-wave simulation using *HFSS* [27] can be seen in Figure 7-3. Both transmission coefficients have values close to -3dB in the frequency range between 55GHz and 65GHz. The isolation of the ports and the input reflection coefficient have values below -15dB in the same frequency range.

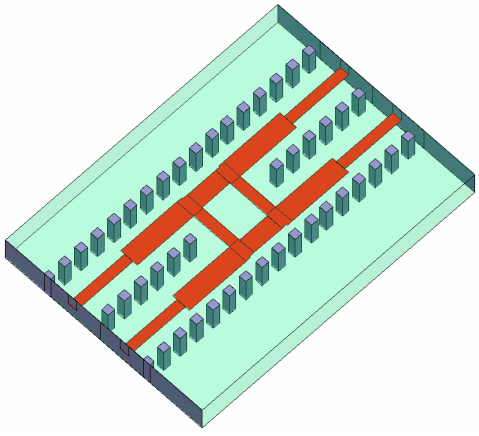

Figure 7-2 Branch-line hybrid coupler

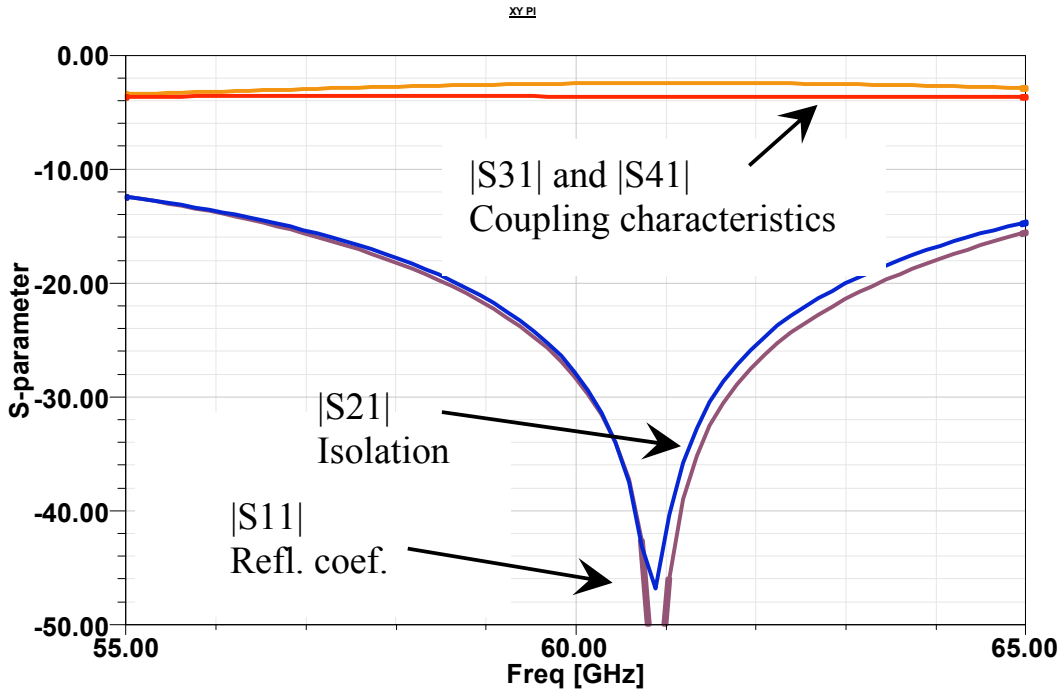

Figure 7-3 Isolation and reflection coefficients of the coupler

This isolation is only achievable by means of via fences along the transmission lines as seen in Figure 7-2. The mode conversion to a parallel-plate one is also suppressed by the via fence.

Simulation results of the Butler matrix at 60 GHz

The considered bandwidth of 10GHz at 60GHz corresponds to 17% relative bandwidth. Therefore, the phase shifters were build as meandered lines. Since the transitions are an important part of the phase shifter, they have to be included in the design and optimization processes for a good return loss and accurate phase relation. All the parts are combined in the matrix in Figure 7-4.

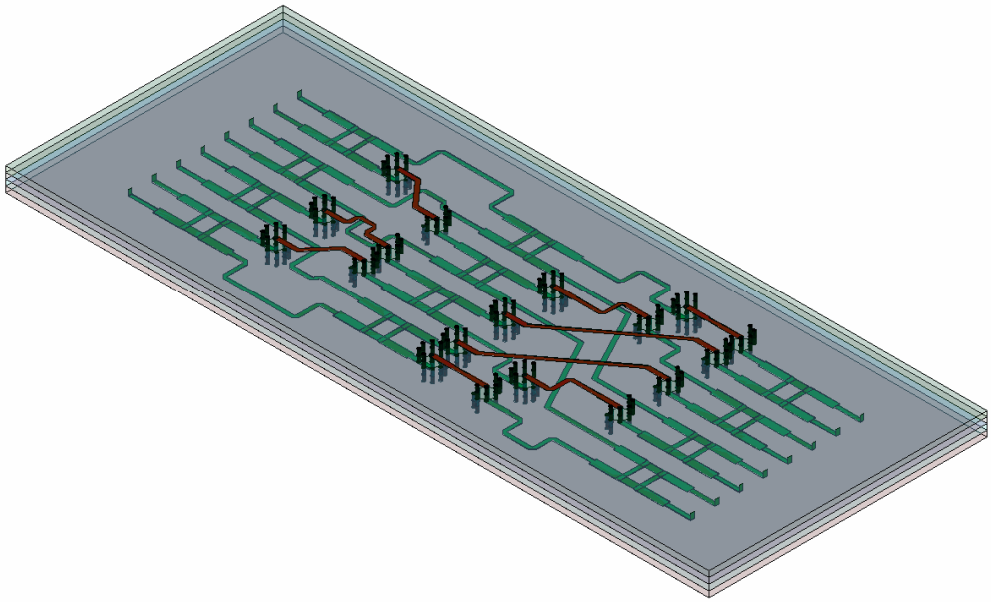

Figure 7-4 Structure of the 60 GHz Butler matrix

The entire Butler matrix was simulated using *HFSS* and *Designer*. The simulation in *HFSS* reaches the memory limit of the simulation tool (500-thousand tetrahedral mesh cells) accounting only for the striplines, not including the vias. In Figure 7-5, the array factor of the Butler matrix is drawn and the current density on the middle ground plane is plotted. Again, a strong standing wave from top to bottom is encountered and, as one can see, the array factor is far from the array factor of the ideal Butler matrix. The simulation of the complete system in *HFSS* proved once more to be extremely difficult but nevertheless important, providing information about the standing waves. The striplines shielding by means of vias is therefore necessary not only for reducing the cross talk of the extremely small matrix but also for excluding the parasitic resonances.

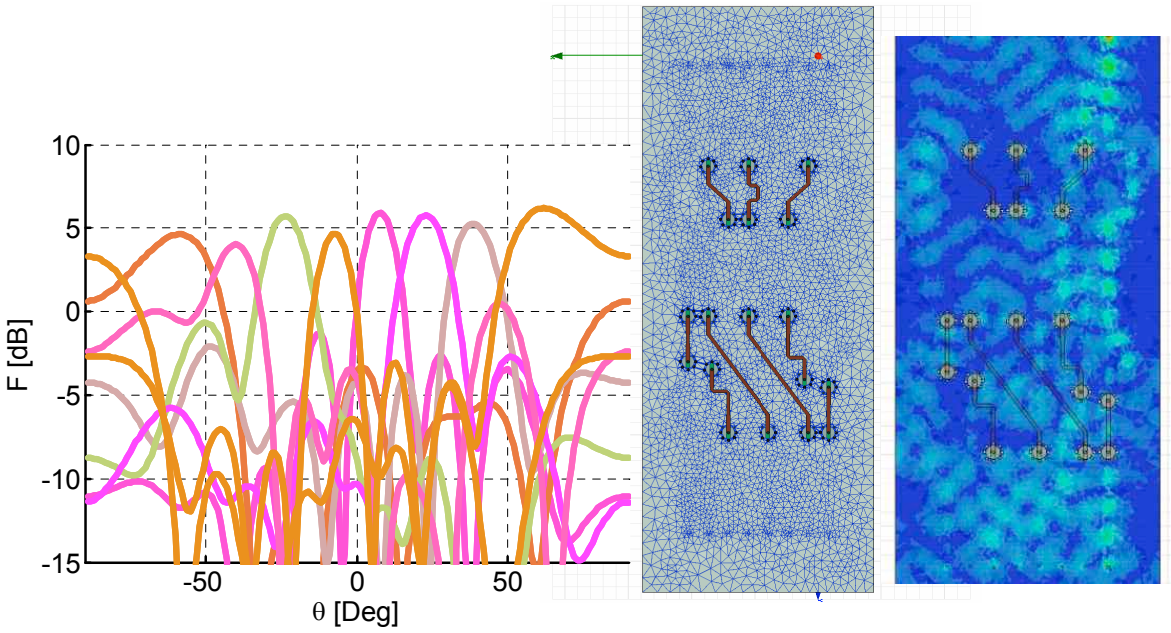

Figure 7-5 Simulation of Butler matrix without vias in HFSS: Array factor, mesh plot, and current distribution

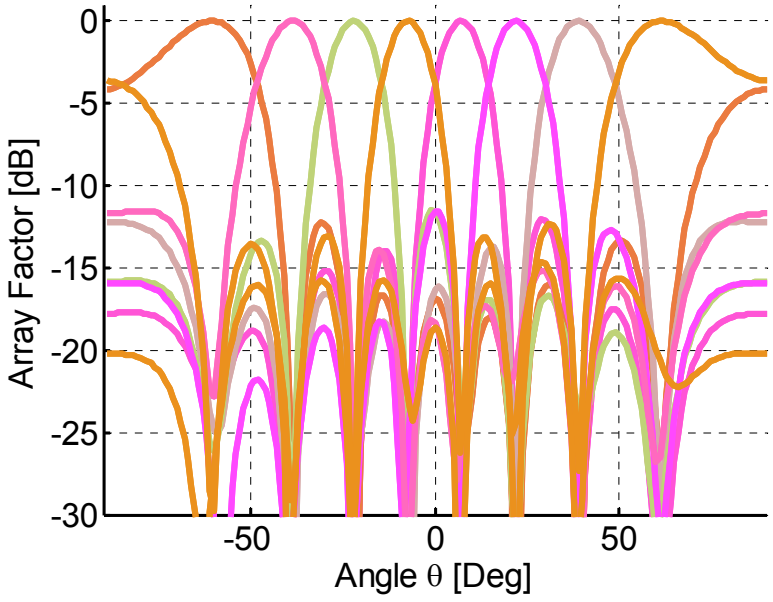

Figure 7-6 Array factor of the simulation results at 60GHz

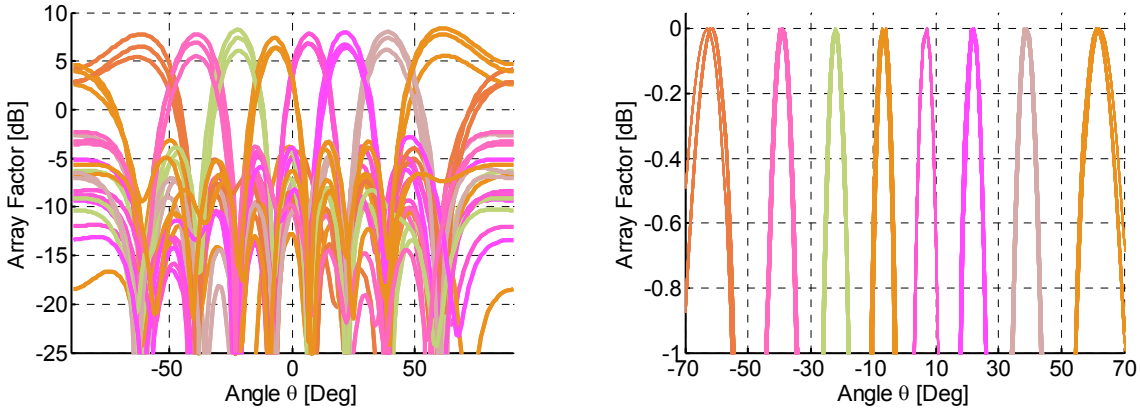

Figure 7-7 Array factor of the simulation results at 55GHz, 60GHz and 65GHz (not normalized/normalized)

Figure 7-6 and Figure 7-7 contain the array factor obtained from the simulation with *Designer*. The SLL is below -12dB for the center frequency and remains below -10dB over a bandwidth of 10GHz around the center frequency of 60GHz. The simulated beam directions and beamwidths are in excellent agreement with the desired values.

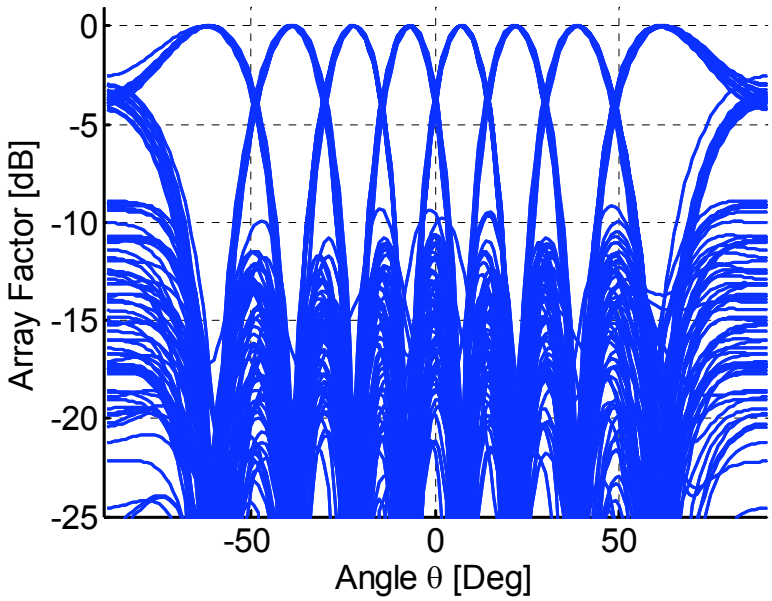

Figure 7-8 Array factor of the simulation results at 10 frequency points in the range 55GHz-65GHz

In the frequency range between 55GHz and 65GHz, the beam directions of the main lobes exhibit a maximum variation of ±2° from the desired value at

the outer beam as seen in Figure 7-7 and in Figure 7-8. Figure 7-8 shows 10 additional patterns to ensure that the behavior is maintained over the entire frequency range from 55GHz to 65GHz. The matrix realization using *Ferro AS6-S* material is the last part of the concept proof.

Measurement setup and results of the 60 GHz Butler matrix

In order to experimentally characterize the matrix structure, a microstrip setup is required and transitions from stripline to microstrip are needed. Figure 7-9 shows the transition from stripline to microstrip in LTCC, including a ribbon bond to the second microstrip line on the Durroid substrate ($\varepsilon_r = 5.9$ and tape thicknesses of 127µm). The microstrip on the LTCC uses a step between the first and the next three substrates as seen in the longitudinal cross section of Figure 7-1. To have one substrate of thickness 192µm protruding from the rest of the board by 400µm is a manufacturing challenge. The transition including the ribbon bond and an air gap of maximum 150µm was optimized as a hole. The resulting reflection coefficient is plotted in Figure 7-9. The transition is optimized to not exceed the level of -30dB for the reflection coefficients. The very small size of the matrix requires also to decouple the closely spaced ports. The optimized isolation stays below -28dB. Time gating allows eliminating the response of the transition. This yields a return loss higher than 25dB.

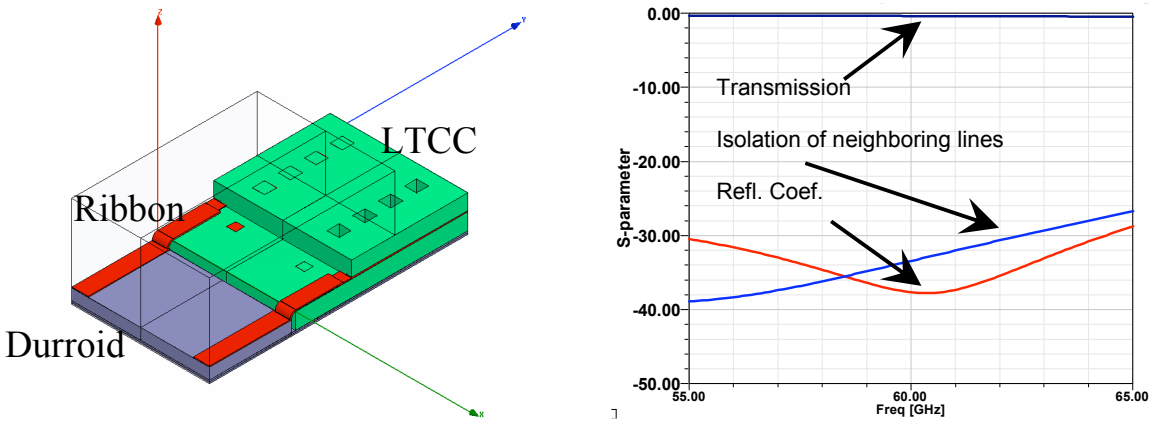

Figure 7-9 Transition from the LTCC stripline to a microstrip on a soft substrate showing two neighboring input lines(red)

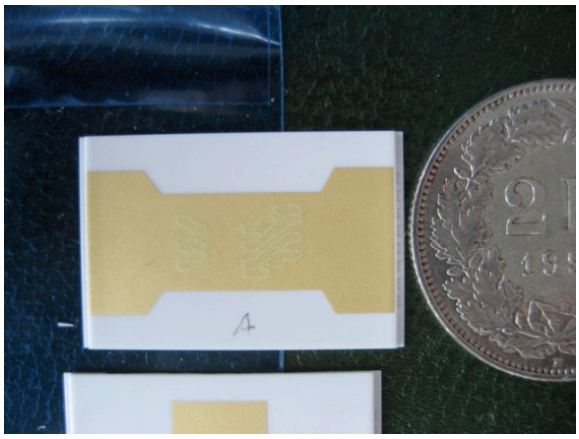

Figure 7-10 Realized Butler matrix in LTCC at 60GHz

The complete structure of the LTCC matrix is pictured in Figure 7-10. The matrix together with the measurement board can be seen in Figure 7-11. V-connectors are used to connect the measurement board to a vector network analyzer. All ports have to be connected simultaneously to a matched load and therefore a probe-tip measurements setup cannot be considered.

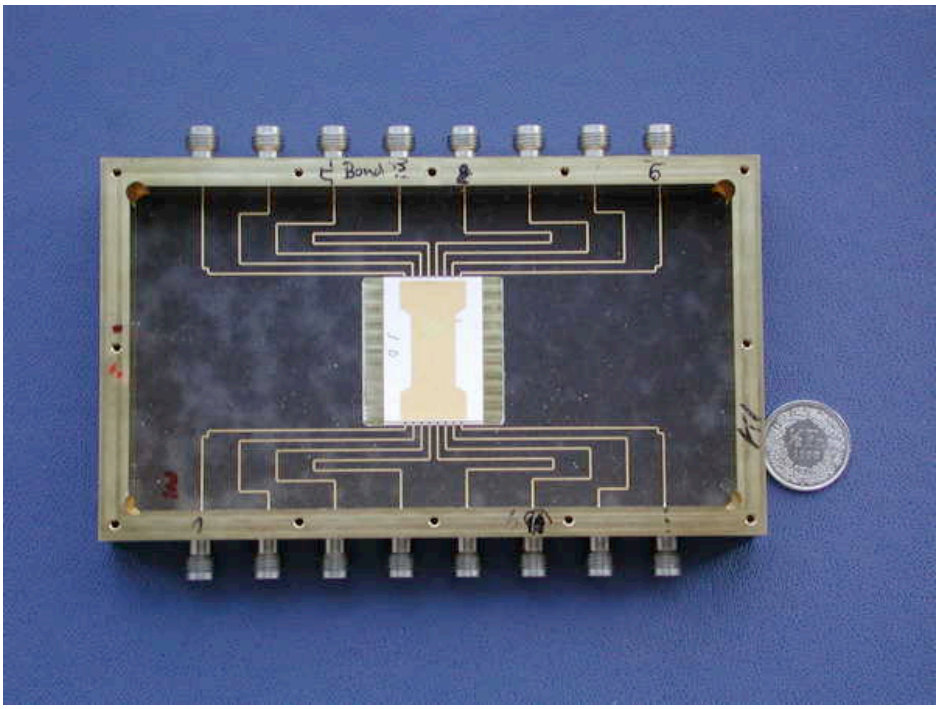

Figure 7-11 60GHz Butler matrix including measurement gear

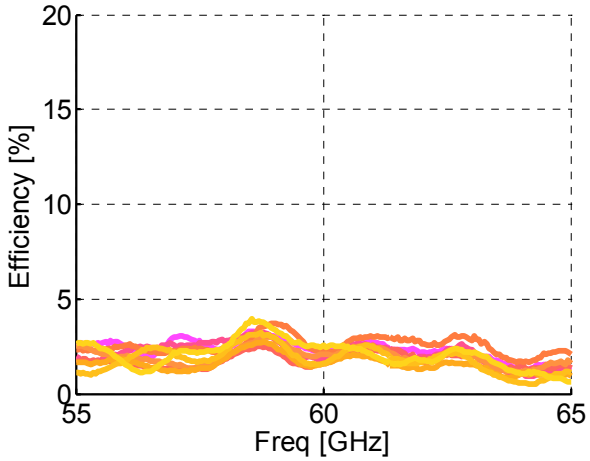

Figure 7-12 Efficiency of the 60GHz Butler matrix together with the measurement gear

The large Duroid substrate with its long equiphase lines connecting the Butler matrix, the V-connectors, and the transition add losses in the range of 8dB to the overall Butler performance and efficiency.
The efficiency as defined by (5.1) is plotted versus frequency in Figure 7-12. In the frequency range of operation, the overall efficiency including the entire measurement setup is in the range of 3%. The range of the transmission coefficients in Figure 7-13 vary between -22dB and -30dB. The Butler matrix adds losses of up to 7dB compared to the matrix at 5GHz due to higher dielectric and metallic losses of the LTCC material at 60GHz. The reflection coefficients are deteriorated to a level of -6dB, which could be traced back to the reflection coefficients of the V-connectors (at best -10dB).

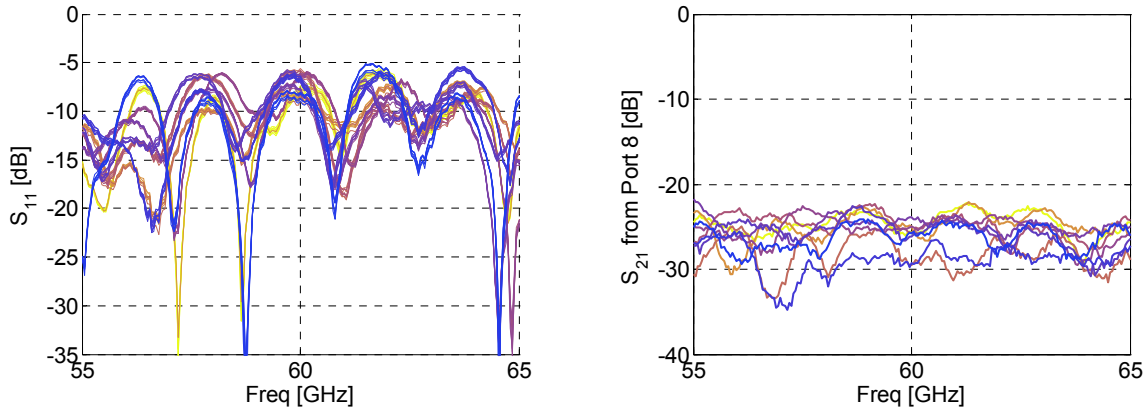

Figure 7-13 Reflection and transmission coefficients of the Butler matrix at 60GHz

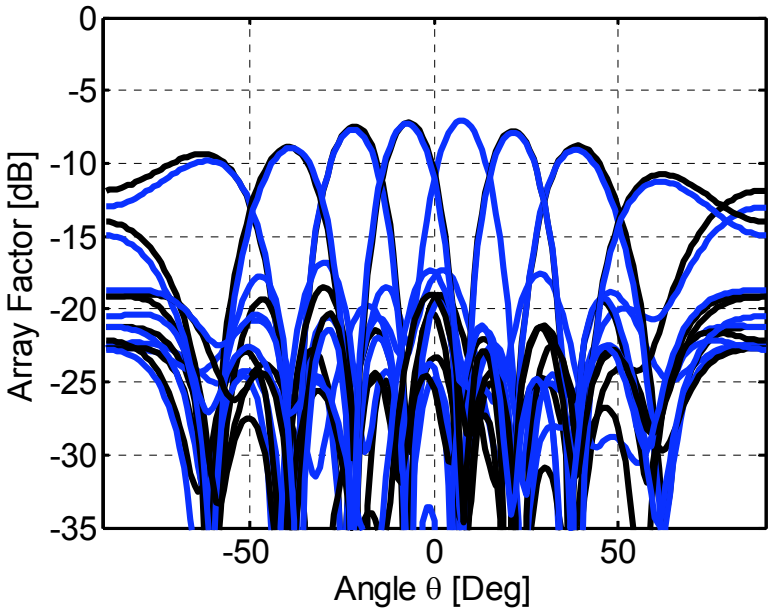

Figure 7-14 Array factor using the phase from the measurement (blue) and from the simulation (black) at 60GHz

The measured transmission coefficients were used to calculate the array factor plotted in Figure 7-14 using the blue color. The array factor in black is calculated from the simulated phase and the measured amplitude. Both plots in Figure 7-14 are at the center frequency of 60GHz. All eight beams from the measurements overlap with those from the simulation. The SLL increases only by 2dB at most. Therefore, we can conclude that the phase of the Butler matrix matches the one from the simulation. The overall gain level is between -7dB and -10dB which is around 15dB less than that in the Butler matrix at 5GHz. Even if the losses from the measurement setup were subtracted, the overall gain is still around 0dB. The array factor of the 8x8 Butler matrix is better than the one of the smaller antenna array reported in [54] using optical beamforming. The size and complexity reduction is considerable compared to the optical system.

For a better comparison between measured and simulated results, the normalized array factor is plotted in Figure 7-15. The measurement data is coded again with the blue color. The array factor in black was calculated using both the amplitude and the phase from the simulation. The SLL increases in the measured case to -8dB and this only for two of the beams on the left-hand side. The asymmetric increase can be explained only with a suboptimal transition from the LTCC to the measurement board. The

maximum beam deviation from the desired value is below one degree at the center frequency.

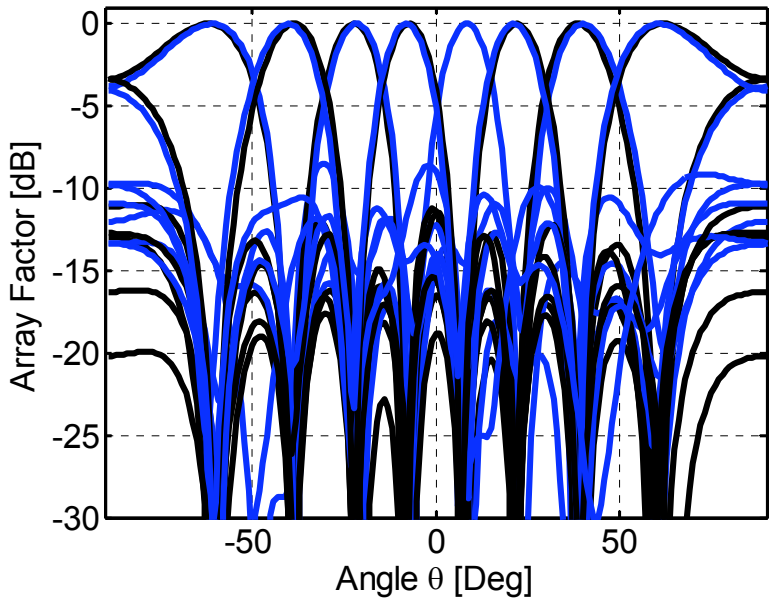

Figure 7-15 Normalized array factor of measurement (blue) and simulation using the amplitude from simulation at 60GHz

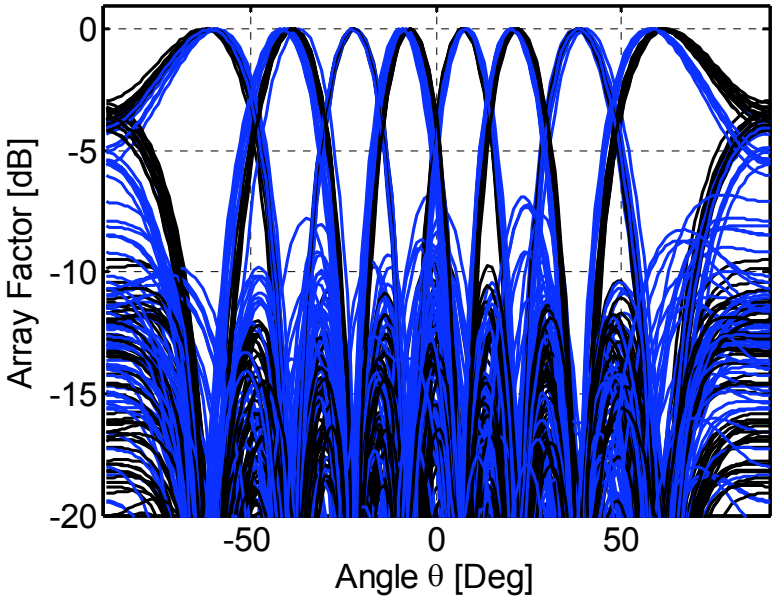

Figure 7-16 Array factor of the measurement and simulation at 10 frequency points in the range 55GHz-65GHz

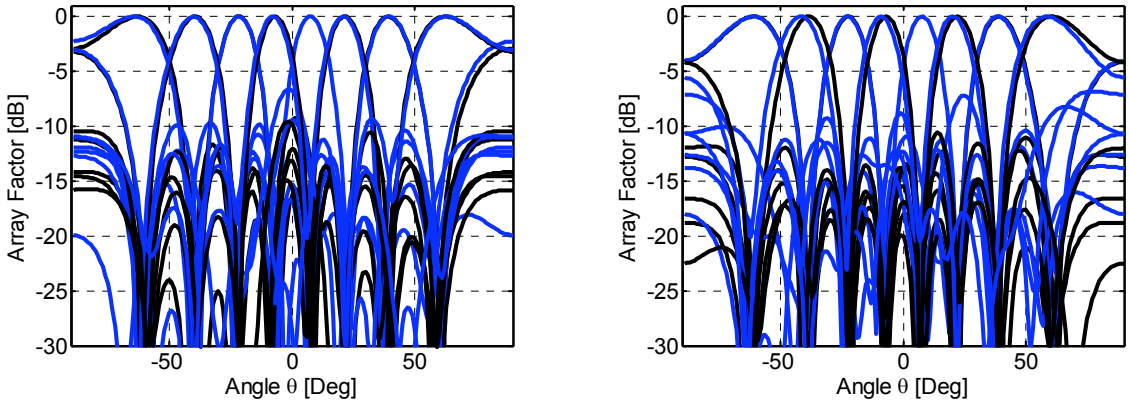

Figure 7-17 Array factor from the measurement and simulation using the amplitude from measurements at 55GHz and at 65GHz

Over the 10GHz frequency range the beam directions vary by at most 4 degree. This is seen in Figure 7-16, where each beam is plotted at 10 different frequency points in the 10GHz interval.

The measurement results at 55 GHz agree in with the simulation results better than at 65GHz, as can be seen in Figure 7-17. The transitions, the connectors and other phase errors of the matrix have a more pronounced effect at the higher frequencies.
The overall results show that the operation of this type of beamforming network can be extended to the V-band using the standard multilayer technology.

The 60GHz design exhibits a simple crossings type using sacrifice layers and still result in a compact design. All three LTCC Butler matrices presented offer new unique opportunities for specific application with multiple beams of new space division systems.

Chapter 8

Conclusions and Outlook

In the present work, the analysis of the split-dielectric Rotman lenses has been developed for the first time. The effort is motivated by the expected size reduction and increased efficiency of the lens. Introducing dielectric regions of different permittivity within the lens creates an additional refraction inside the lens and therefore reduces the overall size. Parametric study of the conventional and of the new lens structures were carried out, and the comparison showed the benefits and drawbacks of the new design. The non-uniform substrate proves to be the key factor in reducing the lens dimension.

The mathematical formulation for a two- and a three- dielectric lens was validated by the results of the full-wave simulation. Two lenses with dual substrate were realized and measurements to confirm the design methodology.

Outlook of the split-dielectric Rotman lens:

Increase internal reflections are the major drawback of the new dual- and triple-dielectric lenses design. Changing the material interface geometry can be a way to reduce the reflections. A wedge shape or a curved form may reduce the angle of incidence on the interface and therefore also the reflections. Another way to reduce the reflections is to add more regions of different dielectric constants and reduce the permittivity difference between the individual adjacent regions. This points toward a lens with a gradient of the dielectric constant within the lens instead of multiple regions of different dielectric constants. This can be done using the substrate modulation technique in LTCC. The air via holes can be applied with a density gradient along the lens resulting in a smooth dielectric permittivity tapering.

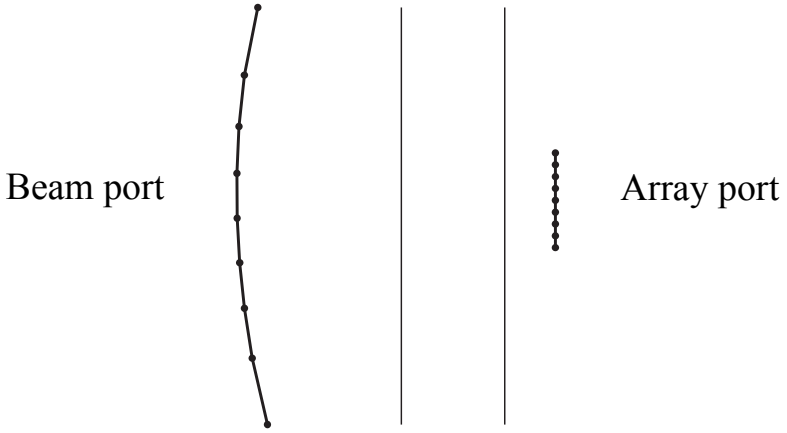

Figure 8-1 Layout of lens with a straight array contour

A future application can be also the lens with a straight array-port curve. A lens of this type has all transmission-line connections between array ports and antenna elements have the same electrical length. This is more convenient to connect such a lens to the antenna array by just using cables of the same length. A sketch and first results of a lens with a straight array contour is shown in Figure 8-1. The calculated dielectric constants are $\varepsilon_{r1} = 21.4$ at the beam port side, $\varepsilon_{r2} = 24.8$ in the middle and $\varepsilon_{r3} = 6$ at the array port side. The focal length is $f_1 = 4\lambda_0$ and the material interfaces are placed at $R_1 = 0.49 f_1$ and $R_2 = 0.16 f_1$.

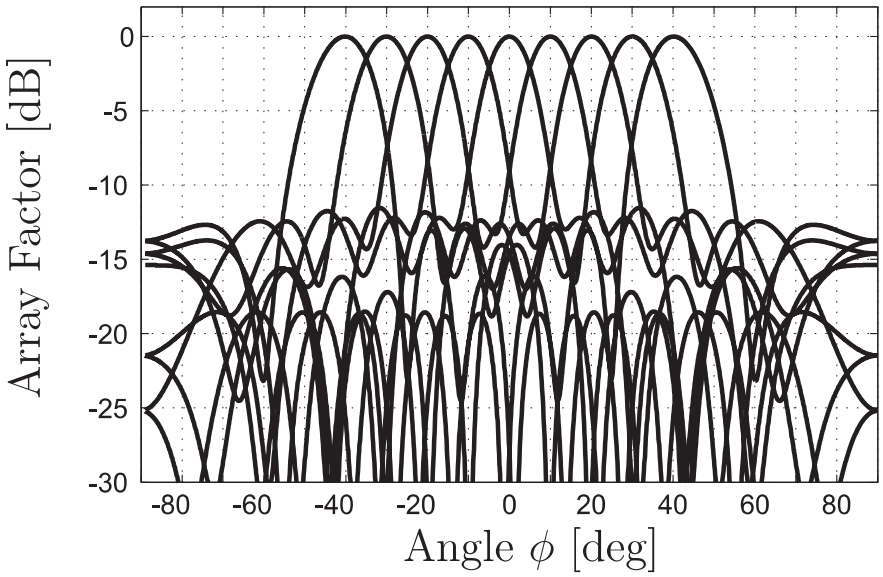

Figure 8-2 Array factor of lens with a straight array contour, calculated from path-length error.

For the design in Figure 8-1, the array factor is calculated from the path-length errors and plotted in Figure 8-2. One can see that the straight face lens shows the expected theoretical scanning properties. Practical realizations of such structure depends on the availability of the specific dielectric material.

The substantial real-estate requirements of the inner lens can be reduced by using the split-dielectric lens approach. The tapered input and output ports as well as the absorbing sidewalls require additional space. In order to maintain the gained size advantage, a folded design of Rotman lenses is introduced; this is the main contribution presented in this dissertation. The dissertation described the folding of the Rotman lens using a wideband stripline transition between the various LTCC layers. Current distribution and array factor of the folded Rotman lens were simulated and compared to the unfolded design. The folding was validated with a double-folded Rotman lens realized in LTCC.

In the last part of the dissertation, three different stripline configurations of 8x8 Butler matrices were constructed. The LTCC technology was used for the first time to implement the Butler matrix components: couplers, phase shifters, and the signal-line crossings.

The Butler matrices take full advantage of the packaging capability of LTCC. The novelty described lies in the extended folding and stacking of phase shifters and couplers from a 5-layer structure to a 40-layers one at 5 GHz. This again reduces the overall lateral dimensions of the lens and for the offers extendibility to higher order Butler matrices by using standard technologies. The size reduction is the effect of the new interconnecting strategy of the separate submodules that make up any higher-order Butler matrix. Therefore, this geometrical design helps realizing Butler matrices of higher-order at yet lower frequencies.

The last of the three designed Butler matrices, based on the same standard LTCC tape process, operates at frequencies centered at 60GHz. The size of the Butler matrix scales with the wavelength while maintaining the beamforming capabilities over wide bandwidths. On the other side, the work shows also the limits of these structures due to losses and technological limitation at high frequency. All three LTCC Butler matrices presented offer helpful new design concepts in the area of beam forming. The diffusion of the new Butler matrix and Rotman lens designs into a number of today's

communication front ends is highly depended on the future cost of the LTCC technology. The entry barrier for a number of mass products is a balance between manufacturing costs and the gain improvement brought by this compact beam forming networks.

This dissertation presents a set of new design tools for beamforming networks based on Rotman lenses and Butler matrices. The classical lens and matrix design applications -- radar and radiometry -- can therefore be extended with a variety of small-smart antenna front ends.

Bibliography

[1] A. J. Fenn, D. H. Temme, W. P. Delaney, and W. E. Courtney, "The development of phased-array radar technology," *Lincoln Laboratory Journal,* vol. 12, pp. 321-340, 2000.

[2] C. A. Fowler and C. A. F. Associates, "Old radar types never die; they just phased array or... 55 years of trying to avoid mechanical scan," *Aerospace and Electronic Systems Magazine, IEEE,* vol. 13, pp. 24A-24L, 1998.

[3] P. S. Hall and S. J. Vetterlein, "Review of radio frequency beamforming techniques for scanned and multiple beam antennas," *Microwaves, Antennas and Propagation, IEE Proceedings H,* vol. 137, pp. 293-303, 1990.

[4] W. Rotman and R. Turner, "Wide-angle microwave lens for line source applications," *Antennas and Propagation, IEEE Transactions,* vol. 11, pp. 623-632, 1963.

[5] J. Butler and R. Lowe, "Beam-forming matrix simplifies design of electronically scanned antennas," *Electronic Design,* vol. 9, pp. 170-173, 1961.

[6] J. J. Lee, "Lens Antennas," *Antenna Handbook,* 1993.

[7] B. Schoenlinner, X. Wu, J. P. Ebling, G. V. Eleftheriades, and G. M. Rebeiz, "Wide-scan spherical-lens antennas for automotive radars," *Microwave Theory and Techniques, IEEE Transactions on,* vol. 50, pp. 2166-2175, 2002.

[8] J. Ruze, "Wide-angle metal-plate optics," *Proc IRE,* vol. 38, 1950.

[9] G. Leonakis, "Correction to" Wide-Angle Microwave Lens for Line Source Applications," *Antennas and Propagation, IEEE Transactions on,* vol. 34, pp. 1067-1067, 1986.

[10] J. Shelton, "Focusing characteristics of symmetrically configured bootlace lenses," *Antennas and Propagation, IEEE Transactions on [legacy, pre-1988],* vol. 26, pp. 513-518, 1978.

[11] T. Katagi, S. Mano, and S. Sato, "An improved design method of Rotman lens antennas," *Antennas and Propagation, IEEE Transactions on,* vol. 32, pp. 524-527, 1984.

[12] D. R. Gagnon, "Procedure for correct refocusing of the Rotman lens according to Snell's law," *Antennas and Propagation, IEEE Transactions on,* vol. 37, pp. 390-392, 1989.

[13] R. C. Hansen, "Design trades for Rotman lenses," *Antennas and Propagation, IEEE Transactions on,* vol. 39, pp. 464-472, 1991.
[14] P. S. Simon, "ANALYSIS AND SYNTHESIS OF ROTMAN LENSES," *22 nd AIAA International Communications Satellite Systems Conference & Exhibit 2004,* p. 2004, 2004.
[15] D. Archer, "Lens-fed multiple beam arrays," *Microwave Journal,* vol. 27, pp. 171-172, 1984.
[16] L. Musa and M. S. Smith, "Microstrip port design and sidewall absorption for printed Rotman lenses," *Microwaves, Antennas and Propagation, IEE Proceedings H,* vol. 136, pp. 53-58, 1989.
[17] C. Metz, J. Grubert, J. Heyen, A. F. Jacob, S. Janot, E. Lissel, G. Oberschmidt, and L. C. Stange, "Fully integrated automotive radar sensor with versatile resolution," *Microwave Theory and Techniques, IEEE Transactions on,* vol. 49, pp. 2560-2566, 2001.
[18] M. E. Russell, A. Crain, A. Curran, R. A. Campbell, C. A. Drubin, W. F. Miccioli, R. Co, and M. A. Tewksbury, "Millimeter-wave radar sensor for automotive intelligent cruisecontrol (ICC)," *Microwave Theory and Techniques, IEEE Transactions on,* vol. 45, pp. 2444-2453, 1997.
[19] M. E. Russell, C. A. Drubin, A. S. Marinilli, W. G. Woodington, M. J. Del Checcolo, R. E. Syst, and M. A. Sudbury, "Integrated automotive sensors," *Microwave Theory and Techniques, IEEE Transactions on,* vol. 50, pp. 674-677, 2002.
[20] J. Blass, "Multidirectional antenna - A new approach to stacked beams," *IRE International Convention Record,* vol. 8, 1960.
[21] S. Mosca, F. Bilotti, A. Toscano, and L. Vegni, "A novel design method for Blass matrix beam-forming networks," *Antennas and Propagation, IEEE Transactions on,* vol. 50, pp. 225-232, 2002.
[22] F. Casini, R. V. Gatti, L. Marcaccioli, and R. Sorrentino, "A novel design method for Blass matrix beam-forming networks," *Radar Conference, 2007 EuRAD 2007 European,* pp. 232-235, 2007.
[23] J. P. Shelton, "Fast Fourier transforms and Butler matrices," *Proceedings of the IEEE,* vol. 56, pp. 350-350, 1968.
[24] J. W. Cooley and J. W. Tukey, "An Algorithm for the Machine Calculation of Complex Fourier Series," *Mathematics of Computation,* vol. 19, pp. 297-301, 1965.
[25] R. J. Mailloux, *Phased array antenna handbook*: Artech House Boston, 2005.

[26] L. Schulwitz and A. Mortazawi, "A New Low Loss Rotman Lens Design for Multibeam Phased Arrays," *Microwave Symposium Digest, 2006 IEEE MTT-S International,* pp. 445-448, 2006.
[27] Ansoft, "version 9.0," *Ansoft Corporation, Pittsburgh, USA*.
[28] T. J. Ellis and G. M. Rebeiz, "MM-wave tapered slot antennas on micromachined photonic bandgapdielectrics," *Microwave Symposium Digest, 1996, IEEE MTT-S International,* vol. 2, 1996.
[29] S. Yamamoto, J. Hirokawa, and M. Ando, "A beam switching slot array with a 4-way Butler matrix installed in a single layer post-wall waveguide," *Antennas and Propagation Society International Symposium, 2002 IEEE,* vol. 1, 2002.
[30] S. Yamamoto, J. Hirokawa, and M. Ando, "A Single-Layer Hollow-Waveguide 8-Way Butler Matrix," *IEICE Transactions on Electronics,* pp. 1080-1088, 2006.
[31] J. Remez and R. Carmon, "Compact designs of waveguide butler matrices," *IEEE Antennas and Wireless Propagation Letters,* vol. 5, pp. 27-31, 2006.
[32] S. F. Peik, B. Jolley, R. R. Mansour, C. Int, and O. Cambridge, "High temperature superconductive Butler matrix beamformer forsatellite applications," *Microwave Symposium Digest, 1999 IEEE MTT-S International,* vol. 4, 1999.
[33] A. Corona and M. J. Lancaster, "A high-temperature superconducting Butler matrix," *Applied Superconductivity, IEEE Transactions on,* vol. 13, pp. 3867-3872, 2003.
[34] R. A. De Lillo, "A high performance 8-input, 8-output Butler matrix beamforming network for ultra-broadband applications," *Antennas and Propagation Society International Symposium, 1993 AP-S Digest,* pp. 474-477.
[35] T. A. Denidni and T. E. Libar, "Experimental investigation of a microstrip planar feeding network for a switched-beam antenna array," *Antennas and Propagation Society International Symposium, 2002 IEEE,* vol. 1, 2002.
[36] R. Mongia, I. J. Bahl, and P. Bhartia, *RF and microwave coupled-line circuits*: Artech House Boston, 1999.
[37] D. M. Pozar, *Microwave engineering*: Wiley New York, 1998.
[38] J. Lange, "Interdigitated Stripline Quadrature Hybrid (Correspondence)," *Microwave Theory and Techniques, IEEE Transactions on,* vol. 17, pp. 1150-1151, 1969.
[39] S. Gruszczynski, K. Wincza, and K. Sachse, "Design of Compensated Coupled-Stripline 3-dB Directional Couplers, Phase

Shifters, and Magic-T's—Part I: Single-Section Coupled-Line Circuits," *Microwave Theory and Techniques, IEEE Transactions on,* vol. 54, pp. 3986-3994, 2006.

[40] M. Bona, L. Manholm, J. P. Starski, and B. Svensson, "Low-loss compact Butler matrix for a microstrip antenna," *Microwave Theory and Techniques, IEEE Transactions on,* vol. 50, pp. 2069-2075, 2002.

[41] G. E. Ponchak, D. Chun, J. G. Yook, L. P. B. Katehi, E. D. T. Branch, N. G. R. Center, and O. H. Cleveland, "The use of metal filled via holes for improving isolation in LTCC RF and wireless multichip packages," *Advanced Packaging, IEEE Transactions on [see also Components, Packaging and Manufacturing Technology, Part B: Advanced Packaging, IEEE Transactions on],* vol. 23, pp. 88-99, 2000.

[42] J. Heyen, A. Gordiyenko, P. Heide, and A. F. Jacob, "Vertical feedthroughs for millimeter-wave LTCC modules," *Microwave Conference, 2003 33rd European,* vol. 1, 2003.

[43] F. J. Schmuckle, A. Jentzsch, W. Heinrich, J. Butz, and M. Spinnler, "LTCC as MCM substrate: Design of strip-line structures and flip-chip interconnects," *IEEE MTT S INT MICROWAVE SYMP DIG,* vol. 1, pp. 1903-1906, 2001.

[44] J. Kim, H. Y. Lee, and T. Itoh, "Novel microstrip-to-stripline transitions for leakage suppressionin multilayer microwave circuits," *Electrical Performance of Electronic Packaging, 1998 IEEE 7th topical Meeting on,* pp. 252-255, 1998.

[45] J. P. Shelton, J. Wolfe, and R. C. Van Wagoner, "Tandem couplers and phase shifters for multi-octave bandwidth," *Microwaves,* vol. 4, pp. 14–19, 1965.

[46] T. Yuasa, Y. Tahara, and H. Oh-hashi, "90 Degree Tandem Hybrid with Tolerance to Displacement Error and Thickness Variation in Multi-layered Substrate," *Microwave Conference, 2006 36th European,* pp. 534-536, 2006.

[47] B. M. Schiffman, "A New Class of Broad-Band Microwave 90-Degree Phase Shifters," *Microwave Theory and Techniques, IEEE Transactions on,* vol. 6, pp. 232-237, 1958.

[48] D. Chai, M. Linh, M. Yim, and G. Yoon, "Asymmetric Teflon-based Schiffman phase shifter," *Electronics Letters,* vol. 39, pp. 529-530, 2003.

[49] S. J. Foti and T. Macnamara, "Design of wideband Butler matrices using Schiffman lines," *Multiple Beam Antennas and Beamformers, IEE Colloquium on,* p. 5, 1989.

[50] S. Y. Eom and H. K. Park, "New switched-network phase shifter with broadband characteristics," *Microwave and Optical Technology Letters,* vol. 38, pp. 255-257, 2003.

[51] A. M. Abbosh, "Ultra-Wideband Phase Shifters," *Microwave Theory and Techniques, IEEE Transactions on,* vol. 55, pp. 1935-1941, 2007.

[52] W. Ng, A. A. Walston, G. L. Tangonan, J. J. Lee, I. L. Newberg, and N. Bernstein, "The first demonstration of an optically steered microwave phased array antenna using true-time-delay," *Lightwave Technology, Journal of,* vol. 9, pp. 1124-1131, 1991.

[53] G. Grosskopf, R. Eggemann, H. Ehlers, A. Kortke, B. Kuhlow, G. Przyrembel, D. Rohde, and S. Zinal, "Maximum directivity beam-former at 60 GHz with optical feeder," *Antennas and Propagation, IEEE Transactions on,* vol. 51, pp. 3040-3046, 2003.

[54] G. Grosskopf, R. Eggemann, S. Zinal, B. Kuhlow, G. Przyrembel, D. Rohde, A. Kortke, and H. Ehlers, "Photonic 60-GHz maximum directivity beamformer for smart antennas in mobile broad-band communications," *Photonics Technology Letters, IEEE,* vol. 14, pp. 1169-1171, 2002.

[55] G. P. Riblet, "A Directional Coupler with Very Flat Coupling," *Microwave Theory and Techniques, IEEE Transactions on,* vol. 26, pp. 70-74, 1978.

George Tudosie

g.tudosie@gmail.com

Ausbildung

Doktorat am Institut für Feldtheorie und Höchstfrequenztechnik (IFH) der Eidgenössischen Technischen Hochschule Zürich (ETH)	12.2001-04.2008 Zürich/CH
Master of Advanced Studies in Management, Technology and Economics/BWI an der Eidgenössischen Technischen Hochschule Zürich (ETH)	10.2006-05.2008 Zürich/CH
Diplom-Ingenieur der Elektrotechnik und Informationstechnik mit Vertiefung Nachrichtentechnik an der Technischen Universität Darmstadt (TUD)	11.1998-07.2001 Darmstadt/D
Diplomarbeit am Forschungszentrum der DaimlerChrysler AG im Bereich Radartechnik für Fahrer-Assistenzsysteme (“Sehr Gut”)	04.2001-07.2001 Ulm/D
Vordiplom in Elektronik und Telekommunikation an der Technischen Universität Timisoara (”Sehr Gut”)	09.1996-06.1998 Timisoara/RO
Deutschsprachige Matura/Abitur am Nikolaus Lenau Lyzeum (”Sehr Gut“)	06.1996 Timisoara/RO

Projekte am Institut für Feldtheorie und Höchstfrequenztechnik (ETH Zürich)

- Realisierung eines rauscharmen **Radiometer-Front-Ends bei 35GHz** im Auftrag von **ArmaSuisse** unter Anwendung der LTCC Technologie - Teamarbeit über eine Zeitspanne von 3 Jahren
  - Verteilnetzwerke für phasengesteuerte Antennen - Butler Matrix (5GHz) realisiert auf LTCC mit **Micro Systems Engineering GmbH (MSE) - Deutschland**
  - Weitere Projekte in LTCC (Butler Matrizen und Rotman Linsen) realisiert mit der **Agency for Science, Technology and Research (A*STAR) - Singapore** (60GHz)
  - Entwurf und Realisierung von rauscharmen Antennenarrays (35GHz)

- **KTI Projekt mit Huber&Suhner** - ein vollautomatisches Abstimmverfahren wurde weiterentwickelt und abgeliefert. Mikrowellen- und Millimeterwellen Filter werden damit automatisch innerhalb des Produktionsprozesses abgestimmt.
  - Erweiterung der effizienten Optimierungsmethode auf Multiplexer (Planar und Hohlleiter) mittels elektromagnetischen Feldsimulationsprogrammen

- Simulation und technische Hilfestellung für Hohlleiterfilter - **Skyguide Genf**

- Technische Studie über einen akustischen Oberflächenwellen-Sensor (ISM-Band) für **Kistler Sensor**

- Betreuung von **Studien- und Diplomarbeiten** aus dem Bereich **Antennen, Filter, Multiplexer** und **passive Verteilnetzwerke**

- Assistenz der Vorlesung **„Antenna and Propagation“**, der Grundlagenvorlesung **„Felder und Komponenten I und II“** und eigenständige Leitung des Seminars **„Smart Antenna“** während der gesamten Zeit an der ETH